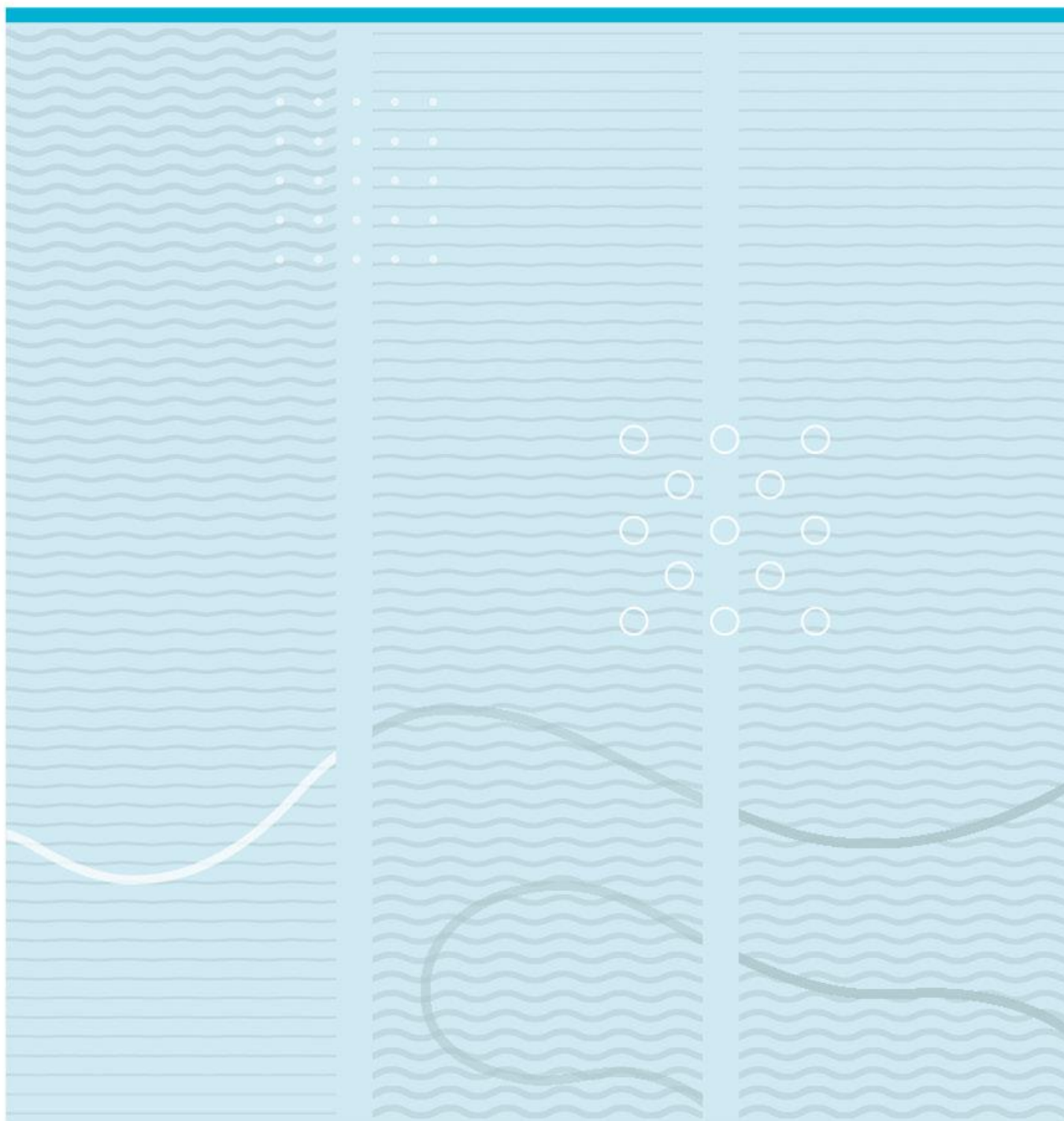


Anette Sollien Nicolaisen

Characterization of Layers with Metal-Coated Polymer Spheres for use in Ultrasound Transducers



University of South-Eastern Norway
Faculty of Technology, Natural Sciences and Maritime Sciences
Department of Microsystems.
Raveien 215
NO-3184 Borre, Norway

<http://www.usn.no>

© 2021 Anette Sollien Nicolaisen

Abstract

The properties of materials used in ultrasound transducers affect the properties of the finished transducer, making it important to characterize the acoustic properties of these materials.

The study in this thesis is focused on metal-coated polymer spheres, MPS, and characterization of composites with MPS and epoxy for use as bonding and acoustic matching layers in ultrasound transducers. Samples consisting of silicon, glass and a composite of spheres and epoxy were made to determine a method for making a monolayer of the spheres. Samples consisting of PZT, a monolayer of spheres and epoxy, and a load material were also made to see the effect of the sphere layer, with a 1D model being used to identify the acoustic properties of the layer, i.e. characteristic acoustic impedance and the speed of sound. The 1D analytical model was supplemented by 2D simulations for more accurate modeling. Thicker 0-3 composite samples were made and measured to determine the longitudinal speed of sound and the characteristic acoustic impedance in this material, and the values from the samples were compared with 2D simulations and values from the 1D models.

The fitting of the 1D Mason model to the impedance spectra from the trial samples gave a characteristic acoustic impedance between 2.7 and 3.1 MRayl and a speed of sound between 2700 m/s and 3200 m/s for the samples with 20 μm spheres. The later PZT samples gave a characteristic acoustic impedance between 2.9 and 3.1 MRayl and a speed of sound between 2400 m/s and 2500 m/s for samples with 40 μm spheres. The lower value of the speed of sound for the 40 μm spheres was also indicated by the thicker 0-3 composite samples, where the 20 μm sphere samples had a speed of sound of 2586 ± 50 m/s, while the 40 μm sphere samples had a speed of sound of 2449 ± 31 m/s. FEM simulations for the speed of sound on the other hand indicated that the speed of sound of the 40 μm sphere layer should be higher than for the 20 μm sphere layer. The speed of sound samples with 40 μm spheres did also show more clearly air-bubbles for all samples, which has most likely affected the results, making the measured speed of sound of the 40 μm sphere layers lower than the real value.

The FEM simulations of the thermal conductivity showed that 2D simulations can be used as an indicator for the thermal conductivity of a layer. The calculated thermal conductivity decreased slightly with increased sphere diameter, and it also showed a decrease in value with a thin layer of polymer between the sphere and the boundary. For the layers with the same thickness as the boundary, the thermal conductivity was 0.320 ± 0.002 W/(m*K) for the 40 μm sphere layer and 0.325 ± 0.001 W/(m*K) for the 20 μm layer.

Acknowledgements

I would like to express my greatest appreciation to my supervisor Prof. Lars Hoff. His guidance and encouragement have helped a lot throughout the work with the thesis, and his comments and discussions has been extremely valuable for the development of and work with this thesis. I would like to thank Prof. Lars Hoff for giving me such an interesting master project, and for all his help throughout the work.

I would also like to express my gratitude to my co-supervisor, Phd-candidate Per Kristian Bolstad for all his extremely valuable help in the lab and with the models. Without his help, the thesis would not have been possible. I would also like to thank him for the possibility to use his COMSOL model for simulations in this thesis.

I would like to thank Martijn Frijlink for his suggestions and comments. It has been of great help in the work.

I would like to thank Helge Kristiansen and Erik Kalland at Conpart for their help with the fabrication of the trial PZT samples and their help with developing methods used for fabrication of later samples. I also want to thank Helge Kristiansen for giving me the project and for providing access to the materials, and for giving me the possibility to visit Conpart.

Finally, I would like to thank my family for all their support and patience throughout the work with this thesis. Thank you for teaching me the value of hard work, and that anything is possible.

Horten 01/06/21

Anette Sollien Nicolaisen

Table of contents

1	Introduction.....	1
1.1	Background	1
1.2	Objective/Motivation	2
1.3	Thesis structure	2
2	Theory.....	4
2.1	Ultrasound.....	4
2.2	Material characteristics	8
2.3	Models.....	10
3	Materials and method.....	14
3.1	Trial samples	14
3.2	Mixing and loading values	16
3.3	0-3 Composites.....	18
3.4	Monolayer method	22
3.5	Monolayer PZT	23
3.6	FEM modeling	26
4	Results.....	34
4.1	Glass values.....	34
4.2	Trial samples	35
4.3	0-3 composite samples	44
4.4	Modeling	52
4.5	Silicon samples.....	57
4.6	PZT samples.....	60
5	Discussion.....	73
5.1	Trial samples	73
5.2	0-3 composite samples	74
5.3	Thermal conductivity	76
5.4	Monolayer samples	78
5.5	Comparison fitting and calculation	80
6	Conclusion	83
6.1	Future work	83
	References	85
	Appendix	87
	A. Pz27 Ferroperm data.....	87
	B. Code for creating 2D sphere layer geometry (COMSOL)	88
	C. Code for creating 3D sphere layer geometry (COMSOL)	92
	D. Transducer process	99
	E. Speed of Sound samples	105

List of figures

Figure 2.1: The longitudinal and shear wave movements in a material.	5
Figure 2.2: Normal incident wave on a boundary with the reflected and transmitted wave direction.	5
Figure 2.3: The Mason equivalent circuit model for an electro-mechanical transducer.....	11
Figure 3.1: Trial samples 3 and 4 (left) and trial sample 6 and 7 (right).....	15
Figure 3.2: Trial sample 8 (left) and trial samples 10 (40 μ m), 11 (20 μ m), 17 and 18 (right).....	15
Figure 3.3: Trial samples 1, 5, 13, 14, 15 and 16.....	15
Figure 3.4: Speed of sound setup; measurement setup (left) and oscilloscope, signal source and computer setup (right).	17
Figure 3.5: Working principle of the speed of sound measurement.	17
Figure 3.6: 20 μ m spheres and Epo-tek 301-2 without Byk (left) and with Byk (right)	19
Figure 3.7: Mixing trial samples after curing (from left): 40 μ m without Byk, 20 μ m without Byk, 40 μ m with Byk and 20 μ m with Byk	20
Figure 3.8: The finished speed of sound samples.....	22
Figure 3.9: Finished silicon monolayer samples S4 to S9.....	23
Figure 3.10: Cross section of the Pz27 pieces after creating wrap around.	24
Figure 3.11: Pz27 sample from above after creating wrap around.....	24
Figure 3.12: Finished samples with PZT, glue-sphere layer and glass load.....	25
Figure 3.13: Finished samples with PZT, glue-sphere layer and tungsten carbide (WC) load	25
Figure 3.14: Geometry type nr. 1.	27
Figure 3.15: Geometry type nr. 2.	27
Figure 3.16: Geometry type nr. 3.	28
Figure 3.17: 3D geometry for the thermal conductivity simulation.	28
Figure 3.18: COMSOL geometry used in the simulation of the monolayer PZT samples.....	30
Figure 3.19: Zoomed in image of the sphere layer (yellow) in the impedance COMSOL geometry.....	31
Figure 3.20: The structure used for speed of sound simulations.	33
Figure 3.21: Zoomed in image of the sphere layer (in blue, left) and the thin water layer (right)	33
Figure 4.1: The power spectrum in decibel for sample L1.....	34
Figure 4.2: Air bubble in glue layer of trial sample 7. The scale bar has a length of 1 mm.....	35
Figure 4.3: Uneven edge of the glue layer of trial sample 18. The scale bar has a length of 1 mm.	35
Figure 4.4: Incomplete compression of sphere layer between a PZT (bottom) and glass load (top), sample 6.....	36
Figure 4.5: A good compression of glue-sphere layer only slightly bigger than the sphere diameter, sample 18	36
Figure 4.6: The most common cross section of the samples, with the compression being partially incomplete and spheres are being stacked on top of each other, sample 13.....	37
Figure 4.7: Impedance curve (top) and phase curve (bottom) for initial sample 3 consisting of a 5MHz PZT and glass load.....	39
Figure 4.8: Impedance curve (top) and phase curve (bottom) for initial sample 4 consisting of a 5MHz PZT and glass load.....	39

Figure 4.9: Impedance curve (top) and phase curve (bottom) for initial sample 6 consisting of a 5MHz PZT and glass load.....	40
Figure 4.10: Impedance curve (top) and phase curve (bottom) for initial sample 7 consisting of a 5MHz PZT and glass load.....	40
Figure 4.11: Impedance curve (top) and phase curve (bottom) for initial sample 8 consisting of a 5MHz PZT and glass load.....	41
Figure 4.12: Impedance curve (top) and phase curve (bottom) for initial sample 13 consisting of an 8MHz PZT and WC load.....	41
Figure 4.13: Impedance curve (top) and phase curve (bottom) for initial sample 15 consisting of an 8MHz PZT and WC load.....	42
Figure 4.14: Impedance curve (top) and phase curve (bottom) for initial sample 16 consisting of an 8MHz PZT and WC load.....	42
Figure 4.15: Impedance curve (top) and phase curve (bottom) for initial sample 17 consisting of an 8MHz PZT and glass load.....	43
Figure 4.16: Impedance curve (top) and phase curve (bottom) for initial sample 18 consisting of an 8MHz PZT and glass load.....	43
Figure 4.17: Graphs showing the effect of different impedance values for the sphere layer.	44
Figure 4.18: Comparison of the ideal density of the material (blue) and density calculated from the fabricated samples (red).....	44
Figure 4.19: The cross section of the test sample with 40 μm spheres without Byk, SoS2.	45
Figure 4.20: The cross section of the test sample 20 μm spheres with Byk, SoS3.	46
Figure 4.21: The 20 μm sphere samples with Byk, SoS3, (left) and without Byk, SoS1, (right), seen from the underside, 200x magnification.....	46
Figure 4.22: Monolayer of spheres on top of the 40 μm speed of sound sample without Byk, SoS4, 100x magnification.....	47
Figure 4.23: Bar chart comparing the average speed of sound of the different SoS samples.	49
Figure 4.24: Bar chart comparing the average acoustic impedance of the different SoS samples.	49
Figure 4.25: Cross section of proper speed of sound samples, with 20 μm speed of sound sample on top and 40 μm speed of sound sample on bottom.	50
Figure 4.26: Cross section of SoS5, 200x magnification, indicating no air bubbles are present.....	50
Figure 4.27: Cross section of SoS10, 200x magnification.....	50
Figure 4.28: Graph with the speed of sound found from simulations.	51
Figure 4.29: The reflection coefficient spectrum for the thick 20 μm , 10% volume sphere simulations. ..	52
Figure 4.30: Temperature distribution in structure of same radius spheres.....	52
Figure 4.31: Temperature distribution in geometry with random sphere radius and random distribution..	52
Figure 4.32: Temperature distribution in geometry with random sphere size, set y-coordinate of the circle center and random x-coordinate.....	53
Figure 4.33: Temperature distribution for the 40 μm same size geometry where the sphere layer is compared to PMMA.....	53
Figure 4.34: Temperature distribution for the 40 μm same place, random size geometry where the sphere layer is compared to PMMA.....	53

Figure 4.35: Graph showing the variations of the thermal conductivities for the 20 μm 2D simulations. .	55
Figure 4.36: Graph showing the variations of the thermal conductivities for the 40 μm 2D simulations. ..	56
Figure 4.37: Graph showing the variations of the thermal conductivities for the 3D simulations.	56
Figure 4.38: Thickness distribution of the silicon samples made with glass from the small microscope coverslips calculated from mechanical measurements. All thicknesses are given in μm	58
Figure 4.39: Thickness distribution of the silicon samples made with glass from the large coverslips calculated from mechanical measurements. All thicknesses are given in μm	58
Figure 4.40: Image through the glass of the underside of silicon sample S4, 100x magnification	59
Figure 4.41: Image through the glass of the underside of silicon sample S5, 100x magnification	59
Figure 4.42: Image through the glass of the underside of silicon sample S6, 100x magnification	59
Figure 4.43: Image through the glass of the underside of silicon sample S8, 100x magnification.	60
Figure 4.44: Thickness of the sphere layer for the glass load samples calculated from mechanical measurements.....	60
Figure 4.45: Thickness of the sphere layer for the tungsten carbide (WC) load samples calculated from mechanical measurements.....	61
Figure 4.46: The underside of PZT sample 2 taken through the glass, 63x magnification.	62
Figure 4.47: Cross section of PZT sample 5, 200x magnification.	63
Figure 4.48: The crack created in PZT sample 3 during fabrication, 32x magnification. Placement on the sample is shown to the right.....	63
Figure 4.49: Air bubbles in PZT sample 1, 32x magnification. Placement on the sample is shown to the right.....	64
Figure 4.50: Air pocket in PZT sample 4, 32x magnification. Placement on the sample is shown to the right.....	64
Figure 4.51: Air pocket in PZT sample 4, 32x magnification. Placement on the sample is shown to the right.....	65
Figure 4.52: Impedance curves simulated in COMSOL, comparing the effect of the sphere layer between the PZT and the load material, and the effect of air between the PZT and the load material.....	65
Figure 4.53: Impedance curve (top) and phase curve (bottom) from measurement, Xtrans and COMSOL for PZT sample 1 before air-bubbles were tried cut away.....	66
Figure 4.54: Impedance curve (top) and phase curve (bottom) from measurement, Xtrans and COMSOL for PZT sample 1 after the air-bubbles were tried cut away.....	66
Figure 4.55: Impedance curve (top) and phase curve (bottom) from measurement, Xtrans and COMSOL for PZT sample 2.....	67
Figure 4.56: Impedance curve (top) and phase curve (bottom) from measurement, Xtrans and COMSOL for PZT sample 4 before the air pocket was cut away. The cut version had too much noise to make a good fit.....	67
Figure 4.57: Impedance curve (top) and phase curve (bottom) from measurement, Xtrans and COMSOL for PZT sample 5.....	68
Figure 4.58: Impedance curve (top) and phase curve (bottom) from measurement, Xtrans and COMSOL for PZT sample 6 before the air pocket was cut away.....	68

Figure 4.59: Impedance curve (top) and phase curve (bottom) from measurement, Xtrans and COMSOL for PZT sample 6 after the air pocket was cut away.	69
Figure 4.60: Impedance curve (top) and phase curve (bottom) from measurement, Xtrans and COMSOL for PZT sample 7.	69
Figure 4.61: Impedance curve (top) and phase curve (bottom) from measurement, Xtrans and COMSOL for PZT sample 9.	70
Figure 4.62: Impedance curve (top) and phase curve (bottom) from measurement, Xtrans and COMSOL for PZT sample 10.	70
Figure 4.63: Impedance curve (top) and phase curve (bottom) from measurement, Xtrans and COMSOL for PZT sample 11.	71
Figure 4.64: Impedance curve (top) and phase curve (bottom) from measurement, Xtrans and COMSOL for PZT sample 14.	71
Figure 4.65: Impedance curve (top) and phase curve (bottom) from measurement, Xtrans and COMSOL for PZT sample 15.	72

List of tables

Table 1.1: Naming of the fabricated samples, with a description and background for the names	3
Table 2.1: Governing equations for the Mason model alone and common with KLM	11
Table 3.1: Weights and type of mixer used for the first sphere mixes	14
Table 3.2: Samples with the load type, MPS diameter and resonance frequency of piezo, as well as whether the sample was discarded or not.	16
Table 3.3: Size parameters and weight of the glass samples in the speed of sound measurement.	18
Table 3.4: Values for calculating particle density	18
Table 3.5: Calculated masses for the mixes	19
Table 3.6: Weight of MPS and glue added to the speed of sound 0-3 composites.....	21
Table 3.7: Average thickness and the weight of the speed of sound samples	21
Table 3.8: Weights added to create mixes for the silicon samples	22
Table 3.9: Summary of the loading method and curing time of the Si samples.	23
Table 3.10: The weight of Epo-tek 301-2 and spheres used for the mixes for the PZT samples.	24
Table 3.11: Overview of the geometry parameters used for thermal conductivity simulations	29
Table 3.12: The expressions used for the global variable probes.	32
Table 4.1: Measured properties of the glass load used for the trial samples.	34
Table 4.2: Measured thicknesses of the initial samples and the values used in xtrans	38
Table 4.3: Comparison of ideal/calculated density and measured density of the spheres and the samples.	45
Table 4.4: Measured speed of sound and characteristic acoustic impedance for the 0-3 composite speed of sound samples.	48
Table 4.5: The speed of sounds calculated from simulations of the reflection coefficient.....	51
Table 4.6: Comparison of methods for finding the thermal conductivity of a monolayer for 20 μm	54
Table 4.7: Comparison of methods for finding the thermal conductivity of a monolayer for 40 μm	55
Table 4.8: Overview of the average thermal conductivity and standard deviation for the different geometries.	57
Table 4.9: Thickness of the sphere layer of the silicon samples measured with the optical microscope. All thicknesses are given in μm	57
Table 4.10: Thicknesses of the sphere layers of the PZT samples, measured with the optical microscope. All thicknesses are given in μm	61
Table 4.11: The values used in Xtrans to fit the 1D simulated impedance graph to the measured impedance	62

Abbreviations

FEM	finite element method
ICA	isotropic conductive adhesive
MPS	metal-coated polymer spheres
PMMA	polymethyl methacrylate
PZT	lead zirconate titanate
Si	silicon
WC	tungsten carbide

1 Introduction

1.1 Background

Ultrasound is sound waves with frequencies above what the human ear can hear, that is frequencies above 20kHz. These frequencies have been used by animals in millions of years through echolocation, while the human use of these frequencies began during World War I with sonars to detect submarines. Now the technology has evolved and ultrasound is used within several disciplines, ranging from imaging the inside of the body to mapping the seafloor and to do non-destructive testing on electrical structures. Some of the advantages with using ultrasound is that it is non-destructive, it can be used over long distances, while at the same time it is safe compared to other methods like X-rays, since it does not utilize ionizing radiation. [1]

The ultrasound system consists of several parts, where one of the most important is the ultrasound transducer. This is the part of the system which sends out and receives the ultrasound signal through conversion of energy from electrical to mechanical and vice versa. This can have many designs in order to optimize the transmission of energy, with one of the more common designs consisting of a backing layer, a piezoelectric material, and one or more matching layers. How well the transducer transmit waves depends on the materials used to build it, as the transmission and reflection of waves depends on the acoustic impedance of the materials. A large difference in this parameter between two materials will cause more of the wave to be reflected at the boundary between the materials, as can be seen from the expression of the reflection coefficient R [2]

$$R = \frac{Z_2 - Z_1}{Z_2 + Z_1} \quad (1.1)$$

Here, R is the ratio between reflected and incoming pressure amplitudes and $Z_k = \rho_k c_k$ is the characteristic acoustic impedance of the two mediums, $k = 1,2$. ρ_k is the density and c_k is the speed of sound in medium k . The acoustic impedance of the most commonly used piezoelectric materials, e.g. PZT, are much higher than that of the common loads, causing most of the wave to be reflected if they were to make up the boundary. The matching layers are used to compensate for this difference, and works as a step between the piezoelectric element and the load. These layers are often made separately and then glued on, which can be a time-consuming process, and they are often made of polymer materials, which does not conduct heat very well. [3]

An alternative to the common matching layer is to use metal-coated polymer spheres, MPS, in the matching layer material. These spheres could improve the heat conduction in a matching layer and also provide electrical conduction through the layer. They can also be used to create monolayers with a well-defined thickness, and thereby be used either as a matching layer for high frequencies or as a glue layer. However, before the spheres can be used in ultrasound transducers, the material has to be characterized. Studies on composites made with these spheres has mostly been done to investigate the possibility of using them as a replacement for silver particles in isotropic conductive adhesives, ICA [4]. These studies have investigated and characterized many of the material properties, but the characterization of the acoustic properties is limited. One investigation into the acoustic properties was the master thesis by Blomvik [5], who did not

do experimental studies, but did a FEM study on the acoustic properties of the MPS and epoxy. However, this was also done for a composite that could replace the ICA. The high volume fraction of spheres needed to make these ICAs will make it difficult to use the composite to make a monolayer, so the investigations in this master thesis will focus on a lower volume fraction than what is used in the ICA studies.

1.2 Objective/Motivation

The aim of the project is to identify the acoustic properties of layers of metal-coated polymer spheres, MPS, in epoxy, in order to identify possible use as a matching layer. The focus will be on the speed of sound of the layers and the acoustic impedance, as these are the most important properties for the matching layer. The thermal conductivity will also be looked at to identify the effect of the MPS. It is highly wanted to identify the properties both for a layer of thicker size, and of monolayer thickness. Making a monolayer can be difficult, however, the advantage of it is that the layer thickness can be accurately defined.

The general task is to characterize the acoustic properties of epoxy layers with MPS and assess how they can be used as matching or glue layers in ultrasound transducers. This is done through the following steps:

- Modeling
 - o Model the transducer stacks as a Mason equivalent model, using the Xtrans software for MATLAB
 - o Simulate the fabricated samples as a stack of PZT, MPS layer and load with a FEM model using COMSOL
 - o Use COMSOL to simulate the speed of sound and the thermal conductivity of the material using the sphere structure
- Fabrication
 - o Make samples to determine a fabrication method for monolayers
 - o Make thicker 0-3 composite samples for speed of sound measurements
 - o Make transducers with monolayers for impedance measurement
- Characterization
 - o Measure speed of sound
 - o Measure acoustic impedance
- Compare measurements, calculations and estimations

1.3 Thesis structure

The thesis is structured in the following way. An introduction to ultrasound transducers and the common build, as well as motivations and objectives is given in Chapter 1. Chapter 2 presents theory on ultrasound, the ultrasound transducer, as well as mathematical formulas and other theory related to the thesis. The fabrication and simulation methods are described in Chapter 3. Chapter 4 gives the results from the fabricated samples and simulations, which are discussed in detail in Chapter 5. Chapter 6 concludes the work and makes suggestions for future work. The appendix contains a more detailed walkthrough of the fabrication of the samples, together with material parameters and code used to create the sphere layers in the FEM simulations.

Table 1.1 is a list of the naming of the different samples and the background for that naming.

Table 1.1: Naming of the fabricated samples, with a description and background for the names

Name	Sample type	Description
L	Silicon monolayer and glass speed of sound samples	L references the large glass coverslips with initial size 5.2 cm x 7.6 cm. A number is added to the L to indicate the different samples.
S	Silicon monolayer and glass speed of sound samples	S references the small glass coverslips with initial size 2.6 cm x 7.6 cm. A number is added to the S to indicate the different samples.
SoS	0-3 composite speed of sound samples	SoS references that the samples are used for speed of sound measurements. A number is added to the SoS to indicate the different samples.
Sample	PZT (Pz27) samples	Referenced by name Sample and differentiated by numbers
Trial	PZT trial samples	Referenced by the name Trial and differentiated by numbers

2 Theory

2.1 Ultrasound

2.1.1 Ultrasound basics

Audible sound is in the frequency range from 20Hz to 20kHz, while ultrasound is defined as the frequencies above the audible range, that is above 20kHz. As with ordinary sound, ultrasound needs a medium to propagate, either a solid, a liquid or a gas.

The speed of sound, the speed at which the wavefront of the ultrasound wave moves, differs between materials and with temperature, but it remains constant for a given medium at a constant temperature. Another property that depends on the material is the wavelength, which is the distance covered by one cycle of the wave. The relation between the two can be written as

$$c = f\lambda \quad (2.1)$$

where c is the speed of sound, f is the frequency of the wave, which is constant, and λ is the wavelength in the medium. The wavelength of an ultrasound signal in a material is difficult to measure directly, however, the speed of sound can be measured quite easily using through-transmission. Here a sample of the material is placed in a coupling medium, often water, between two transducers which are aligned so that the signal can go in a straight line from one transducer to the other. One of the transducers will work as a transmitter, sending out a signal through the sample, and the other works as a receiver. The signal will be both reflected and transmitted, and the time difference between two received signals can be used to calculate the speed of sound. [6]

Waves in a medium can move through it in several ways. The different modes can be divided into groups depending on how the particles in the medium vibrate relative to the motion of the wave, with the two main groups being compressional waves and shear waves, the movement of which are shown in Figure 2.1.

Compressional waves, also known as longitudinal waves, has particle movement parallel to the wave movement. As the name implies, the movement of the particles creates compression and rarefaction of the material. The movement of the particles themselves is small, so that the wave that is transmitted is a pressure wave. [7] This wavetype can transmit through any material, be it gas, liquid or solid state, and is the most commonly used wave in ultrasound.

Shear waves, also known as transverse waves, has particle movement perpendicular to the wave movement. [7] These types of waves can only be supported by solids, unlike the longitudinal type, which could pass in any material. The shear wave speed of sound is for many common solids around half that of the longitudinal speed of sound.

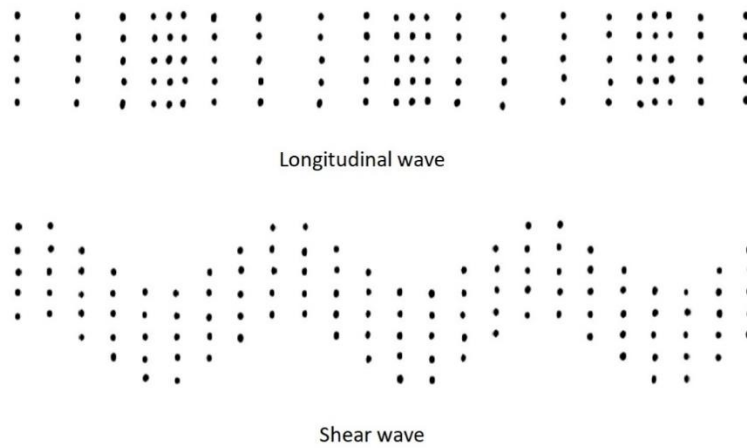


Figure 2.1: The longitudinal and shear wave movements in a material.

2.1.2 Acoustic impedance, reflection and transmission

Impedance is often used in electrical terms to describe an opposition to the flow of electrical current. Acoustic impedance can be seen as a measure of the opposition to the motion, i.e. velocity, that results from an ultrasound pressure. This is a property of the material and the wavefield, and is defined as the ratio between the pressure in the ultrasound signal and the velocity. The characteristic acoustic impedance is the acoustic impedance for a plane wave and is characteristic for a material and the type of wave propagating through the material. [8] A definition of this is

$$Z = \rho c \tag{2.2}$$

where ρ is the density of the material, and c is the speed of sound.

The characteristic acoustic impedance plays a big role when it comes to transmission and reflection of a wave. The wave will propagate through the material until it hits a boundary with another material, where some of the wave will be transmitted and some will be reflected as shown in Figure 2.2.

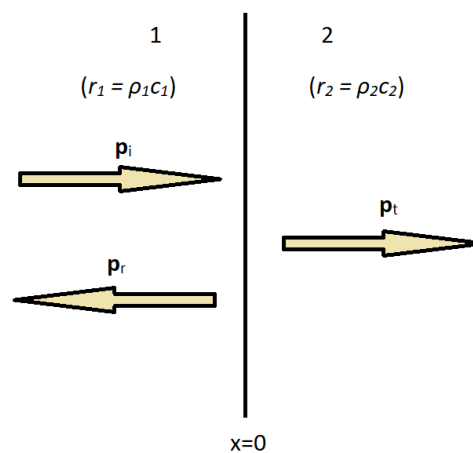


Figure 2.2: Normal incident wave on a boundary with the reflected and transmitted wave direction. The arrows represent the wave directions, where p_i is the incident wave, p_r is the reflected wave, and p_t is the transmitted wave. The vertical black line is the boundary between the materials.

The reflection and transmission are results of differences in acoustic impedance. As long as the impedance is the same, as with a single material, the wave will propagate. However, when it hits a boundary where the acoustic impedance changes, some will be reflected and some will be transmitted. How much of the signal that is reflected depends on the difference in acoustic impedance, where a large difference will cause a lot of the energy in the signal to be reflected. The reflection and transmission coefficients can be calculated from the acoustic impedance of the two media: [8]

$$R = \frac{Z_2 - Z_1}{Z_2 + Z_1} \quad (1.1)$$

$$T = \frac{2Z_2}{Z_2 + Z_1} \quad (2.3)$$

Here R is the reflection coefficient, the ratio between the reflected and incoming wave. T is the transmission coefficient, and is the ratio of the transmitted and incoming wave. Z_1 and Z_2 are the impedances of material 1 and material 2 respectively.

2.1.3 Ultrasound transducer

A common ultrasound transducer consists of a stack of several layers; a backing layer, a piezoelectric element and one or more matching layers. In addition to these layers, the transducer often consists of thin glue layers that bond the other layers together, as well as it may contain an acoustic lens or protecting encapsulations.

The piezoelectric element is the part of the transducer which creates and registers the signal, through the piezoelectric effect. This effect causes the creation of an electrical field due to an applied strain or the creation of strain when an electric field is applied. Under the application of strain, electrical charges will appear on the surface, creating the electric field mentioned above. This process, with the creation of an electrical field from an applied strain is called the direct piezoelectric effect. The opposite way, that is the creation of strain from an applied electrical field, is called the inverse piezoelectric effect. [9] The resonance frequency of a piezoelectric element is determined by the thickness of the element. The relation stems from how efficient the element works for different frequencies. An element with a light backing material, like air, has its most efficient operation when the thickness of the element is half the signal wavelength, which gives the resonance frequency

$$f_0 = \frac{c}{\lambda} = \frac{c}{2t} \quad (2.4)$$

Where c is the speed of sound, f_0 is the resonance frequency, λ is the wavelength and t is the thickness of the piezoelectric element. [7] This formula can be derived from the relation between frequency, wavelength and speed of sound in equation (2.1).

The piezoelectric effect does occur naturally, however, the piezoelectric properties of these materials are usually not that strong. Ferroelectric materials with better electro-mechanical coupling have therefore been made. [9] The different domains in the ferroelectric material have dipoles pointing in all directions when strained, meaning the total crystal will not have any dipole. The different dipoles can be made to point in the same direction by heating the ferroelectric material to above the Curie temperature and then slowly cool

it in the presence of a dc electric field. If the material is heated above the Curie temperature again, it will lose its piezoelectric properties, and a new poling process has to be done. [10]

The piezoelectric element used in the ultrasound transducer often has an acoustic impedance around 30 MRayl, while the load can have a much lower value, like 1.5 MRayl for water or biological tissue. [2] This difference is quite large, making the transmission of a signal from the piezoelectric element to the load difficult. The matching layer is added to the transducer to improve the transmission, working as a stepping stone for the acoustic impedance between the piezoelectric element and the load. It therefore needs to have a value between that of the piezoelectric element and the load.

Optimization of the matching layer acoustic impedance can maximize the transmission of signal from the transducer to the load. For a monochromatic plane wave, total transmission can be obtained using a matching layer with thickness $\lambda_M/4$, where λ_M is the wavelength of the signal in the matching layer. The acoustic impedance of the matching layer should then be given as

$$Z_M = \sqrt{Z_p Z_L} \quad (2.5)$$

where Z_p is the acoustic impedance of the piezoelectric element and Z_L is the acoustic impedance of the load. However, this matching is based on a single frequency, and will have good transmission for that frequency and a small band of frequencies around the one it is made for. This will however not be useful for signals with a wider band of frequencies, and therefore a wide band of wavelengths, as longer and shorter wavelengths will experience reflection. [8]

For wideband transducers, optimized impedance for the matching layers can be found using the calculations in the paper by Desilet et al. [11] In this paper, the expressions for the optimized matching layer values are derived based on the KLM equivalent circuit model. The acoustic impedance for a single matching layer is:

$$Z_m = Z_p^{\frac{1}{3}} Z_l^{\frac{2}{3}} \quad (2.6)$$

While for transducers with two matching layers the acoustic impedance of the two layers should be:

$$Z_{m1} = Z_p^{\frac{4}{7}} Z_l^{\frac{3}{7}} \quad (2.7)$$

$$Z_{m2} = Z_p^{\frac{1}{7}} Z_l^{\frac{6}{7}} \quad (2.8)$$

For both cases, Z_m is the matching layer impedance, where subscript 1 and 2 means matching layer 1 and matching layer 2 respectively, while Z_p and Z_l are the acoustic impedance of the piezo and the load respectively.

The backing layer is the layer behind the piezoelectric element, which receives the waves sent back from the front of the piezoelectric material. Depending on the material used for the backing, these waves can either be reflected or transmitted out. The reflective backing, e.g. air, is used to maximize the transducer efficacy, but it can also introduce ringing which limits the bandwidth. Proper matching layers can mitigate this ringing. A transmitting backing layer on the other hand will absorb the waves, making it easier to obtain

a larger bandwidth. However, this cause leaking of energy out the back, reducing the efficacy of the transducer.

2.2 Material characteristics

2.2.1 Mixing

Making samples usually requires the use of several materials, both solid and liquid. In many cases it also requires different materials to be mixed together, usually to create new compounds with certain properties. When mixing several different materials, it is necessary to know how much is present of one compared to the other, as this, amongst other things, determine different properties of the final compound. How much is present of one material compared to the other is usually presented as a fraction, either of mass or of volume. In mathematical terms, the volume fraction can be written as

$$V_\phi = \frac{V_{M1}}{V_T} = \frac{V_{M1}}{V_{M1} + V_{M2}} \quad (2.9)$$

Where V_{M1} and V_{M2} are the volumes of materials 1 and 2, and V_T is the total volume of the mix, which can also be written as the sum of the volumes of materials 1 and 2. The volume fraction will be used in this case.

The volume fraction of the finished compound is usually known, as it is determined by the desired properties of the finished material. However, the definition of density can be used to rewrite equation (2.9) into an expression for the mass of particles, in this case MPS, that has to be added to a certain mass of glue to get the desired volume fraction of particles in the finished compound:

$$M_p = V_\phi \frac{M_g}{\rho_g} \frac{\rho_p}{1 - V_\phi} \quad (2.10)$$

Here M_g is the glue mass and ρ_p and ρ_g are the particle density and glue density, respectively.

The MPS consists of a polymer core and a thin metallic layer, which must both be taken into account when calculating the density of the particles. The total mass of the particle is the sum of the core mass and the metal layer mass, while the volume is a sum of the volume of the core and the volume of the metal layer, giving

$$\rho_p = \frac{M_p}{V_p} = \frac{M_c + M_M}{V_c + V_M} \quad (2.11)$$

It is however impossible to measure the mass of the core and the metal layer alone, making this form of the expression useless when it comes to calculating the particle density. If the definition of density is used to replace the masses with material densities and volumes, and the volumes are replaced by the sphere size parameters, a new, more useful expression is revealed:

$$\rho_p = \frac{\rho_c R_c^3 + \rho_M ((R_c + d_M)^3 - R_c^3)}{(R_c + d_M)^3} \quad (2.12)$$

Where ρ_c and ρ_M are the core and metal layer densities, respectively, R_c is the core radius and d_M is the metal layer thickness. This reasoning used for finding the particle density can also be used to find the density of the system

$$\rho_s = \frac{M_T}{V_T} = \frac{M_c + M_M + M_g}{\frac{M_c}{\rho_c} + \frac{M_M}{\rho_M} + \frac{M_g}{\rho_g}} \quad (2.13)$$

This can be rewritten using the volume fraction, so that it becomes

$$\rho_s = V_\phi \rho_p + (1 - V_\phi) \rho_g \quad (2.14)$$

2.2.2 Heat

Heat can be created in all the layers of the ultrasound transducer through loss mechanisms. The loss is mechanical for the backing layer and the matching layer, while the total loss of the piezoelectric element is a combination of elastic, dielectric and piezoelectric loss. The losses in the piezoelectric can be represented by adding an imaginary term to the elastic, dielectric and piezoelectric material parameters, often denoted the *loss tangent*. This results in the formulation

$$c_E^* = c_E(1 - j \tan \gamma) \quad (2.15)$$

$$\epsilon_S^* = \epsilon_S(1 - j \tan \delta) \quad (2.16)$$

$$e^* = e(1 - j \tan \theta) \quad (2.17)$$

where $\tan \gamma$, $\tan \delta$ and $\tan \theta$ are the elastic, dielectric and piezoelectric loss, respectively. Another formulation of the loss factor is the quality factor, Q . This is defined as the ratio of the total stored energy over the energy loss. [12] The heat created by the loss mechanisms is a result of the energy absorbed from the ultrasound signal and the conversion between the electrical and mechanical domain being absorbed by the material and converted into heat. The different loss mechanisms work in different ways, and can result in either isotropic loss or anisotropic loss. Isotropic loss assumes that the loss mechanisms is the same in all directions, and therefore the loss is the same in all directions, and can be represented by the quality factor. For anisotropic loss on the other hand, the loss mechanisms differ in different directions resulting in the heat loss in certain directions being bigger than in other directions, and can be represented by loss tangents.

Loss mechanisms in the transducer will generate heat, which must be transported away from the structure. Heat transportation can happen if a temperature gradient is present, with energy being transferred from high temperature regions to low temperature regions. This happens either through conduction, convection or radiation. Conduction occurs in stationary mediums, like stationary fluids or solids. Heat is transferred through motion of electrons or as lattice waves induced by the atomic motion. Convection is heat transfer related to the motion of fluids, and can be divided into natural convection and forced convection. Natural convection is when the flow is a result of the warmer fluid being lighter than the colder fluid, causing the heated fluid to rise and leave room for the colder fluid to be heated. With forced convection, the movement of the fluid is helped by an outside force. Radiation is the transfer of heat through emission of

electromagnetic waves, making radiation the only heat transfer method that does not need a material to transfer heat. [13]

Of the three heat transfer methods, only conduction is relevant when it comes to the interior heat transport of the ultrasound transducer, and the material property which describes this form of heat transfer is the thermal conductivity, κ . This property quantifies how well the material can conduct heat and can vary largely between different materials. The ones with the highest conductivity are metals, due to the crystalline build and many free electrons. Other crystalline materials, like ceramics, also have a high conductivity, while polymers, with little crystallinity and few free electrons, tend to have a low conductivity. [3] This property affects the heat flux of the material, which is the rate at which the heat is transferred in a direction per unit area perpendicular to the direction of transfer. The thermal conductivity can in this sense be seen as the transport property, where the relation between the two given by

$$\phi = \kappa \nabla T \quad (2.18)$$

Where ϕ is the heat flux, κ is the thermal conductivity and ∇T is the temperature gradient in the system, that is

$$\nabla T = \frac{\partial T}{\partial x} \vec{i} + \frac{\partial T}{\partial y} \vec{j} + \frac{\partial T}{\partial z} \vec{k} \quad (2.19)$$

Under the condition that heat transfer is only, or mostly, happening in one direction, the expression for the temperature gradient can be simplified to the direction in question. For steady state conditions, that is when the process do not change with time, and linear distribution of the temperature is assumed, the gradient can be simplified even more, to

$$\frac{dT}{dx} = \frac{T_2 - T_1}{L} \quad (2.20)$$

Where T_2 and T_1 are the temperatures at the opposite edges driving the temperature difference, and L is the distance between the two boundaries. [13]

2.3 Models

When building new structures, modeling can be important, as it provides a prediction of the behavior of the finished structure before anything is made. The process can be done in one dimension, two dimensions or three dimensions, where the finished model get more complex the more dimensions is added.

2.3.1 One-dimensional equivalent model

The one-dimensional model for an ultrasound transducer describes the thickness vibration mode of the transducer. Several one-dimensional models exist, with Mason model and Krimholtz, Leedom and Mattei (KLM) model being the two most common. The two models build on the same physical assumptions and give identical results, although the implementations are different. [1]

In the Mason model, the transducer can be represented as a three-port model, where two of the ports are mechanical and one is electrical. As would be assumed, the mechanical ports represent the mechanical connections, while the electrical connection is represented with the electrical ports. The conversion between

the two domains is represented by an ideal transformer, which conserves the power in the transformation. [14] The model is shown in Figure 2.3.

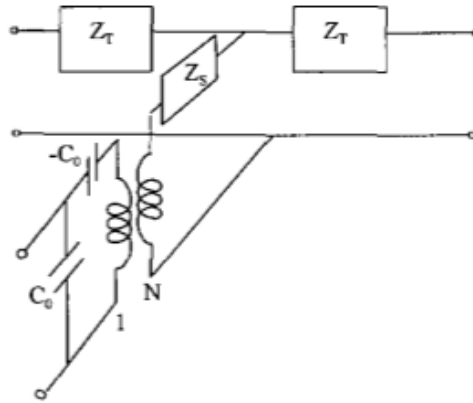


Figure 2.3: The Mason equivalent circuit model for an electro-mechanical transducer.

The model links the forces F_1 and F_2 and velocities u_1 and u_2 on the two mechanical ports (front and back) to the voltage V and current I on the electrical port. The impedances Z_T and Z_S represent the mechanical transmission line, C_0 is the clamped electrical capacitance, and the transformer represents the conversion between the electrical and mechanical energy. From S. Sherrit et.al "Comparison of the Mason and KLM Equivalent Circuits for Piezoelectric Resonators in the Thickness Mode", 1999 [14]

The three-port model is a representation of the piezoelectric element, with the two mechanical ports representing the front and back face of the element. The matching layer and backing layer can be represented with two-port mechanical models, and these can be cascaded to model the entire transducer. The model uses electrical equivalent components in the circuit, though for the electrical side these are actual electrical elements, while they are equivalents for the mechanical side. The governing equations for the model shown in Figure 2.3 are given in Table 2.1. The equations are given in terms of the material constants of the free resonator, as they show the relationship between these constants and the Mason equivalent model. [14]

Table 2.1: Governing equations for the Mason model alone and common with KLM

Common for Mason and KLM model	Mason model
$k_t^2 = \frac{e_{33}^2}{c_{33}^D \epsilon_{33}^D}$ (2.21)	$Z_T = iZ_0 \tan\left(\frac{\Gamma t}{2}\right)$ (2.26)
$h_{33} = k_t \sqrt{\frac{c_{33}^D}{\epsilon_{33}^S}}$ (2.22)	$Z_S = -iZ_0 \csc(\Gamma t)$ (2.27)
$C_0 = \frac{\epsilon_{33}^S A}{t}$ (2.23)	$N = C_0 h_{33}$ (2.28)
$Z_0 = A \sqrt{\rho c_{33}^D}$ (2.24)	
$\Gamma = \omega \sqrt{\frac{\rho}{c_{33}^D}}$ (2.25)	

In the equation definitions ϵ_{33}^S is the clamped complex dielectric constant, c_{33}^D is the open circuit elastic stiffness, k_t is the complex electromechanical coupling, h_{33} is the piezoelectric constant, C_0 is the clamped capacitance, Z_0 is the characteristic impedance of the piezoelectric material, and Γ is the wave number in the thickness direction. The equations which are specific for the Mason defines Z_T and Z_S which are the impedances in the mechanical part as seen in Figure 2.2, and N is the turns ratio for the transformer.

Xtrans is a MATLAB program which implements the Mason model to do one-dimensional simulations of transducers. It was developed at the Department of Circulation and Medical Imaging at NTNU, and will be used in this thesis to determine some of the properties of the sphere layer.

2.3.2 Finite Element Modeling (FEM)

The partial differential equations, PDEs, for a problem may be impossible to solve analytically, so approximate PDEs are made through usage of numerical model equations. These can be solved by numerical methods like the finite element method, FEM. With FEM, the geometry is divided into smaller pieces constructed in a one, two or three-dimensional mesh, where a denser mesh provides a solution closer to the actual solution than a wider mesh. The properties to be examined are computed from the equations and modeled into a larger system representing the full problem. This then results in a more complex equation for the complete structure, making the method a good alternative for solving complicated domains. [15]

Constitutive equations can be used to express the laws of physics in the FEM simulation. The scalar version of the constitutive equations for the piezoelectric element is also the basis for both the Mason model and the KLM model. For the piezoelectric element, the constitutive equations are

$$\mathbf{T} = c^E \mathbf{S} - e \mathbf{E} \quad (2.29)$$

$$\mathbf{D} = e^T \mathbf{S} + \epsilon^S \mathbf{E} \quad (2.30)$$

This is the stress-charge form of the equations, where T is the stress, D is the electric flux density, S is the strain vector and E is the electric field, and the fat text means it is a vector. c^E is the elasticity matrix, e is the piezoelectric matrix, and ϵ^S is the dielectric matrix. The superscript letters, E for the elasticity matrix and S for the dielectric matrix, means the matrices were evaluated at constant value. For the elasticity the evaluation is at constant electric field, while for the dielectric matrix it is for constant mechanical strain. For anisotropic materials, the matrices could become large with many values. [16, 17] A material can however become transversely isotropic if the poling axis coincides with a material symmetry axis. This means all directions perpendicular to the symmetry axis are equivalent and all planes perpendicular to the axis are isotropic, which is the case for piezoelectric ceramics, PZT, but not piezoelectric single crystals. For the isotropic case, it will then be possible to reduce the number of constants, both for the elasticity matrix, the piezoelectric matrix and the dielectric matrix, which will gain the form [18]

$$c^E = \begin{bmatrix} c_{11} & c_{12} & c_{13} & 0 & 0 & 0 \\ c_{12} & c_{11} & c_{13} & 0 & 0 & 0 \\ c_{13} & c_{13} & c_{33} & 0 & 0 & 0 \\ 0 & 0 & 0 & c_{44} & 0 & 0 \\ 0 & 0 & 0 & 0 & c_{44} & 0 \\ 0 & 0 & 0 & 0 & 0 & c_{66} \end{bmatrix} \quad (2.31)$$

$$e = \begin{bmatrix} 0 & 0 & 0 & 0 & e_{15} & 0 \\ 0 & 0 & 0 & e_{15} & 0 & 0 \\ e_{31} & e_{31} & e_{33} & 0 & 0 & 0 \end{bmatrix} \quad (2.32)$$

$$\epsilon = \begin{bmatrix} \epsilon_{11} & 0 & 0 \\ 0 & \epsilon_{11} & 0 \\ 0 & 0 & \epsilon_{33} \end{bmatrix} \quad (2.33)$$

3 Materials and method

In order to characterize the glue-sphere layers, both simulations and physical experiments were necessary. Samples with a monolayer of spheres were made to determine the effect of such a layer, but also to determine the properties of the layer, through fitting of Xtrans simulated impedance spectra to the measured spectra. No established method exists for making such monolayers, making it necessary to determine a reliable method for fabricating such layers, before making samples with PZT. In addition to monolayers, thicker 0-3 composites consisting of MPS and glue were made to determine the speed of sound of the compound through measurements. Simulations were done to determine how well the measurements correspond to the theoretical models. Thermal simulations were done to determine the thermal conductivity, as this is the most important parameter for heat transfer.

3.1 Trial samples

3.1.1 Making the samples

The first trial samples with monolayer of MPS and glue were made at Conpart with a PZT that already had a wrap-around electrode. The wrap around electrode allowed access to the electrode on the bottom through a connection to the top of the plate.

The MPS and glue mix was created as follows

- A pre-mix was made by pouring approximately 5 g of resin, PY 302-2, in the cup and measure the actual weight, which was then multiplied with 0.35 to get the weight of hardener, D-230, to add.
- The pre-mix was put in a mixer for 2.5 minutes at 2000 rpm to get an even solution
- A desired weight of the pre-mix was taken out and added into another cup.
- The weight of spheres to add to the pre-mix was found using volume fraction, in this case approximately 10% volume spheres.
- The cup with the spheres and glue was stirred a little with a plastic stick and then put in the mixer for 2.5 minutes at 2000 rpm..

The weight used for the two sphere types and the mixing type is shown in Table 3.1

Table 3.1: Weights and type of mixer used for the first sphere mixes

Mix	Weight glue (g)	Weight spheres (g)	Mixing
20µm sphere mix	1.999	0.301	Mixer
40µm sphere mix	3.025	0.482	Vacuum mixer

A plastic stick was used to add the sphere filled glue to the load material, which in these experiments were either glass, Si or tungsten carbide (WC). The PZT was placed on top with the glue approximately in the center of the PZT, and put in an oven at 100°C for approximately 30 minutes to harden. Some samples stayed longer in the oven. A weight of 1.8 kg and 320 g were used to press the PZT down on the load during curing, and a small piece of tape was used to hold the PZT in place. The finished samples are shown in Figure 3.1 to 3.3. Each sample was short circuited to ensure it was discharged before the impedance was measured.

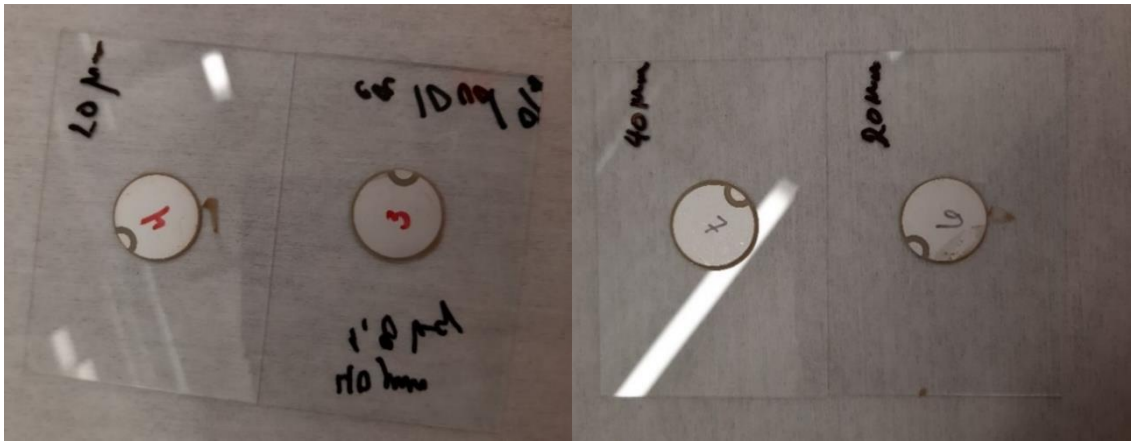


Figure 3.1: Trial samples 3 and 4 (left) and trial sample 6 and 7 (right)



Figure 3.2: Trial sample 8 (left) and trial samples 10 (40 μ m), 11 (20 μ m), 17 and 18 (right)



Figure 3.3: Trial samples 1, 5, 13, 14, 15 and 16

The samples made from PZT 1, 5, 10, 11 and 14 were discarded. Samples 1 and 5 were discarded because the PZT was outside the load, as can be seen in Figure 3.3. Samples 10 and 11 were discarded because the epoxy glue was squeezed out and covered the PZT, as can be seen in Figure 3.2, and sample 14 was discarded because the PZT did not stick to the load. PZT number 12 broke before it was glued to a load,

while PZT number 2 broke while measuring the initial impedance. The sphere diameter, load type and resonance frequency for the different samples are summarized in Table 3.2.

Table 3.2: Samples with the load type, MPS diameter and resonance frequency of piezo, as well as whether the sample was discarded or not.

Sample nr.	Load material	Sphere diameter [μm]	Frequency [MHz]	Result
Trial 1	Si (silicon)	20	5	Discarded (outside load)
Trial 2	---	---	5	Discarded (broken)
Trial 3	Glass	40	5	Ok
Trial 4	Glass	20	5	Ok
Trial 5	WC (tungsten carbide)	20	5	Discarded (outside load)
Trial 6	Glass	20	5	Ok
Trial 7	Glass	40	5	Ok
Trial 8	Glass	20	5	Ok
Trial 10	Glass	40	8	Discarded (overflow of glue)
Trial 11	Glass	20	8	Discarded (overflow of glue)
Trial 12	---	---	8	Discarded (broken)
Trial 13	WC (tungsten carbide)	20	8	Ok
Trial 14	WC (tungsten carbide)	20	8	Discarded (not bonded)
Trial 15	WC (tungsten carbide)	20	8	Ok
Trial 16	WC (tungsten carbide)	20	8	Ok
Trial 17	Glass	20	8	Ok
Trial 18	Glass	20	8	Ok

All the samples were diced and the cross section was studied in an optical microscope (*Carl Zeiss Jena Neophot 32*), which was also used to measure the thickness of the layer. The results were then loaded into MATLAB, and the impedance was calculated from a Mason equivalent circuit model implemented in the MATLAB program Xtrans. The acoustic properties of the glue layer were adjusted to a best fit between the impedance spectra simulated in Xtrans and the measured impedance spectra. Acoustic properties of the glass coverslips used as loads were found by measurements, which is elaborated below. Acoustic properties for tungsten carbide (WC) were taken from the literature [19].

3.2 Mixing and loading values

3.2.1 Load values

Two types of glass were used in the samples, one large of size 5.2 cm x 7.6 cm, and one small of size 2.6 cm x 7.6 cm. Both glass types were coverslips for use in microscopes, with the larger being used for the 5MHz PZTs and the smaller being used for the 8MHz PZTs in the trial samples. The speed of sound and the acoustic impedance of the glasses were found by measuring the acoustic transmission through and reflections from the glass samples using the setup of Figure 3.4. The working principle of this setup is shown in Figure 3.5. The larger glass was diced into four pieces, while the smaller was diced in two to fit

them into the setup. The size of the glass before dicing, and the size of the glass samples after dicing is summarized in Table 3.3, together with the thickness and the weight of the samples after dicing. The abbreviation L means the sample is from the large glass, while S means it is from the small glass.



Figure 3.4: Speed of sound setup; measurement setup (left) and oscilloscope, signal source and computer setup (right).

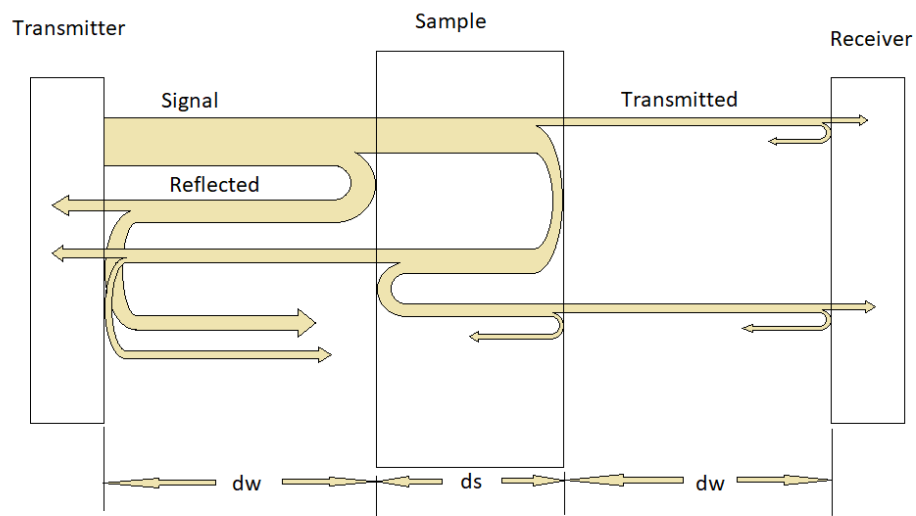


Figure 3.5: Working principle of the speed of sound measurement.

The arrows into the transmitter and receiver indicates registered signals, and the time difference between these are taken to calculate the speed of sound. The signal will keep being reflected and transmitted until it is too small to register.

Table 3.3: Size parameters and weight of the glass samples in the speed of sound measurement.

The two first values are the size of the glasses before dicing, while the other are the measurement after dicing. The number is to separate the samples.

	Length of sample [cm]	Width of sample [cm]	Weight [g]	Average thickness [mm]
Large glass (L)	7.6	5.2	---	---
Small glass (S)	7.6	2.6	---	---
Sample L1	4.0	2.4	2.325	0.985
Sample L2	4.0	2.8	2.761	0.989
Sample L3	3.6	2.8	2.488	0.987
Sample L4	3.6	2.4	2.074	0.985
Sample S1	4.0	2.6	2.793	1.097
Sample S2	3.6	2.6	2.479	1.098

The samples were too thin to determine the speed of sound from the time difference between the signals, so the power spectra, which showed clear peaks for maximum transmission, was used instead. The results were loaded into MATLAB, which determined the frequency at the maximum transmission peaks, the resonance frequency, which was then used in equation (2.1) to calculate the speed of sound. Maximum transmission happens when the thickness of the sample is half the wavelength.

3.2.2 Density of glue and MPS

Epo-tek 301-2 is a two-component epoxy consisting of Epo-tek 301-2 part A and Epo-tek 301-2 part B. The density of Epo-tek 301-2 was found by mixing 3g of part A and 1.05g of part B to make a pure sample. After mixing in the speed mixer for 4 minutes, the sample was cured for 3hours, and then grinded down so that both sides were flat. The weight of the sample was 3.672 ± 0.006 g, the average thickness was 3.176 ± 0.017 mm and the radius was approximately 3.6 ± 0.1 cm, and these values were used to calculate the density.

Density of the spheres were calculated using equation (2.12). The radius of the cores and the thickness of the metallic layer were given from Conpart. The density of the core material (PMMA) was found in [20]. The parameters used for the calculations are shown in Table 3.4.

Table 3.4: Values for calculating particle density

	20 μ m spheres	40 μ m spheres
Radius core (R_C)	10 μ m	20 μ m
Thickness Ag-layer (d_M)	160 nm	160 nm
PMMA density (ρ_{PMMA})	1.16 g/cm ³	1.16 g/cm ³
Ag-density (ρ_{Ag})	10.49 g/cm ³	10.49 g/cm ³

3.3 0-3 Composites

The speed of sound samples are 0-3 composites, which are much thicker than a monolayer, made to be used for measuring the speed of sound.

3.3.1 Mixing trial

Samples without PZT were made using Epo-tek 301-2 to see how the MPS and the glue mixed and to try to make 0-3 composites for speed of sound measurements.

The calculated masses of Epo-tek 301-2 and spheres for the samples are shown in Table 3.5. Formula 2.13 was used to calculate the sphere mass to be added, using 1.49 g/cm^3 for the density of the $20\mu\text{m}$ spheres and 1.27 g/cm^3 for the density of the $40 \mu\text{m}$ spheres due to the assumption of styrene core, later corrected for a PMMA core. For the Epo-tek 301-2 the density in the data sheet for part B, 0.95 g/cm^3 , was used. The density of mixed Epo-tek 301-2 was found after these samples were made. The name for the samples, SoS, in Table 3.5 is short for Speed of Sound.

Table 3.5: Calculated masses for the mixes

	Byk	Spheres	Epo-tek 301-2 part A	Epo-tek 301-2 part B
SoS1	No	0.71g ($20 \mu\text{m}$)	3.0g	1.05g
SoS2	No	0.60g ($40 \mu\text{m}$)	3.0g	1.05g
SoS3	Yes	1.18g ($20 \mu\text{m}$)	5.0g	1.75g
SoS4	Yes	1.00g ($40 \mu\text{m}$)	5.0g	1.75g
Epo-tek	No	---	5.0g	1.75g

Sample 3 and 4 was also added two drops of Byk-A 501, which is an agent that reduces surface tension and should improve wetting of the spheres [21], to see if it could prevent sedimentation of the MPS. The samples were mixed a little by hand before it was put in a speed mixer (*Speed Mixer DAC 150 FVZ-K*) at 2500 rpm for 4 minutes. All samples were put straight into the oven for 3 to 4 hours after the speed mixer, at a temperature of 80°C . The samples for the $20 \mu\text{m}$ spheres after speed mixing are shown in Figure 3.6, while the cured samples are shown in Figure 3.7.

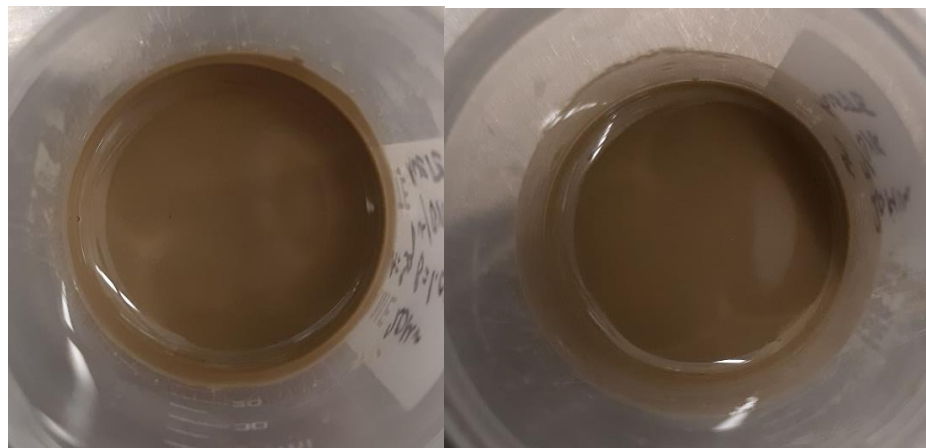


Figure 3.6: $20 \mu\text{m}$ spheres and Epo-tek 301-2 without Byk (left) and with Byk (right)

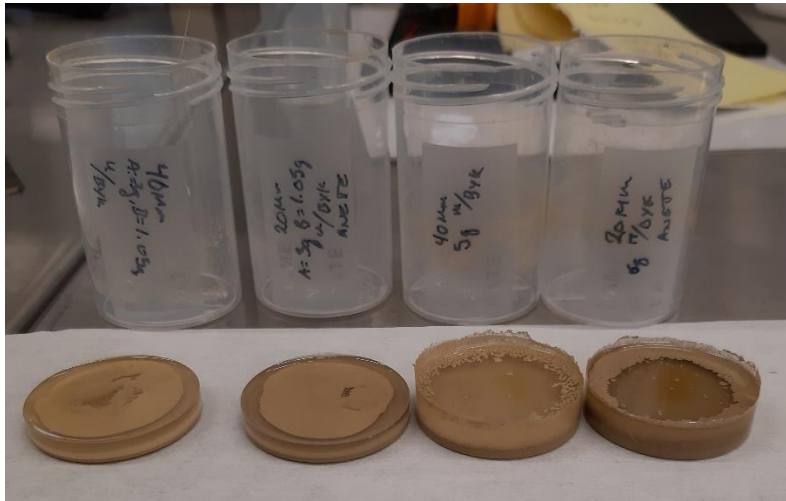


Figure 3.7: Mixing trial samples after curing (from left): 40 μm without Byk, 20 μm without Byk, 40 μm with Byk and 20 μm with Byk

The samples were cut through the center using a hacksaw, and then grinded down. The grinding was first done with a coarse paper (grit 240), and then finer (grit 600) and finer (grit 800) until the edge was smooth enough to study in the optical microscope.

3.3.2 Speed of sound samples

Previous work using metal coated spheres [22] had problems with sedimentation of the spheres, as seen in the initial tests, though this was with another type of glue. This was mitigated by letting the composite begin the curing process and then spin the solution to mix it again.

The next speed of sound samples were made with the same process as above, with an initial mixing of the Epo-tek 301-2 parts and then adding the correct weight of spheres. The pure Epo-tek 301-2 was mixed for 2 minutes, while the glue-sphere mix was spun for 2.5 minutes, both at 2500 rpm. After the second mixing, the composites were vacuumed for 15 minutes and then put in the oven at 80°C. After 30 minutes, the cups with the composites were taken out and spun for 1-2 minutes, before being placed back in the oven. The samples were then checked every five minutes until they had been in the oven for a total of 1 hour. The speed of sound samples SoS5 to SoS9 were made for the silicon monolayer samples. Rests from the PZT samples were tried to be used, but experienced sedimentation during curing. The masses used for the samples are shown in Table 3.6.

After the curing was done, the samples that could be used for speed of sound measurements were taken out and grinded. This was first done by hand at paper with grit 240 to remove the big height differences, then a grinding machine (*MultiPrep system for grinding and polishing*) was used to make the two sides parallel. Wax was used to stick the samples to the holder while the machine grinded one side, before flipping the sample and repeating the process. When both sides of the sample were approximately parallel, another round of grinding was done, this time with paper with grit 600, to smoothen out the surface. The speed of sound setup shown in Figure 3.4 and Figure 3.5 was then used to measure the speed of sound in the samples, and this, together with the calculated density, was used to find the acoustic impedance. Table 3.7 shows the

average thicknesses of the samples, while Figure 3.8 shows the finished speed of sound samples. More details on the fabrication and images can be found in appendix E.

Table 3.6: Weight of MPS and glue added to the speed of sound 0-3 composites

Sample	Sphere type	Added weight (spheres)	Epo-tek 301-2
SoS1	20 μm	0.69 g	4.03 g
SoS2	40 μm	0.62 g	4.11 g
SoS3	20 μm	1.20 g	6.65 g
SoS4	40 μm	1.05 g	6.74 g
SoS5	20 μm	0.64 g	4.13 g
SoS6	40 μm	0.53 g	4.11 g
SoS7	40 μm	0.49 g	4.10 g
SoS8	20 μm	0.46 g	3.03 g
SoS9	40 μm	0.40 g	3.03 g
SoS10	20 μm	0.46 g	3.01 g
SoS11	20 μm	0.47 g	3.05 g
SoS12	40 μm	0.40 g	3.00 g
SoS13	40 μm	0.41 g	3.01 g

Table 3.7: Average thickness and the weight of the speed of sound samples

Sample	Thickness [mm]	Weight [g]
SoS5	1.971 ± 0.0314	2.366
SoS6	1.894 ± 0.0510	2.230
SoS8	1.976 ± 0.0303	2.357
SoS9	1.707 ± 0.0168	1.936
SoS10	1.775 ± 0.0284	2.083
SoS11	1.801 ± 0.0652	1.983
SoS12	1.610 ± 0.0244	1.773
SoS13	1.348 ± 0.0188	1.524

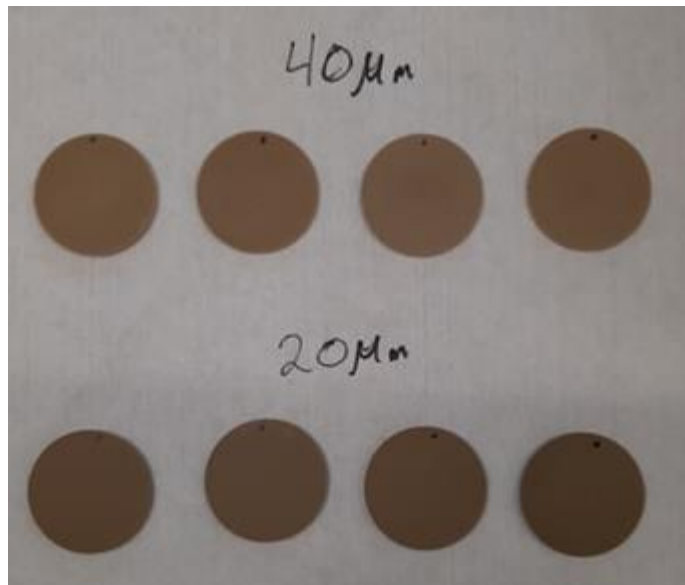


Figure 3.8: The finished speed of sound samples

3.4 Monolayer method

Samples of silicon and glass were made to test the method for making monolayers, as the trial samples showed air bubbles and layers which were not monolayers. The method for making the glue-sphere mix was almost the same as the with the trial samples, only Epo-tek 301-2 was used as the glue, and mixing of Epo-tek part A and Epo-tek part B was done at 2500 rpm for 2 minutes. The weight of the spheres and the Epo-tek 301-2 used for the mix are shown in Table 3.8. After adding the spheres and glue in the same cup, the mixes were put in the speed mixer for 2.5 minutes at 2500 rpm, and then vacuumed for 15 minutes.

Table 3.8: Weights added to create mixes for the silicon samples

Sample	Weight Epo-tek (added)	Weight spheres (added)
20µm, 10vol% (1)	2.02 g	0.309 g
40µm, 10vol% (1)	3.06 g	0.403 g
20µm, 10vol% (2)	3.03 g	0.463 g
40µm, 10vol% (2)	3.01 g	0.401 g

A small plastic stick was used to apply the mix, with only one drop being placed on the glass. The size of the drop depended on how much the plastic stick had gathered of the mix. Different solutions were used for the tape. On the S samples the tape was placed lightly over the silicon layer after the silicon had been placed on top of the glue drop, while the L samples had the tape on the Si-piece before placing it on top of the drop. The loading method for the different samples are summarized in Table 3.9, with the weights having a mass of 675 g, 835 g and 1.12 kg. Sample 12 was discarded, as the spheres could not spread out. The finished S samples are shown in Figure 3.9.

Table 3.9: Summary of the loading method and curing time of the Si samples.

Sample	Loading	Removal of load	Curing time [h]
S4	Weight	Before put in the oven	1.5 (rest curing in air)
S5	Weight	Before put in the oven	1.5 (rest curing in air)
S6	Weight	Before put in the oven	1.5 (rest curing in air)
S7	Weight	No	1 (rest curing in air)
S8	Weight	No	1 (rest curing in air)
S9	Weight	No	1 (rest curing in air)
L1	Weight	After put in the oven	4
L3	Tape	No	3
L7	Weight	No	3
L8	Tape	No	4
L11	Weight	After put in the oven	4
L12	Weight	No	3

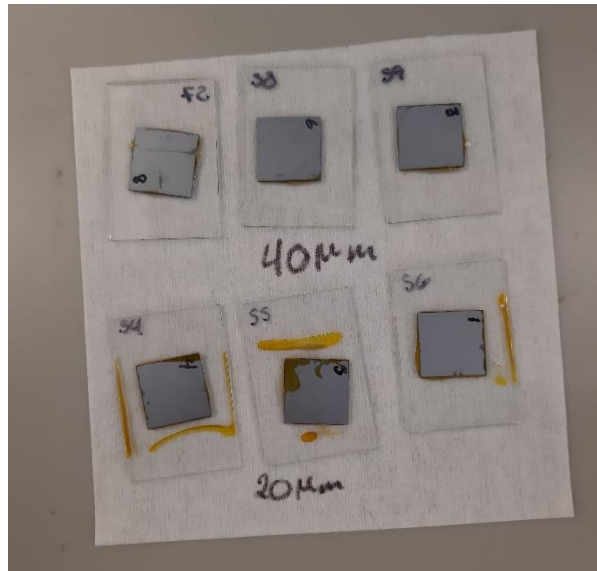


Figure 3.9: Finished silicon monolayer samples S4 to S9.

3.5 Monolayer PZT

3.5.1 PZT with wrap-around

The PZT plates used for the PZT samples were of type Pz27 (Ferroperm, Denmark) in the shape of a 4MHz piezoelectric plate with 3 cm diameter. These had a silver electrode on each side of the plate, which were ground away using paper with grit 600, then it was smoothed using paper with grit 1200, to prepare for a wraparound electrode for easier measurements of the finished samples. After grinding away the original electrode, the Pz27 was diced and sputtered, first with 20 nm Cr for adhesion and then 200 nm Au for the new electrode. The sputtered Pz27 was then diced into 7.5 mm x 5 mm pieces, with a cut halfway into the PZT 2.5 mm from the edge on the long side to make the wrap around. The cross section of the structure with the layers is shown in Figure 3.10 and a finished Pz27 piece from above is shown in Figure 3.11.

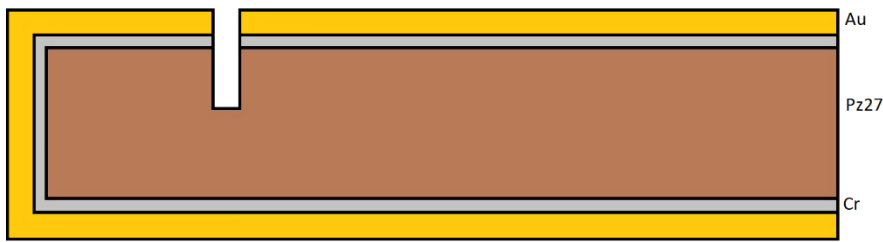


Figure 3.10: Cross section of the Pz27 pieces after creating wrap around.

The yellow area going around the structure is the gold layer, while the grey area is the chromium layer. The brown piece in the middle is the Pz27.



Figure 3.11: Pz27 sample from above after creating wrap around.

Due to time constraints, it was decided to focus on one sphere size. The 40 μm spheres were chosen, as the previously fabricated samples indicated it was easier to make monolayers with this size. The masses of the different constituents used for the glue-sphere mixes, with the samples the mixes were used on, are shown in Table 3.10.

Table 3.10: The weight of Epo-tek 301-2 and spheres used for the mixes for the PZT samples.

The impedance of sample 8, 12 and 13 were measured alone, but was not used to make samples with a load.

Sample	Weight Epo-tek 301-2 (added)	Weight spheres (added)
Sample 1-3	3.01 g	0.415 g
Sample 4-6	3.00 g	0.404 g
Sample 7, 9-10, 15	3.03 g	0.403 g
Sample 11,14	3.01 g	0.401 g

The mix of Epo-tek 301-2 and spheres was the same as with the silicon samples. A pre-mix of Epo-tek 301-2 was made, with approximately 3g being moved to another cup using a pipette and mixed with the spheres. The application of the glue-sphere mix on the load was also the same as for the monolayer case, with the mix being added using the plastic stick and the PZT being placed on top with the glue drop

in the center. A tape was gently placed over to keep the PZT in place and a weight was added on top. The details of the process can be found in appendix D. Figure 3.12 shows the samples that were made with the glass load, while Figure 3.13 shows the samples made with tungsten carbide (WC) load. Sample number 3 had to be discarded due to breaking of the PZT along the cut made to separate the electrodes on the top of the piece.

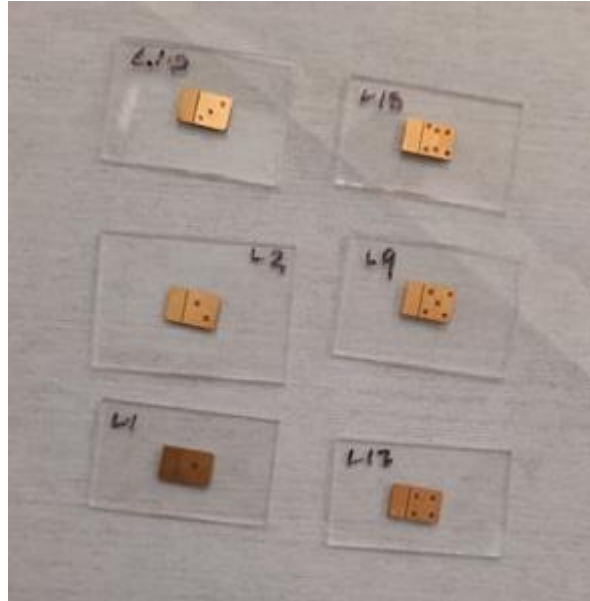


Figure 3.12: Finished samples with PZT, glue-sphere layer and glass load.

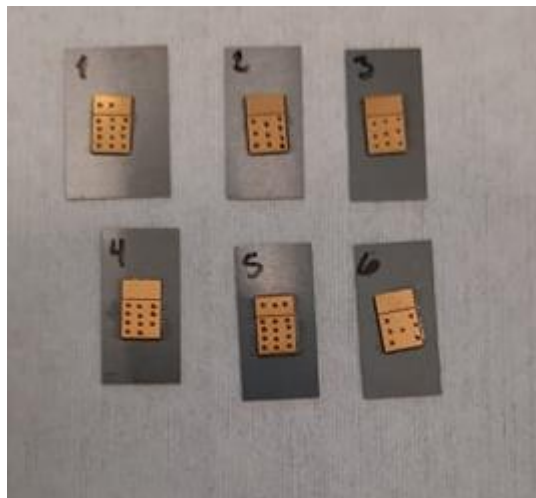


Figure 3.13: Finished samples with PZT, glue-sphere layer and tungsten carbide (WC) load

Electrical impedance of the samples was measured with the *R&S® ZVL Vector Network Analyzers*, and the results were loaded into MATLAB for comparison with the spectra from Xtrans. The glass samples were studied from the underside with the optical microscope, while the tungsten carbide samples, and also the glass samples, were cut to study the cross section.

3.6 FEM modeling

FEM (finite element modeling) models were made of the transducers using COMSOL Multiphysics. FEM models were made for simulation of electrical impedance and of thermal conductance. A description of the major steps to make the models follows.

Geometry: The sphere layer of the structures was built using java programming in the ‘Application Builder’ in COMSOL. The programs for making 2D and 3D sphere layers are given in appendix B and C. The 2D program creates flat geometries with circles representing the spheres, however the layers are representing a 2D version of the sphere layer and is therefore referenced as a sphere layer. The sphere structures were imported into the simulation files for the different models. The rest of the structures, like the piezoelectric material and the load for the transducer models, and a PMMA layer for the heat transfer model was added to the geometry by using the CAD feature in COMSOL, with rectangles used to represent the different layers. These other layers were made of single blocks with size parameters given in the ‘Parameters’ fields in COMSOL to simplify the changes between models.

Materials: COMSOL has a material library, and for the cases where it was possible, this was used. Of the materials in the model, the water, air, PMMA and silver existed in the material library from before, while the Pz27 and Epo-tek 301-2 had to be added from blank materials. The parameter values for the Pz27 were found in the data sheet from Ferroperm [23], which is also given in appendix A, while the Epo-tek 301-2 parameters were found in [24].

Physics: COMSOL combines FEM simulations in several *physics domains*. Which physics domains are needed depends on which properties the model is made to investigate.

3.6.1 Heat model

Both 2D and 3D structures were built for the thermal conductivity simulation. 2D was used to test the methods to be used before implementing in the 3D model. The 2D model could also run two methods for calculating the thermal conductivity, while the 3D model could only run one due to problems with meshing for one of the methods.

The first of the two methods used to determine the thermal conductivity was based on the heat flux through the sphere structure. A ‘Probe’ was used to measure the total heat flux of the structure and then this heat flux was used to calculate the thermal conductivity. This method required the silver layer to be made as a separate domain, and could therefore not be used in the 3D model due to problems with fine enough meshing.

The second method was based on the total heat flux through a two layered structure, where the layers had different thermal conductivity, and where the heat flux would be the same through both layers. A layer of PMMA with the same thickness as the sphere layer was used as a reference layer for this method, which was used both for the 2D and the 3D model, as the silver layer in this case could be modeled through the thin layer function in COMSOL.

Several different sphere geometries were tried; some with random distribution of the spheres and random sphere radius, some with the same sphere radius and random distribution and some with random sphere

radius and random distribution in the x-direction, but same y-coordinate within the layer. 3D models were also made with all the spheres having the same radius, and the distribution being random. Examples of all the geometry types are shown in Figure 3.14 to Figure 3.17. An overview of the samples with size parameters, sphere diameters and geometry type are shown in Table 3.11.

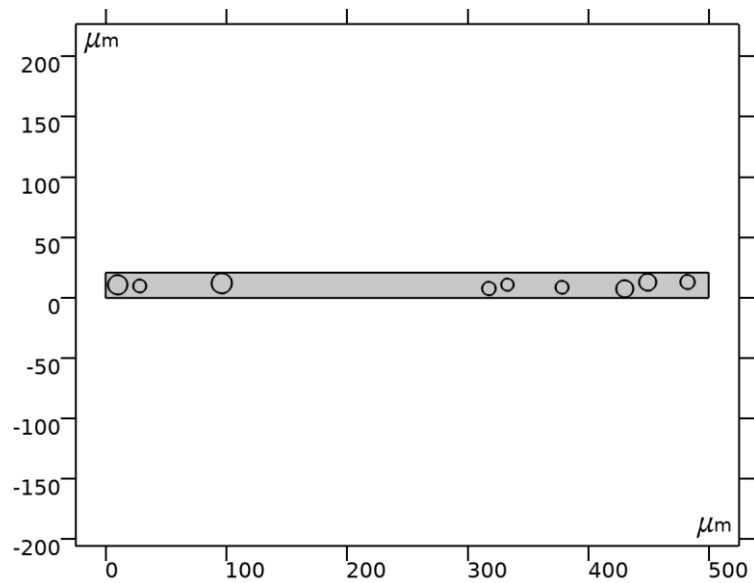


Figure 3.14: Geometry type nr. 1.

All the spheres have random size and random distribution within the glue layer.

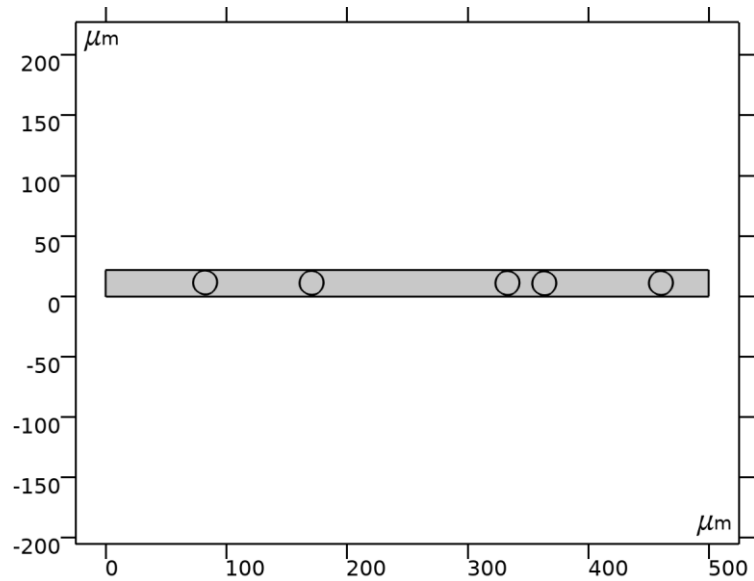


Figure 3.15: Geometry type nr. 2.

All spheres have the same size, with distribution being random throughout the glue structure

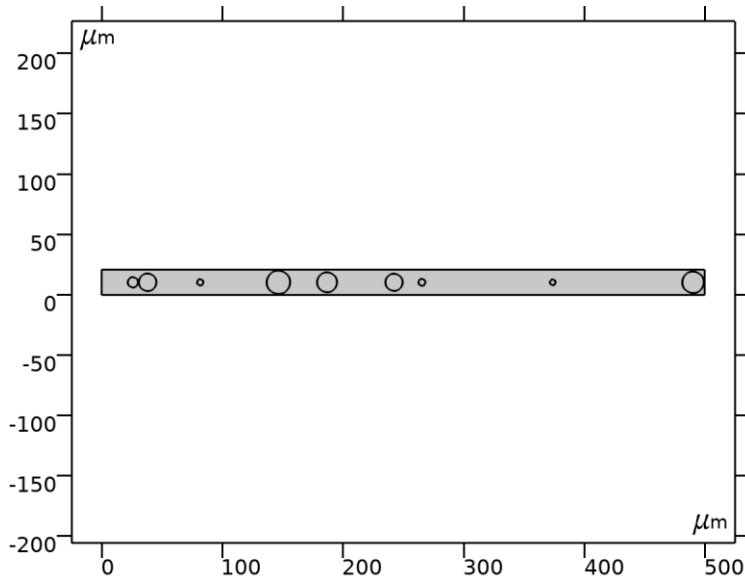


Figure 3.16: Geometry type nr. 3.

The spheres have different radius at the given cross section, and is randomly distributed along the length of the glue layer, while height placement is set in the middle of the height of the glue layer

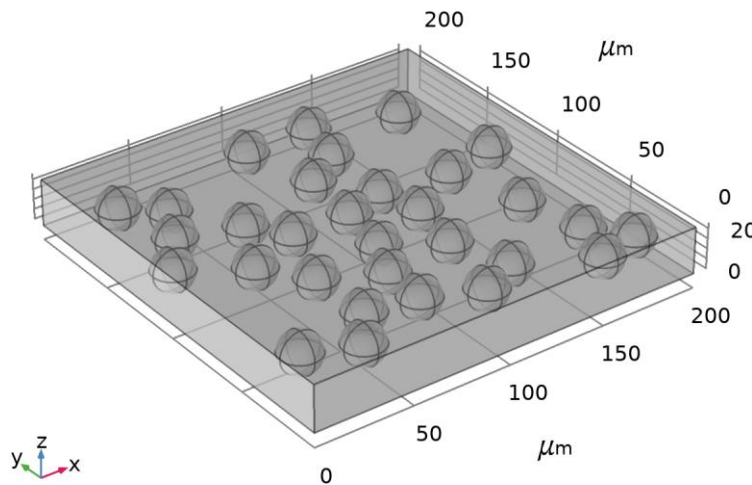


Figure 3.17: 3D geometry for the thermal conductivity simulation.

All spheres have the same size and is randomly distributed throughout the structure.

The materials were added to the domains, with PMMA on the main domain and inside the spheres, and silver, Ag, on the sphere surfaces. For the heat flux method, the silver was added to the domain in between two circles, while for the comparison method, a thin layer, denoted a 'Single Layer Material' in COMSOL, had to be made and applied. The material to which the sphere layer was compared in the comparison method was also PMMA.

The simulation to find the thermal conductivity only needed the *Heat Transfer in Solid* physics node. A constant temperature of 200K was set at the bottom boundary of the geometry, while another constant temperature of 400K was set at the top boundary. Both temperatures, 200 K and 400 K, are unrealistic for a transducer, but was set to clearly see the effect. The sides of the structure were set to be thermally

insulated, with the surrounding temperature being room temperature. For the comparison method a ‘Thin Layer’ had to be added to the sphere boundaries in the physics to indicate the properties of the silver layer, and ‘Heat Flux’ was applied to allow heat flow thru the layer. All the geometries for the 2D 20 μm sphere structures were 21 μm thick, while the geometries for the 2D 40 μm sphere structures had a thickness of 42 μm .

Table 3.11: Overview of the geometry parameters used for thermal conductivity simulations

Sample	2D		3D		
	Sphere size	Geometry	Width [μm]	Thickness [μm]	Width/depth [μm]
Nr. 1	20 μm	Type nr. 1	500	23	200
Nr. 2	20 μm	Type nr. 1	500	23	200
Nr. 3	20 μm	Type nr. 1	500	23	200
Nr. 4	20 μm	Type nr. 1	500	23	200
Nr. 5	20 μm	Type nr. 1	500	23	200
Nr. 6	20 μm	Type nr. 1	200	23	200
Nr. 7	20 μm	Type nr. 1	200	23	200
Nr. 8	20 μm	Type nr. 1	200	23	200
Nr. 9	20 μm	Type nr. 1	200	23	200
Nr. 10	20 μm	Type nr. 1	200	23	200
Nr. 11	20 μm	Type nr. 2	500	20.5	200
Nr. 12	20 μm	Type nr. 2	500	20.5	200
Nr. 13	20 μm	Type nr. 2	500	20.5	200
Nr. 14	20 μm	Type nr. 2	500	20.5	200
Nr. 15	20 μm	Type nr. 2	500	20.5	200
Nr. 16	20 μm	Type nr. 3	500	20.5	200
Nr. 17	20 μm	Type nr. 3	500	20.5	200
Nr. 18	20 μm	Type nr. 3	500	20.5	200
Nr. 19	20 μm	Type nr. 3	500	20.5	200
Nr. 20	20 μm	Type nr. 3	500	20.5	200
Nr. 21	40 μm	Type nr. 3	1000	44	400
Nr. 22	40 μm	Type nr. 3	1000	44	400
Nr. 23	40 μm	Type nr. 3	1000	44	400
Nr. 24	40 μm	Type nr. 3	1000	44	400
Nr. 25	40 μm	Type nr. 3	1000	44	400
Nr. 26	40 μm	Type nr. 2	1000	40.5	400
Nr. 27	40 μm	Type nr. 2	1000	40.5	400
Nr. 28	40 μm	Type nr. 2	1000	40.5	400
Nr. 29	40 μm	Type nr. 2	1000	40.5	400
Nr. 30	40 μm	Type nr. 2	1000	40.5	400

The mesh for the 2D model was chosen to be a free triangular mesh for all the domains, and the size of the elements were set to ‘Extremely Fine’. For the 3D the mesh was free tetrahedral, with the size being ‘Extra Fine’.

For the heat flux method, a domain probe calculating the total heat flux in the y-direction (ht.tfluxy) was applied to the whole geometry. This was used to find the thermal conductivity of the material by assuming linear distribution of heat and using equation (2.18) to calculate the value. For the comparison method a boundary probe was added to the boundary between the sphere layer and the pure PMMA used for comparison to find the stationary average temperature at the boundary. The assumption that the heat flux was the same throughout the whole structure and that the temperature was linearly distributed in both parts of the structure was used to calculate the thermal conductivity of the sphere layer from the thermal conductivity of the PMMA and the temperature difference in the two parts of the structures.

3.6.2 Impedance model

The COMSOL impedance models were made with size parameters as given for the different transducer samples. Only 2D simulations were made due to problems with making a 3D model of the correct size. Figure 3.18 shows an image of the structure, with a zoomed in image of the sphere layer in Figure 3.19. In the figures, the red area is the piezoelectric element, the green is the hard load glued to the structure, and the blue is the outside load, with the upper part being a perfectly matched layer (PML). The yellow is the sphere layer.

The sphere layer geometry was made with all the spheres having the same diameter, as this was the case for the real spheres. In the creation of the layer, all the spheres were set to have the same y-coordinate, for simpler meshing and faster calculation. The x-coordinate was random.

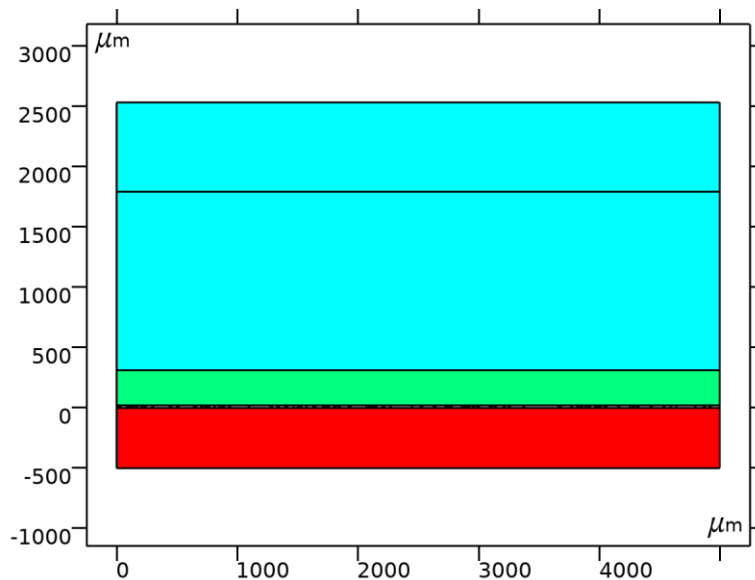


Figure 3.18: COMSOL geometry used in the simulation of the monolayer PZT samples.

The sphere layer, which is too thin to be visible in this drawing, is located between the PZT (red) and the hard load (green). The blue area is air.

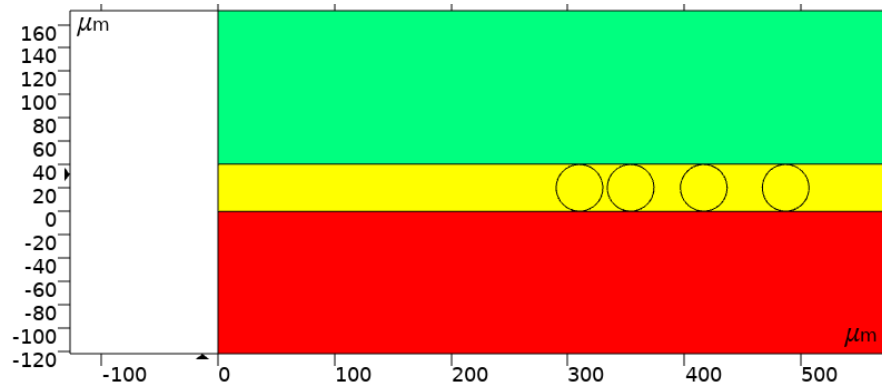


Figure 3.19: Zoomed in image of the sphere layer (yellow) in the impedance COMSOL geometry.

The studies in this case were all for vibrations in air, and this was therefore used as the blue load, with the material properties found in the COMSOL material library. The silver was set as a ‘Single Layer Material’ on the boundary of the circles. Pz27 was set as the piezoelectric material, the core of the spheres was set to PMMA, and the glue around the spheres was set to Epo-tek 301-2. The green load was either glass or tungsten carbide depending on the structure that was simulated.

The physics needed by COMSOL for the impedance model were *Solid Mechanics*, *Electrostatics* and *Pressure Acoustics, Frequency Domain*. The *Pressure Acoustics* was applied to the blue load and PML, with a sound hard wall following the outer boundary. Coupling between the transducer structure and the load was done along the boundary between the glass and the air with the ‘Acoustic-Structure Boundary’ in the Multiphysics node. The *Solid Mechanics* was applied to the whole transducer structure, with the sphere layer and glass being set as ‘Linear Elastic Material’, and the ‘Piezoelectric Material’ being set at the red piezoelectric part of the transducer. ‘Roller’ boundary condition was also applied to the vertical sides of the transducer to indicate that the transducer is part of a larger plate, and a ‘Thin Elastic Layer’ was applied to the sphere boundaries to indicate the silver layer. The only free boundary was the bottom horizontal boundary of the piezoelectric element. The *Electrostatics* was set to the piezoelectric element, with zero charge on the vertical sides, ground on the top horizontal boundary and a terminal on the bottom horizontal boundary.

Loss was added both in the piezoelectric material and the matching layer. This was done in the form of mechanical damping in the *Solid Mechanics*, where the damping in the piezoelectric material was added in the piezoelectric material of the physics and the loss for the sphere layer and the load layer was added in separate ‘Linear Elastic Material’. The losses were in all cases set as isotropic, defined by the loss factor Q_m of the material.

The meshing of the structure was done based on the wavelength in the material of the element in question at resonance frequency, set to 4 MHz. The mesh size of the PZT, the load material and the air were set to have the wavelength in the material at 4 MHz divided by four, $\lambda/4$, as the largest element size, while the smallest element size was set to the wavelength divided by eight, $\lambda/8$. The glue layer was set to have a mesh size of the wavelength of PMMA at 4 MHz divided by 100, $\lambda/100$, both for the spheres, the area outside the spheres and along the top and bottom boundary of the layer.

An integration function was set on the lower horizontal boundary, and was used to calculate the total current on this, while an average function was set on the boundary between the transducer and the load and used to calculate the average velocity. These two were used in COMSOL to calculate the impedance, which was defined as ‘Global Nodes’. The expressions are shown in Table 3.12, where I is the current over the lower boundary of the piezoelectric material, V0 is the voltage at the terminal, that is 1 V, and piezo_d is the depth of the piezoelectric material into the screen. This simulation ran a Frequency Study, which swiped over the frequencies from 0.1MHz to 20MHz. Around resonances, the simulations were done for 0.01MHz steps, while the rest was done with 0.05MHz steps.

Table 3.12: The expressions used for the global variable probes.

The current I is taken over the lower boundary of the piezo where a current density is set. V0 is the voltage at the terminal of the piezo, piezo_d is the depth of the structure. The average function is set over the top boundary of the structure, and is calculating the average velocity.

Variable name	Variable	Expression
Current	I	intop1(ej.Ty)*piezo_d
Impedance	Z	V0/I

3.6.3 Speed of Sound Model

The FEM model for simulating speed of sound using reflection from thin layers was developed by PhD student Per Kristian Bolstad [25]. The structure is shown in Figure 3.20, where the blue areas are water, with the rectangles furthest out being ‘Perfectly Matched Layer’, and the grey area is the glue layer containing spheres. The silver layer is in COMSOL made as a separate domain between two circles, shown in Figure 3.21. The whole sphere layer is set as a ‘Linear Elastic Material’, and vertical boundaries of the whole structure have Floquet periodic boundary conditions to allow oblique incidence. A background pressure is also set at the top water part. The model sweeps a plane wave at normal incidence over a range of frequencies and calculates the reflection coefficient at the top boundary, a little into the water layer, as the ratio of the scattered field to the incident field. A zoomed in image of the boundary is shown in Figure 3.21. The longitudinal speed of sound is found from the minima in the frequency spectrum for the reflection coefficient.

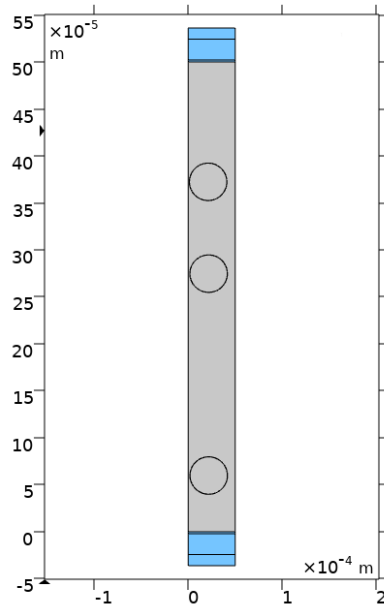


Figure 3.20: The structure used for speed of sound simulations.

The blue area is water, while the grey area is the sphere layer. The signal moves through the glue-sphere layer and is registered at the top boundary, a small distance into the water.

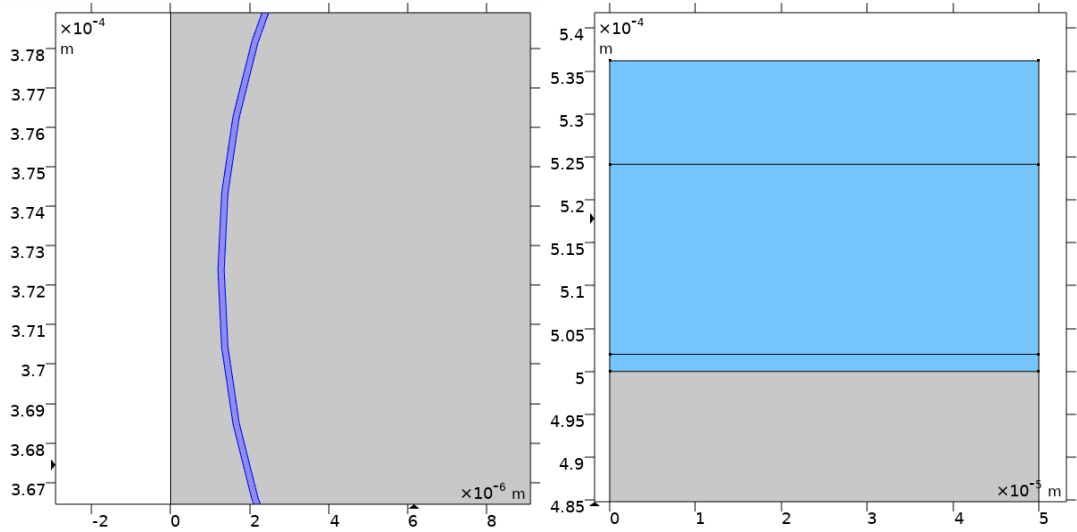


Figure 3.21: Zoomed in image of the sphere layer (in blue, left) and the thin water layer (right)

4 Results

4.1 Glass values

The measured speed of sound and calculated density and characteristic acoustic impedance for the glass samples are summarized in Table 4.1. Each sample was measured twice, except for sample S1 which was measured three times. All measurements generally showed the same, and the average value for each sample was used for calculation of the average value and standard deviation of the results. Figure 4.1 shows the output graph for sample L1 used to find the resonance frequencies, with the transmission peaks marked.

Table 4.1: Measured properties of the glass load used for the trial samples.

	Resonance frequency, f_0 [MHz]	Speed of sound, c [m/s]	Average volume [cm ³]	Average density, ρ [kg/m ³]	Impedance, Z [MRayl]
Sample L1	2.94	5792	0.9456	2458	14.2
Sample L2	2.94	5815	1.108	2492	14.5
	2.95	5835			14.5
Sample L3	2.94	5804	0.9949	2501	14.5
Sample L4	2.95	5812	0.8510	2437	14.2
Sample S1	2.64	5792	1.141	2448	14.2
Sample S2	2.64	5797	0.9992	2481	14.4
Average L	2.94 ± 0.01	5812 ± 16	---	2472 ± 30	14.4 ± 0.2
Average S	2.64 ± 0.0	5795 ± 4	---	2465 ± 23	14.3 ± 0.1

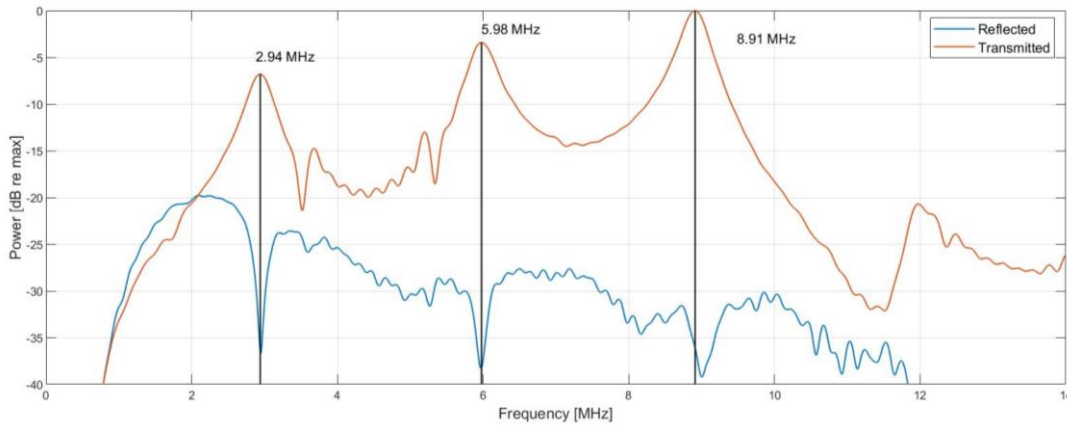


Figure 4.1: The power spectrum in decibel for sample L1.

The peaks in the transmitted shows where the glass had a resonance frequency.

4.2 Trial samples

4.2.1 Microscope images

Forming a monolayer was not a straightforward process, and some of the samples showed air bubbles within the glue layer or uneven distribution of the glue, both in the form of varying thickness and uneven edges. Figure 4.2 and Figure 4.3 are images through the glass load of trial sample 7 and trial sample 18, respectively, and show examples of this, with an air bubble under the PZT for sample 7 and the uneven edge of the glue layer for sample 18. Both images are with 25x magnification. The air-bubble shown in Figure 4.2 is one of the larger bubbles with a size of approximately 1 mm, while most others were somewhere between 100 μm and this.

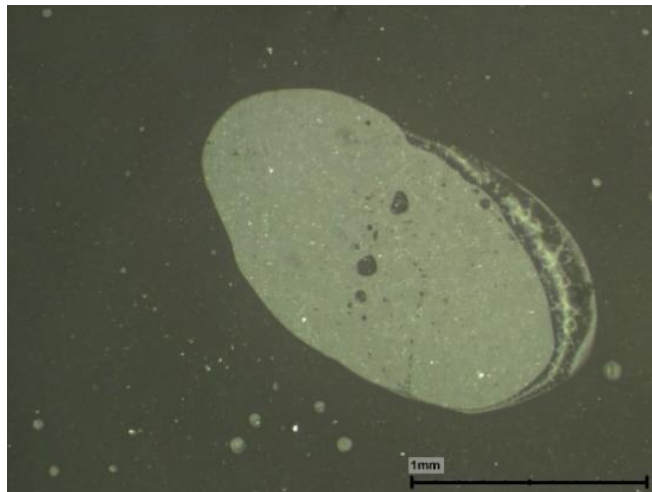


Figure 4.2: Air bubble in glue layer of trial sample 7. The scale bar has a length of 1 mm

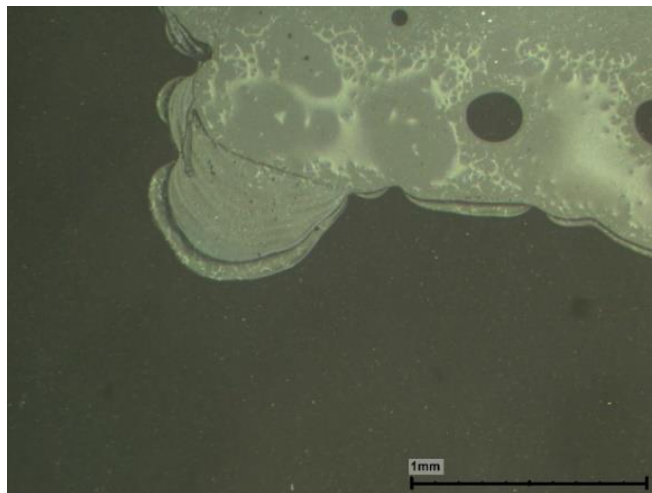


Figure 4.3: Uneven edge of the glue layer of trial sample 18. The scale bar has a length of 1 mm.

Figure 4.4 to Figure 4.6 are optical microscope images of some of the cross sections of the glue layer. Figure 4.4 shows an incomplete compression of the glue layer, resulting in a glue layer much thicker than the sphere diameter. This is seen in the image as the spheres, with a diameter of 20 μm , covering less than half the distance between the glass, on the top, and the PZT, on the bottom. Spheres are present all the distance between the glass load and the PZT, though it is not visible in this image. Figure 4.5 shows cross

section with good compression of the glue layer, where the total layer is only slightly thicker than the sphere diameter. Figure 4.6 shows the most common of the cross sections, where the total glue layer is somewhat thicker than the sphere diameter. This was seen for all samples, except sample 6, at some point in the cross section. Some, like sample 18, had other points where the compression was good. All the images have 250x magnification.

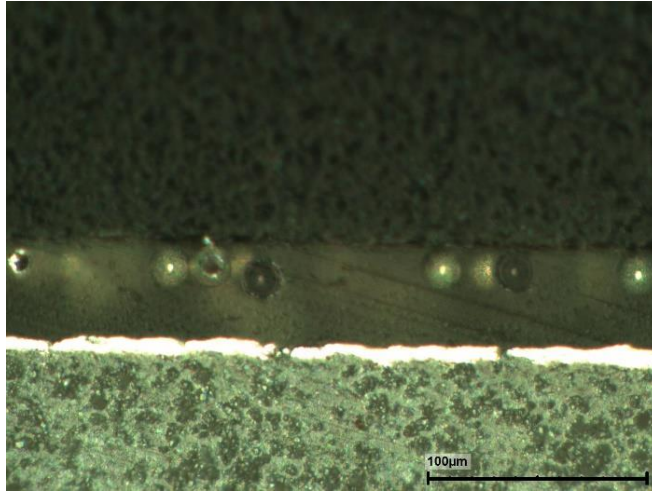


Figure 4.4: Incomplete compression of sphere layer between a PZT (bottom) and glass load (top), sample 6

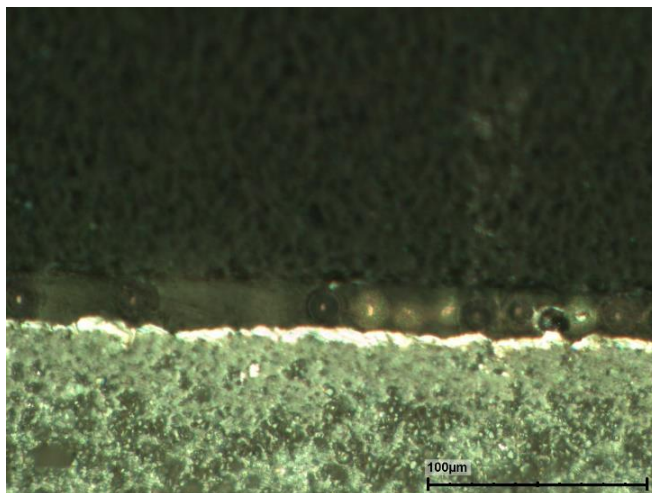


Figure 4.5: A good compression of glue-sphere layer only slightly bigger than the sphere diameter, sample 18

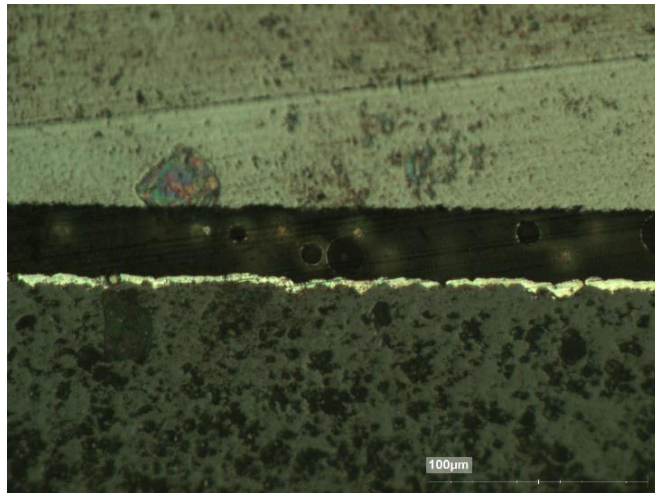


Figure 4.6: The most common cross section of the samples, with the compression being partially incomplete and spheres are being stacked on top of each other, sample 13

4.2.2 Results from fitting

A lot of trial was necessary to find the properties that gave the best fitting of the simulated impedance spectra. Table 4.2 shows the values used in Xtrans for fitting the simulated impedance spectra to the impedance spectra measured from the trial samples. The first column also shows all thicknesses measured with the optical microscope, and the thickness used in Xtrans is shown in the second column. The used values are measured in the center, and are either average of several values from the center or the one value from the center. Where it is not mentioned where the measurement is taken, the median value is used, as the average can be pulled up or down by extreme values.

Table 4.2: Measured thicknesses of the initial samples and the values used in xtrans

	Measured thickness [μm]		Thickness used in calculation [μm]	Characteristic Impedance, Z [MRayl]	Speed of sound, c [m/s]	Q
Trial 3	57.28		57.3	2.7	3200	15
Trial 4	41.73 (edge) 39.83 (edge) 31.49 (edge)	31.48 (edge) 29.61 (center) 27.70 (center)	28.7	2.8	3300	15
Trial 6	49.32 50.08	47.04	49.3	3.2	3300	15
Trial 7	58.80 (edge) 61.46 (edge) 50.84 (edge)	51.97 (edge) 54.25 (center)	54.3	2.8	2700	15
Trial 8	29.59 (edge) 32.63 (edge) 30.74 (edge)	33.76 (edge) 35.28 (center) 34.52 (center)	34.9	3.0	3000	15
Trial 13	31.87 (edge) 33.38 (edge)	33.38 (center) 33.76 (center)	33.8	2.8	2700	15
Trial 15	41.73 (edge) 39.08 (edge)	34.14 (center) 36.44 (center)	35.3	2.6	2700	15
Trial 16	29.59		29.6	2.8	2600	15
Trial 17	29.97 27.31	29.59	29.6	3.2	3200	15
Trial 18	29.21 28.07	25.80 23.14	26.9	3.2	3000	15

The average impedance in the fitted results of the 20 μm spheres trial samples is 3.0 ± 0.2 MRayl, and the average speed of sound with standard deviation in the same samples is 2975 ± 282 m/s. Figure 4.7 to Figure 4.16 shows the impedance spectra for the samples, with the measured impedance spectra in black and Xtrans adjusted impedance spectra in blue. The fitting of the curve is done around a small peak at lower frequency than the main large peak.

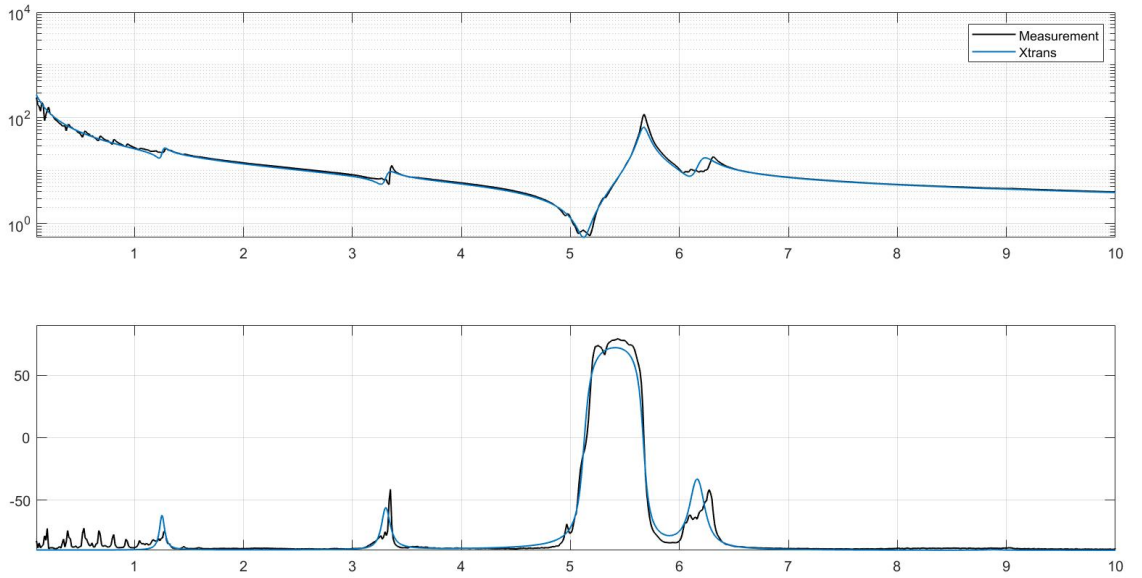


Figure 4.7: Impedance curve (top) and phase curve (bottom) for initial sample 3 consisting of a 5MHz PZT and glass load

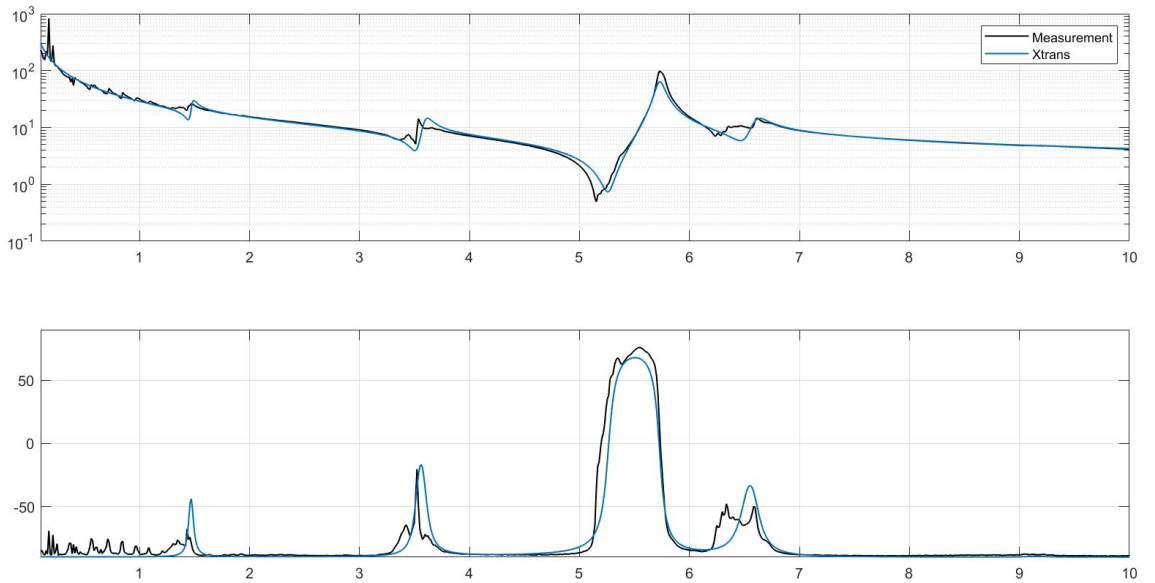


Figure 4.8: Impedance curve (top) and phase curve (bottom) for initial sample 4 consisting of a 5MHz PZT and glass load

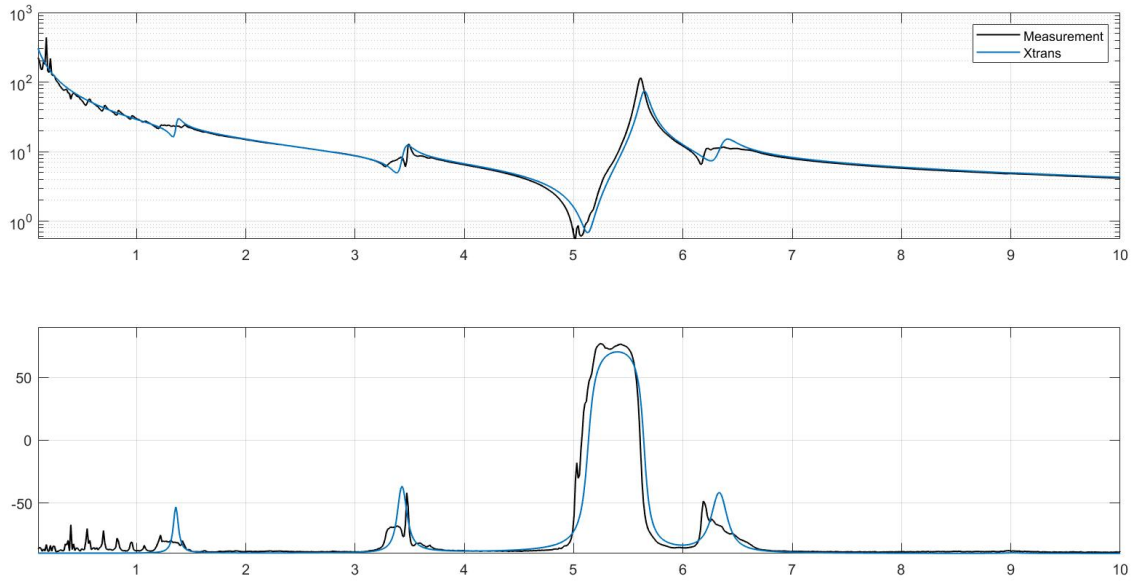


Figure 4.9: Impedance curve (top) and phase curve (bottom) for initial sample 6 consisting of a 5MHz PZT and glass load

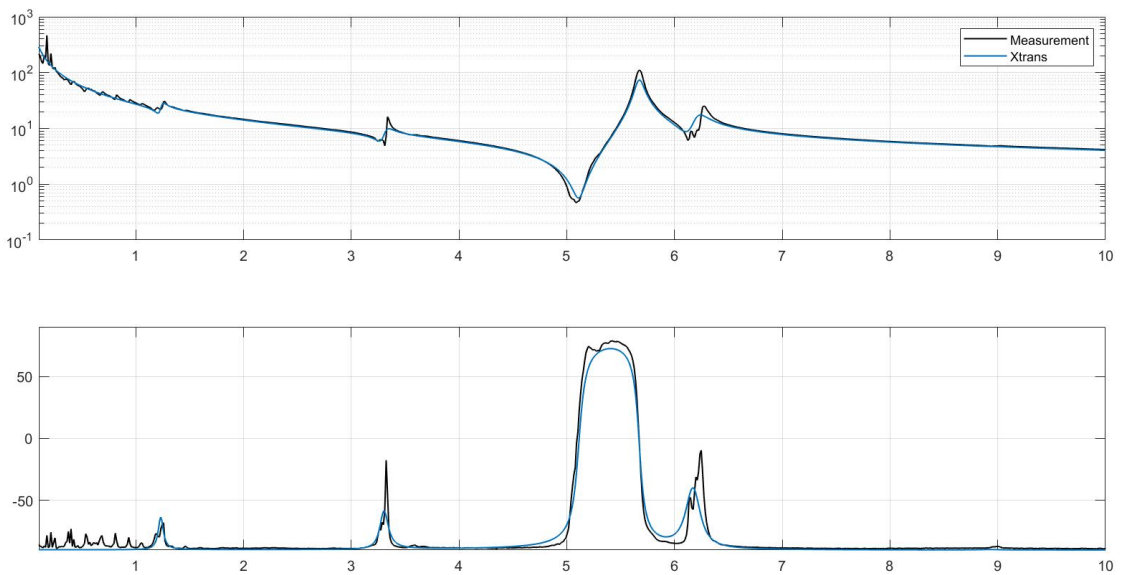


Figure 4.10: Impedance curve (top) and phase curve (bottom) for initial sample 7 consisting of a 5MHz PZT and glass load

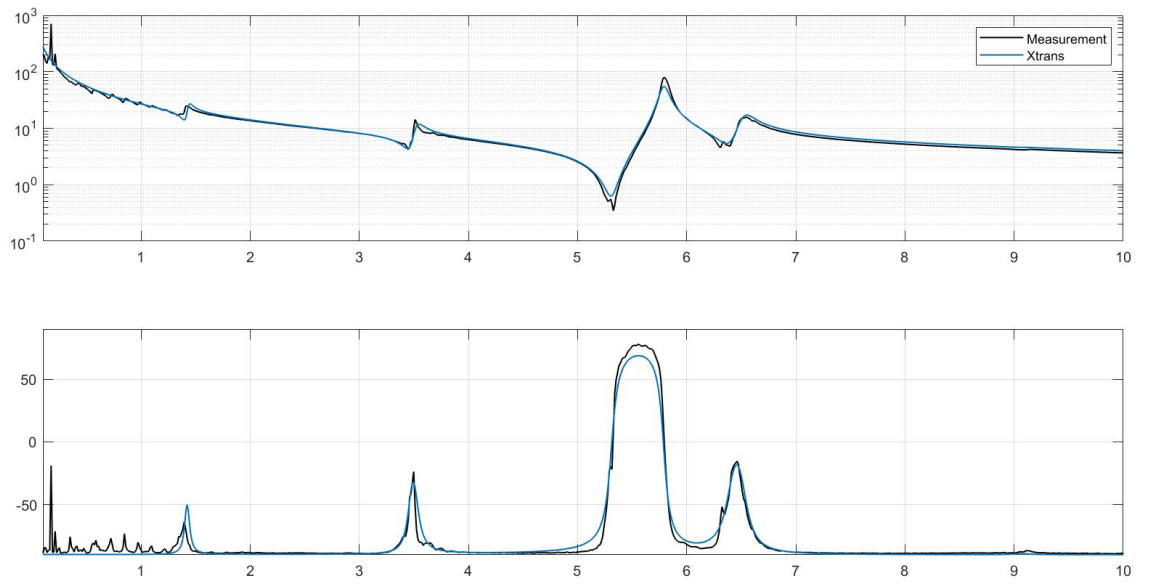


Figure 4.11: Impedance curve (top) and phase curve (bottom) for initial sample 8 consisting of a 5MHz PZT and glass load

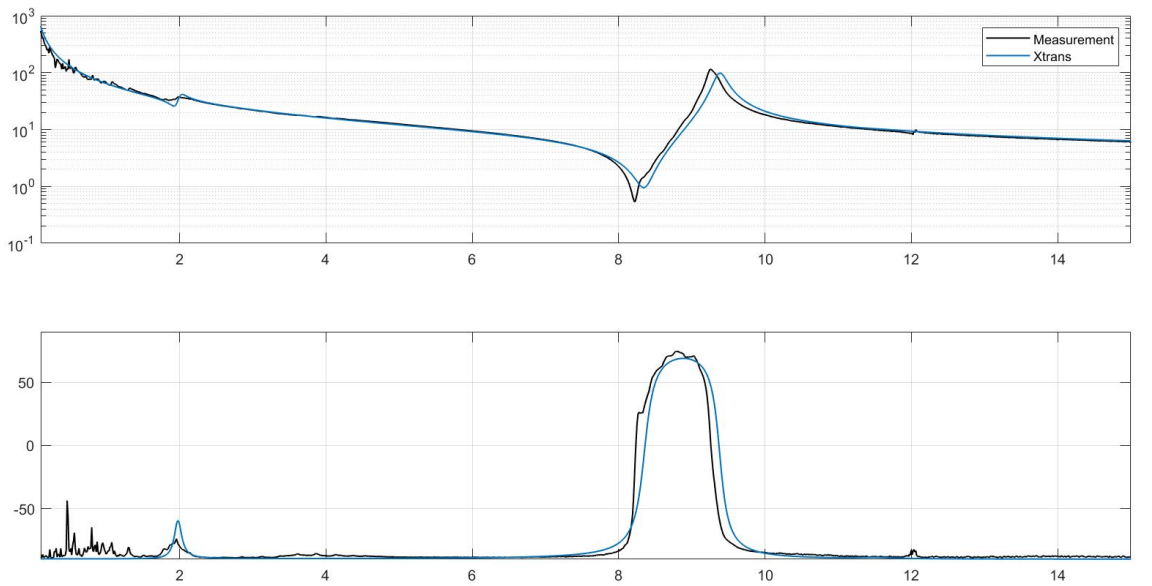


Figure 4.12: Impedance curve (top) and phase curve (bottom) for initial sample 13 consisting of an 8MHz PZT and WC load

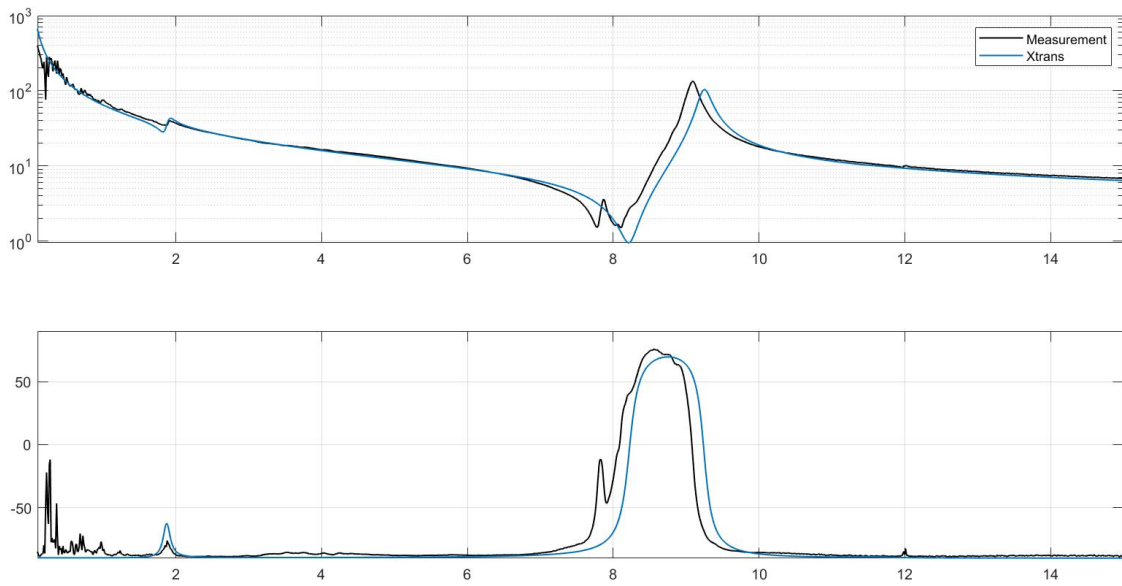


Figure 4.13: Impedance curve (top) and phase curve (bottom) for initial sample 15 consisting of an 8MHz PZT and WC load

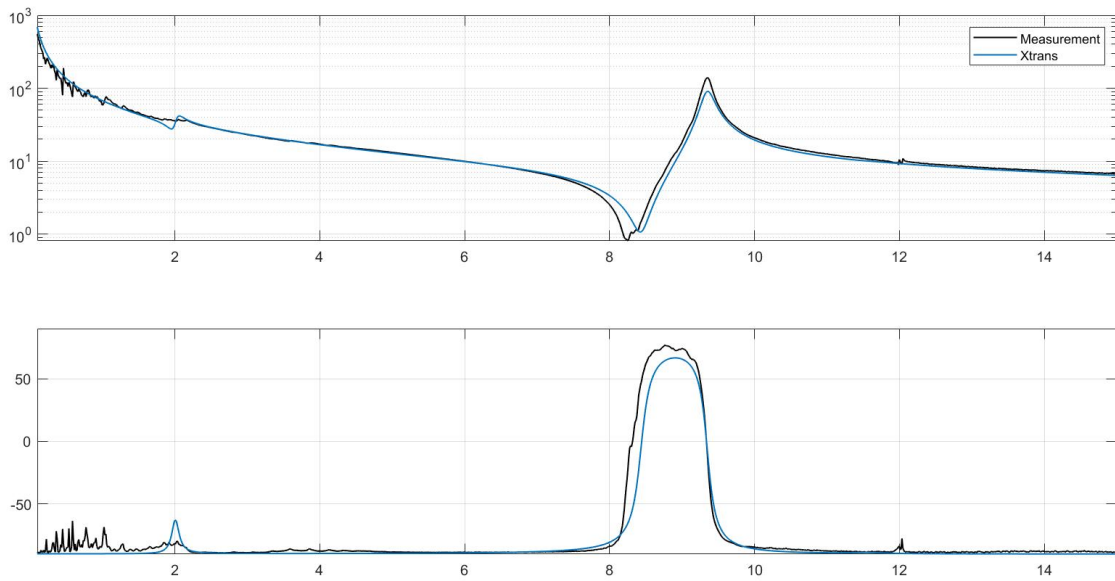


Figure 4.14: Impedance curve (top) and phase curve (bottom) for initial sample 16 consisting of an 8MHz PZT and WC load

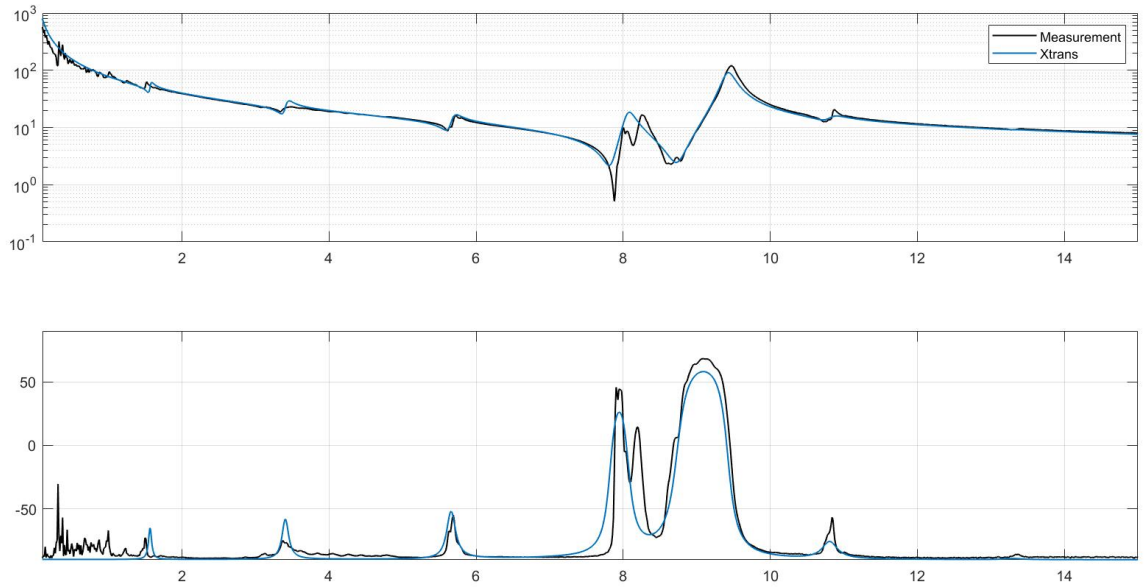


Figure 4.15: Impedance curve (top) and phase curve (bottom) for initial sample 17 consisting of an 8MHz PZT and glass load

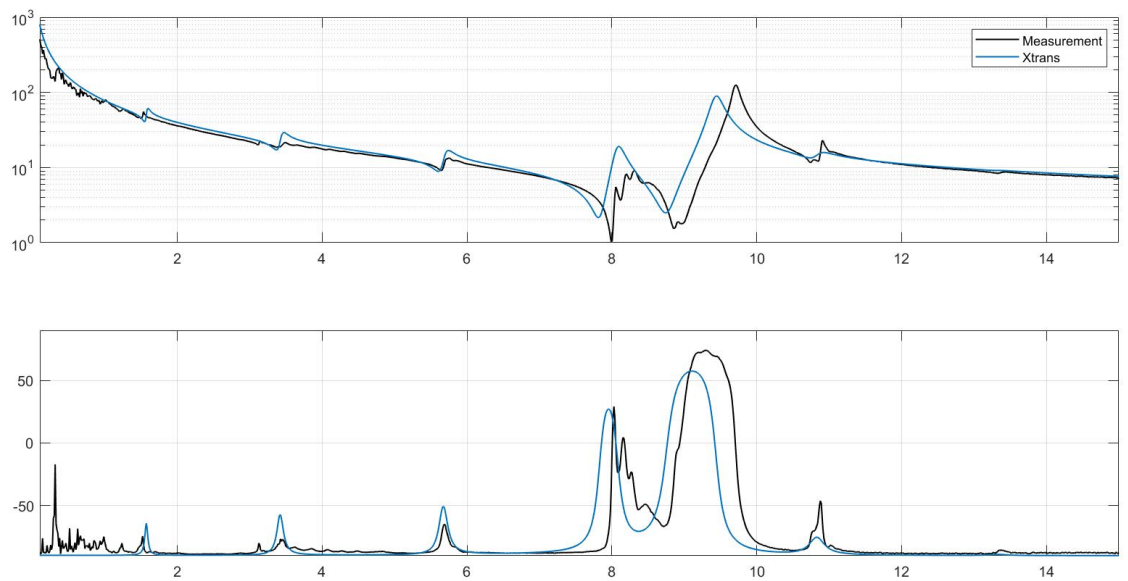


Figure 4.16: Impedance curve (top) and phase curve (bottom) for initial sample 18 consisting of an 8MHz PZT and glass load

Figure 4.17 shows the peak around which the fitting of the Xtrans impedance spectra was done for trial sample 7. All the peaks in the spectra stem from the glass or WC load and the PZT, while the addition of the sphere layer shifts the impedance spectra. This peak is the one which is the most sensitive to changes in the sphere layer, and therefore contains information about variations in the layer. The different lines in Figure 4.17 all represent different characteristic acoustic impedance values for the sphere layer, with a 0.2 MRayl jump between each line giving a visible shift between each line. The peak clearly matches a certain value for the characteristic acoustic impedance, with an estimated uncertainty of 0.1 MRayl.

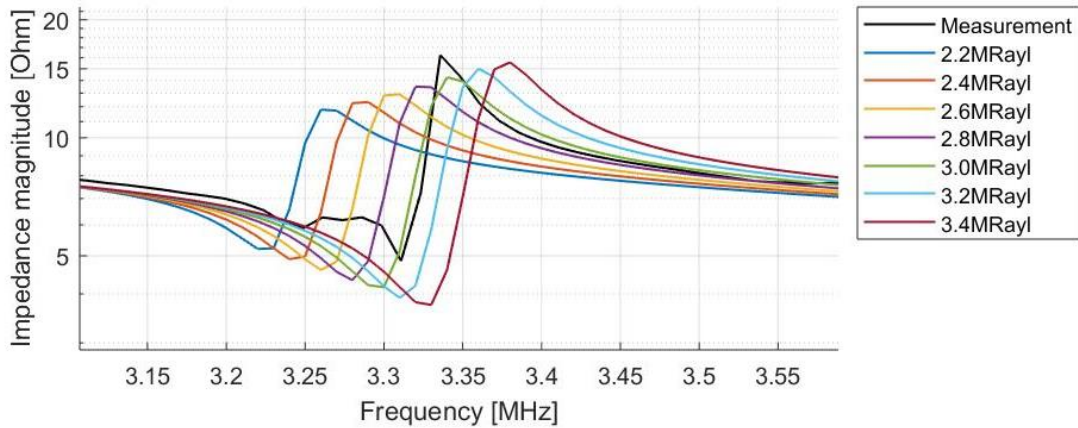


Figure 4.17: Graphs showing the effect of different impedance values for the sphere layer.
 The variation is larger at this smaller peak than it is at the main peak.

4.3 0-3 composite samples

4.3.1 Density of glue and MPS

The density was calculated for both the spheres, the pure Epo-tek 301-2 and the 0-3 composite samples. Figure 4.18 shows the comparison between the density of the samples and the ideal densities of the samples. The values are shown in Table 4.3, where column 3 shows the ideal values, found through calculations from the material properties or found in a reference, and column 4 shows the values calculated from the measurements of the samples. The ideal values for the particle densities are found using equation (2.12), while equation (2.14) was used to calculate the ideal density for the 0-3 composite samples. The ideal density for the Epo-tek 301-2 was found in [24]. Equation (2.14) rewritten for the volume fraction was used to calculate the volume fraction of air. The density of air was set to zero in these calculations, due to it being much smaller than the other densities.

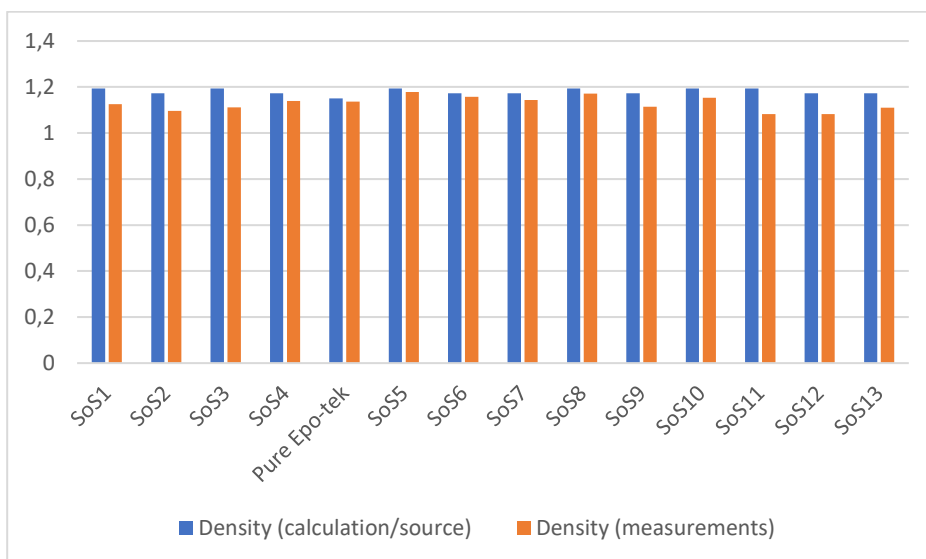


Figure 4.18: Comparison of the ideal density of the material (blue) and density calculated from the fabricated samples (red)

Table 4.3: Comparison of ideal/calculated density and measured density of the spheres and the samples.

	Sample	Density (calculated or from literature)	Density (measurements)	Volume fraction (air in samples)
Particle (20µm)	---	1.594 g/cm ³	---	---
Particle (40µm)	---	1.380 g/cm ³	---	---
Mixing test	SoS1	1.194 g/cm ³	1.125 ± 0.064 g/cm ³	5.8%
	SoS2	1.173 g/cm ³	1.113 ± 0.049 g/cm ³	5.1%
	SoS3	1.194 g/cm ³	1.112 ± 0.056 g/cm ³	6.9%
	SoS4	1.173 g/cm ³	1.144 ± 0.058 g/cm ³	2.5%
Epo-tek 301-2	Pure Epo-tek	1.150 g/cm ³	1.136 ± 0.008 g/cm ³	1.2%
Speed of sound samples	SoS5	1.194 g/cm ³	1.178 ± 0.026 g/cm ³	1.3%
	SoS6	1.173 g/cm ³	1.151 ± 0.026 g/cm ³	1.9%
	SoS7	1.173 g/cm ³	1.143 ± 0.028 g/cm ³	2.6%
	SoS8	1.194 g/cm ³	1.169 ± 0.023g/cm ³	2.1%
	SoS9	1.173 g/cm ³	1.113 ± 0.013g/cm ³	5.1%
	SoS10	1.194 g/cm ³	1.153 ± 0.022 g/cm ³	3.4%
	SoS11	1.194 g/cm ³	1.082 ± 0.044 g/cm ³	9.4%
	SoS12	1.173 g/cm ³	1.082 ± 0.020 g/cm ³	7.6%
	SoS13	1.173 g/cm ³	1.110 ± 0.020 g/cm ³	5.6%

4.3.2 Mixing trial

The first 0-3 composite samples displayed separation of the spheres and the glue by both sedimentation and floatation. The figures below show the cross section of the samples consisting of MPS and Epo-tek 301-2. Figure 4.19 shows the 40 µm sphere sample without Byk. This has created a sandwich sphere layer, with spheres both on the bottom and the top surface, though the top surface layer is not visible in this figure. Figure 4.20 shows the cross section of the 20 µm sphere sample with Byk, where the layer of spheres is only shown at the bottom.



Figure 4.19: The cross section of the test sample with 40 µm spheres without Byk, SoS2. Practically all of the spheres are gathered in the bottom of the sample due to sedimentation.



Figure 4.20: The cross section of the test sample 20 μm spheres with Byk, SoS3.

Most of the spheres are gathered at the bottom due to sedimentation, but the Byk has made some stay in the rest of the sample.

Figure 4.21 shows the underside of the test speed of sound samples with 20 μm spheres, SoS1 and SoS3, with 200x magnification. The underside of the samples with 40 μm spheres, SoS2 and SoS4, showed the same tendency as the 20 μm sphere samples.

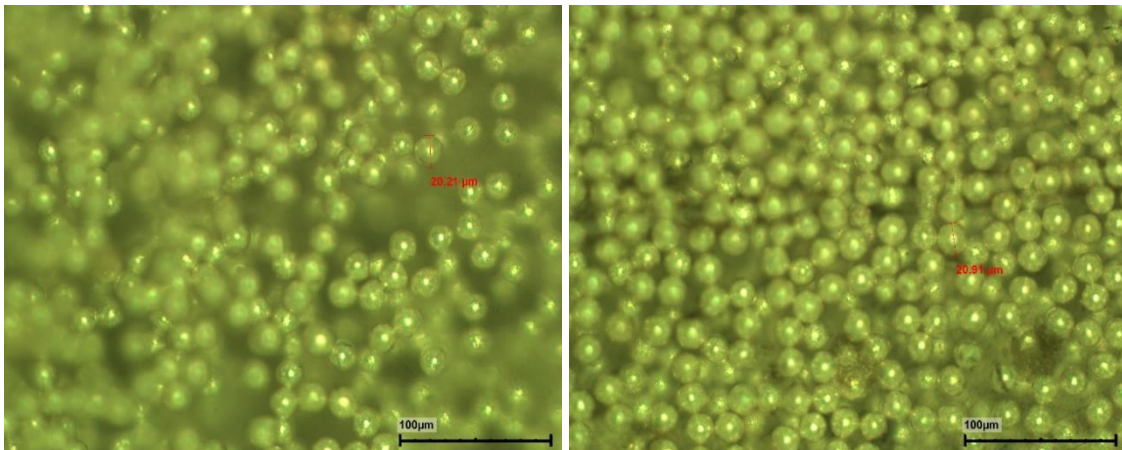


Figure 4.21: The 20 μm sphere samples with Byk, SoS3, (left) and without Byk, SoS1, (right), seen from the underside, 200x magnification

Figure 4.22 shows a microscope image of the thin layer that could be seen on the top of the speed of sound samples without Byk. This layer could be seen both for the sample with 20 μm spheres, SoS3, and for the sample with 40 μm spheres, SoS4.

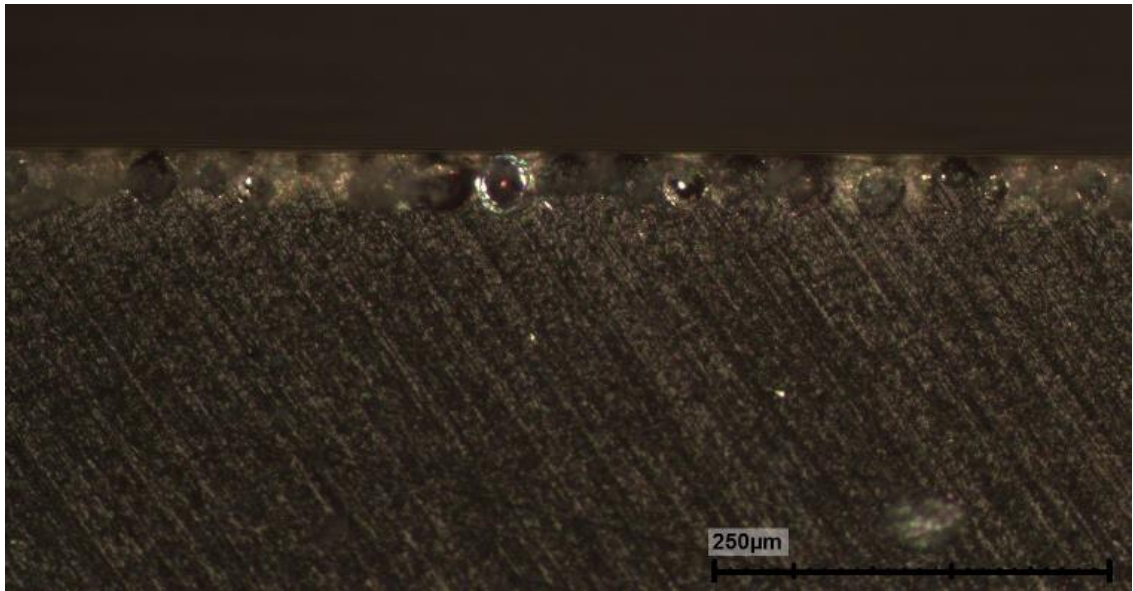


Figure 4.22: Monolayer of spheres on top of the 40 μm speed of sound sample without Byk, SoS4, 100x magnification

4.3.3 Speed of sound samples

Several speed of sound samples were made, with some having even distribution and could be used for measurements, while others experienced sedimentation. Most of the samples showed sedimentation after 30 minutes in the oven, and a new sedimentation after around the 45 minutes when a mixing had been done at 30 minutes. A few showed signs of sedimentation later, with the time of curing needed to avoid sedimentation seeming random. 8 samples were made that either showed sedimentation or uneven distribution of spheres in the finished sample. These samples were discarded, and only the samples showing even distribution of spheres were measured. Table 4.4 shows the calculated and measured values of the 0-3 composite speed of sound samples where the spheres were evenly mixed throughout the sample. Figures 4.23 and 4.24 are bar charts comparing the average values for the measurements in Table 4.4. The average values are calculated from the average values for each sample. Figure 4.23 compares the speed of sound, while Figure 4.24 compares the impedance values. No results are shown for sample SoS7 as this sample was not properly mixed.

Table 4.4: Measured speed of sound and characteristic acoustic impedance for the 0-3 composite speed of sound samples.

	Speed of sound, c [m/s]		Impedance, measured density [MRayl]		Impedance, ideal density [MRayl]	
	(1)	(2)	(1)	(2)	(1)	(2)
SoS5 (20μm)	2554	2551	3.01	3.01	3.05	3.05
	2554	2548	3.01	3.00	3.05	3.04
	2550	2548	3.01	3.00	3.04	3.04
SoS6 (40μm)	2493	2483	2.88	2.87	2.92	2.91
	2501	2483	2.89	2.87	2.93	2.91
SoS8 (20μm)	2632	2632	3.08	3.08	3.14	3.14
	2630	2633	3.08	3.09	3.14	3.14
	2632	2632	3.08	3.08	3.14	3.14
	2638	2633	3.09	3.08	3.15	3.14
SoS9 (40μm) (There is a lot of noise on the three last measurements of (1))	2431	2441	2.71	2.72	2.85	2.86
	2430	2439	2.71	2.72	2.85	2.86
	2443	2454	2.72	2.73	2.87	2.88
	2064	2457	2.30	2.73	2.42	2.88
	1168	2459	1.30	2.74	1.37	2.88
SoS10 (20μm)	2533	2536	2.92	2.92	3.02	3.03
	2533	2536	2.92	2.92	3.02	3.03
	2534	2537	2.92	2.93	3.03	3.03
SoS11 (20μm)	2624	2624	2.84	2.84	3.13	3.13
	2623	2624	2.84	2.84	3.13	3.13
	2624	2624	2.84	2.84	3.13	3.13
SoS12 (40μm)	2402	2416	2.60	2.61	2.82	2.83
	2398	2417	2.59	2.62	2.81	2.84
	2402	2418	2.60	2.62	2.82	2.84
SoS13 (40μm)	2452	2460	2.72	2.73	2.88	2.89
	2453	2459	2.72	2.73	2.88	2.88
	2455	2459	2.73	2.73	2.88	2.88
Average (20μm)	2586±50	2586±50	2.96±0.10	2.96±0.10	3.09±0.06	3.09±0.06
Average (40μm)	2446±40	2452±27	2.73±0.12	2.74±0.10	2.87±0.05	2.87±0.03

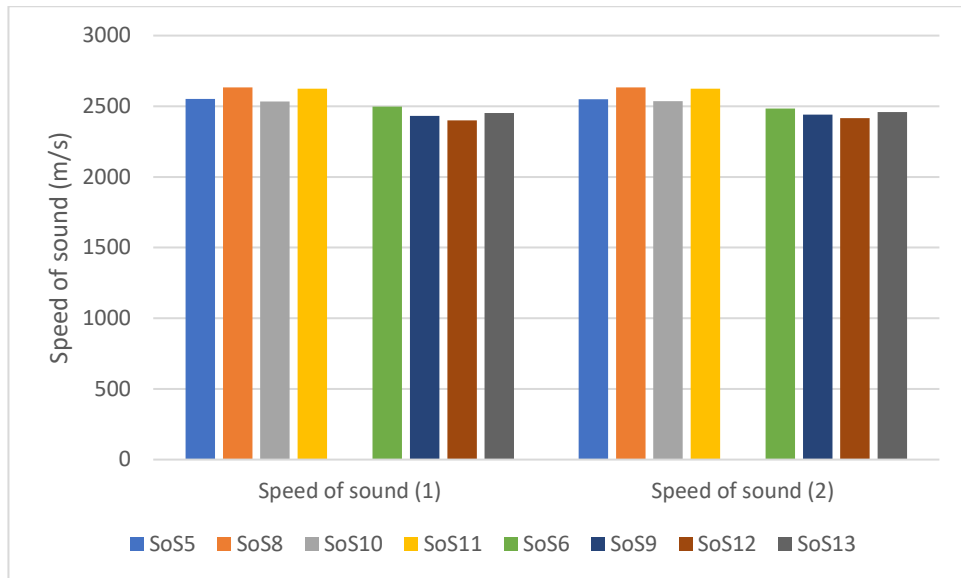


Figure 4.23: Bar chart comparing the average speed of sound of the different SoS samples. SoS5, SoS8, SoS10 and SoS11 are samples using 20 μm spheres, while SoS6, SoS9, SoS12 and SoS13 are samples using 40 μm spheres.

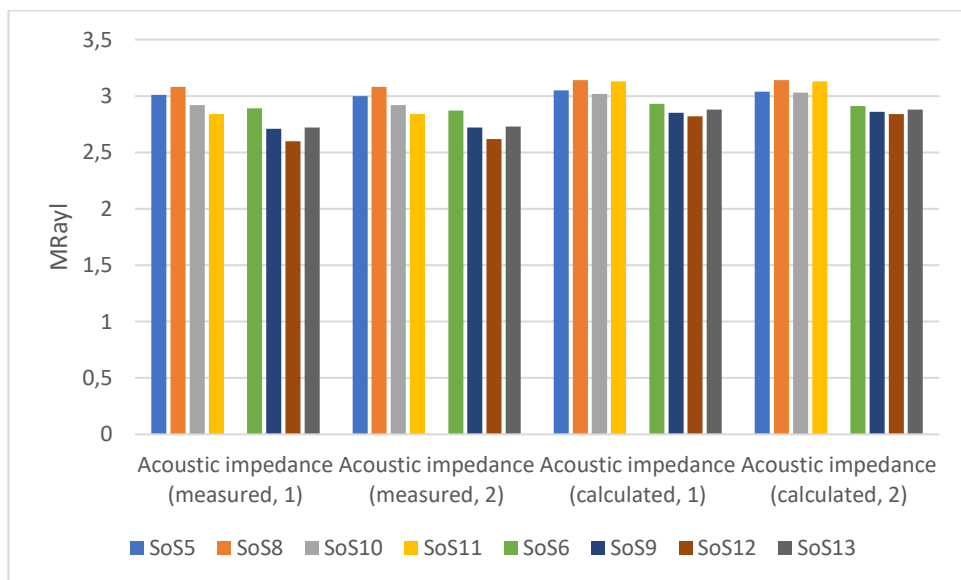


Figure 4.24: Bar chart comparing the average acoustic impedance of the different SoS samples. Measured means all the values used to calculate the acoustic impedance were from measurements on the samples, while the calculated bars use the ideally calculated densities. SoS5, SoS8, SoS10 and SoS11 are samples using 20 μm spheres, while SoS6, SoS9, SoS12 and SoS13 are samples using 40 μm spheres.

Figure 4.25 shows the cross section of 0-3 composite speed of sound samples with even distribution of spheres, with 20 μm sample being on top and 40 μm sample being on the bottom. Figure 4.26 and Figure 4.27 shows microscope images of the cross sections of some of the speed of sound samples. Figure 4.26 shows the cross section of SoS5 where no air bubbles are visible, while Figure 4.27 shows the cross section for SoS10 with clearly visible air bubbles. Almost all the speed of sound samples showed air bubbles in the microscope, with the exception being SoS5 and SoS8.



Figure 4.25: Cross section of proper speed of sound samples, with $20\mu\text{m}$ speed of sound sample on top and $40\mu\text{m}$ speed of sound sample on bottom.

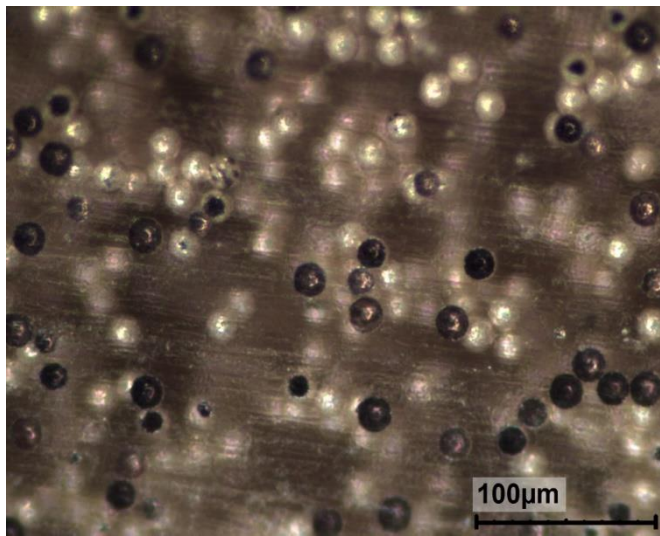


Figure 4.26: Cross section of SoS5, 200x magnification, indicating no air bubbles are present

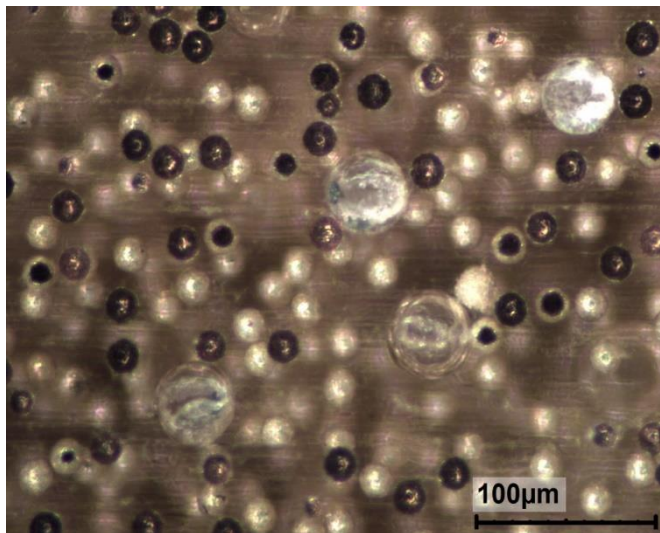


Figure 4.27: Cross section of SoS10, 200x magnification.

The smaller darker circles are the spheres, while the larger, lighter circles are air bubbles in the sample.

4.3.4 Speed of sound simulations

One method for determining the speed of sound through simulation is to simulate the reflection coefficient to find the resonance frequency. Table 4.5 shows the speed of sound calculated from simulations of the

reflection coefficient. Most of the samples are monolayers, with the exception being sample 7, sample 8 and sample 9, which were thicker samples. A comparison of the average simulation values, the measured values, and values from references are shown in Figure 4.28. A graph showing the output reflection coefficient from the simulation is shown in Figure 4.29, with the minimum value being the resonance frequency.

Table 4.5: The speed of sounds calculated from simulations of the reflection coefficient

Sample nr.	Volume fraction	c [m/s] (20 μ m)	c [m/s] (40 μ m)		Average c [m/s] (20 μ m)	Average c [m/s] (40 μ m)
Sample 1	0%	2432	2432		2432 \pm 0	2432 \pm 0
Sample 2	10%	2368	2370		2373 \pm 8	2372 \pm 4
Sample 3	10%	2376	2370			
Sample 4	10%	2364	2380			
Sample 5	10%	2384	2370			
Sample 6	10%	2372	2370			
Sample 7	10%	2372	2380		2373 \pm 6	2383 \pm 6
Sample 8	10%	2368	2390			
Sample 9	10%	2380	2380			
Sample 10	20%	2348	2340		2339 \pm 8	2347 \pm 6
Sample 11	20%	2336	2350			
Sample 12	20%	2332	2350			
Sample 13	30%	2296	2300		2291 \pm 6	2303 \pm 6
Sample 14	30%	2284	2310			
Sample 15	30%	2292	2300			

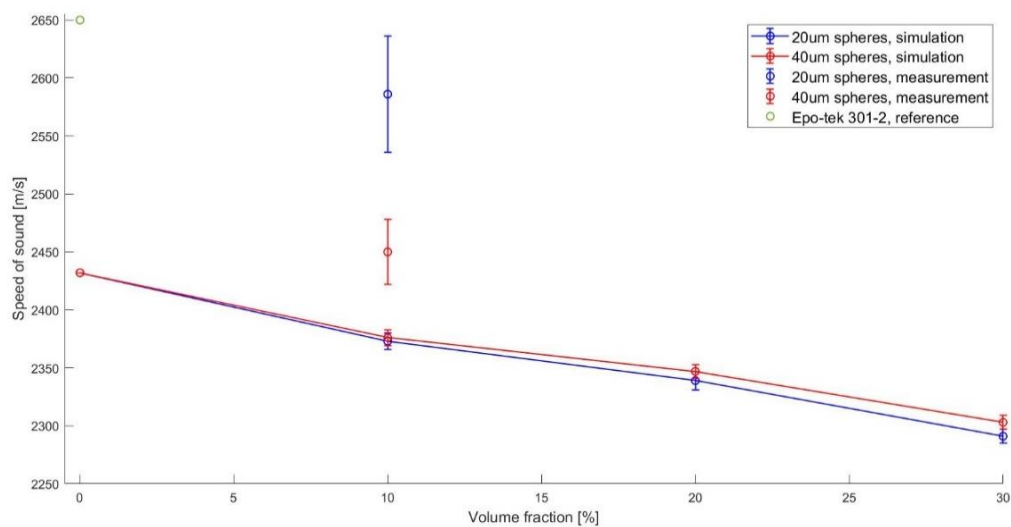


Figure 4.28: Graph with the speed of sound found from simulations.

The lone circle is the speed of sound found for Epo-tek 301-2 in [24], while the circles with errorbars are the average values measured from the speed of sound samples

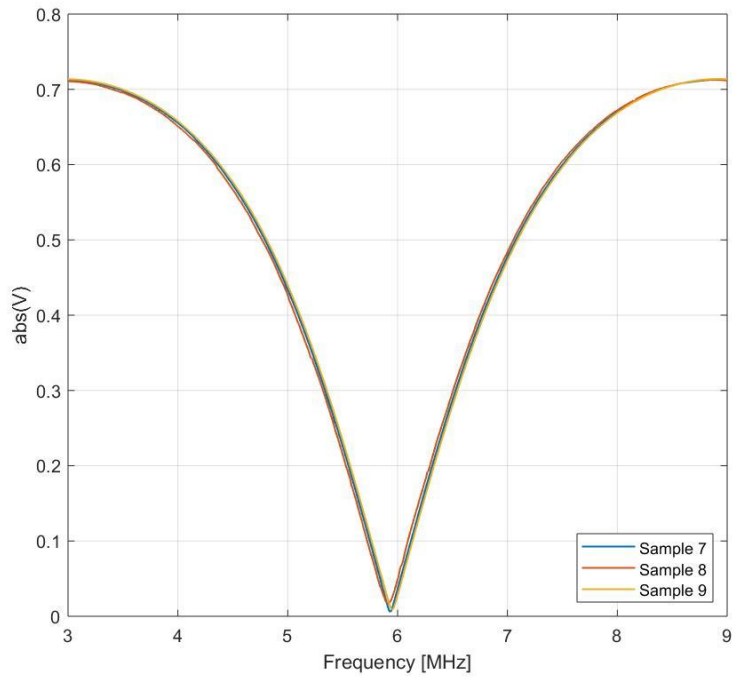


Figure 4.29: The reflection coefficient spectrum for the thick 20 μm , 10% volume sphere simulations.

4.4 Modeling

4.4.1 Thermal conductivity

The temperature distribution and thermal conductivity values varied depending on the method and structure that was used. Figure 4.30 shows the heat distribution in the sphere layer for the thermal conductivity model with all spheres having the same size. Figure 4.31 shows the same for the model where both the sphere size and the distribution is random, while Figure 4.32 show it for the structure where the spheres have random size, but same y-coordinate. The core temperature indicates how close to the lower edge the sphere is.

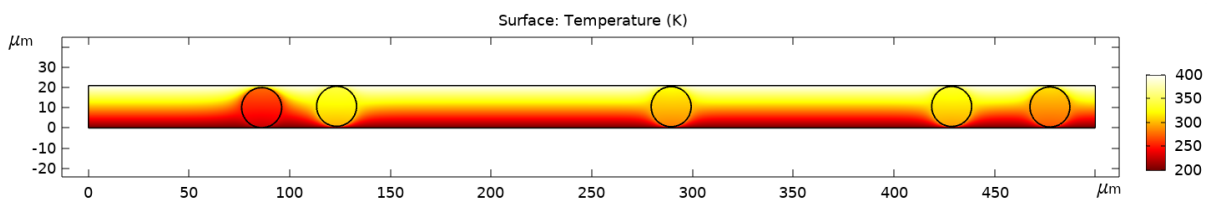


Figure 4.30: Temperature distribution in structure of same radius spheres

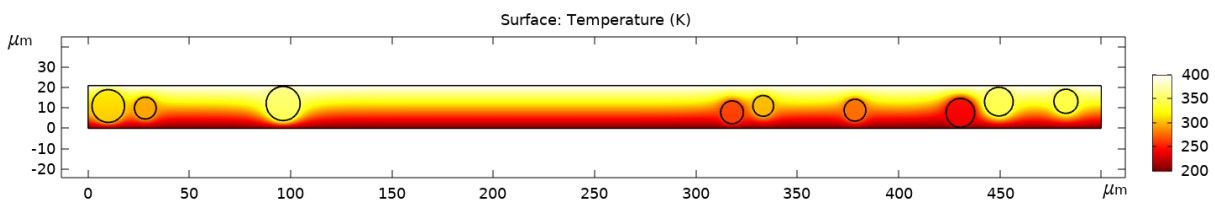


Figure 4.31: Temperature distribution in geometry with random sphere radius and random distribution

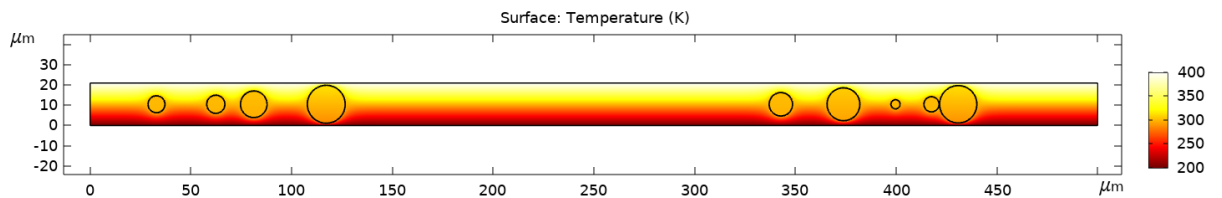


Figure 4.32: Temperature distribution in geometry with random sphere size, set y-coordinate of the circle center and random x-coordinate

This is how it looked for all simulations, with the spheres closer to the top edge of 400K having a higher core temperature than the ones closer to the lower edge of 200K, and the core having small or no temperature variations. Figure 4.33 and Figure 4.34 shows the temperature distribution for the comparison method, where the PMMA layer was used as a reference to calculate the thermal conductivity.

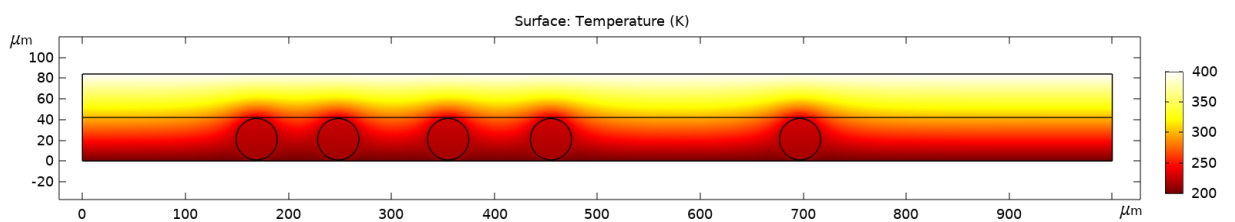


Figure 4.33: Temperature distribution for the 40 μm same size geometry where the sphere layer is compared to PMMA

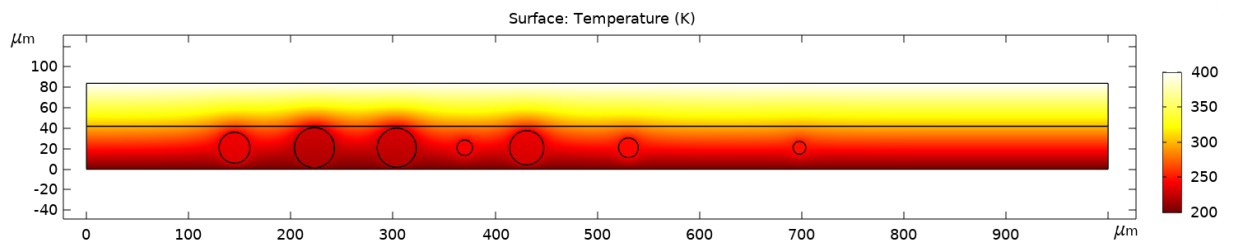


Figure 4.34: Temperature distribution for the 40 μm same place, random size geometry where the sphere layer is compared to PMMA

Table 4.6 shows the thermal conductivities for 20 μm sphere samples for different structures, under the assumption that the temperature distribution was linear. The results are represented graphically in Figure 4.35. Samples nr. 1 to nr. 10 are of geometry type nr. 1, Figure 3.13, while samples nr. 11 to nr. 15 are of geometry type nr. 2, Figure 3.14, and samples nr. 16 to nr. 20 are of geometry type nr. 3, Figure 3.15. For the 3D models the thickness varies, with sample nr. 1 to sample nr. 10 being 23 μm thick, while sample nr. 11 to sample nr. 20 were 20.5 μm thick.

Table 4.6: Comparison of methods for finding the thermal conductivity of a monolayer for 20 μm .
 The samples have the same structure in PMMA comparison and heat flux, while the 3D is different.

	PMMA comparison [W/(m*K)]	Heat flux [W/(m*K)]	3D model [W/(m*K)]
Nr. 1	0.245	0.266	0.297
Nr. 2	0.248	0.268	0.296
Nr. 3	0.255	0.274	0.295
Nr. 4	0.245	0.256	0.298
Nr. 5	0.258	0.291	0.299
Nr. 6	0.273	0.302	0.294
Nr. 7	0.266	0.296	0.294
Nr. 8	0.284	0.301	0.297
Nr. 9	0.264	0.283	0.297
Nr. 10	0.271	0.283	0.296
Nr. 11	0.294	0.426	0.325
Nr. 12	0.297	0.430	0.324
Nr. 13	0.294	0.432	0.324
Nr. 14	0.296	0.432	0.326
Nr. 15	0.301	0.437	0.325
Nr. 16	0.240	0.255	0.326
Nr. 17	0.248	0.263	0.326
Nr. 18	0.251	0.287	0.325
Nr. 19	0.249	0.278	0.328
Nr. 20	0.246	0.281	0.325

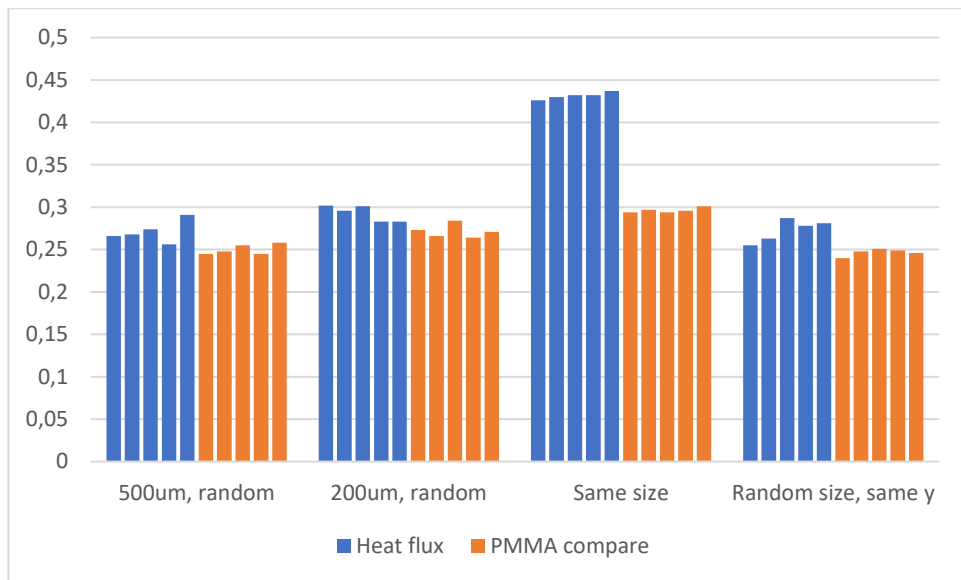


Figure 4.35: Graph showing the variations of the thermal conductivities for the 20 µm 2D simulations. The graphs are arranged after the samples of the same geometry type. Most of the results here are almost the same, with the exception being the values obtained from the same size structure with calculations from the obtained heat flux.

Table 4.7 and Figure 4.36 show the same as Table 4.6 and Figure 4.35, only for the 40 µm sphere. In this case samples nr. 21 to nr. 25 are of geometry type nr. 3, Figure 3.15, while samples nr. 26 to nr. 30 are of geometry type nr. 2, Figure 3.14. For both the 40 µm and 20 µm sphere structures, the heat flux calculation gave approximately 30% higher value than the PMMA comparison for the same size structures, while the results were almost the same for all the other structures.

Table 4.7: Comparison of methods for finding the thermal conductivity of a monolayer for 40µm. The samples have the same structure in PMMA comparison and heat flux, while the 3D is different.

	PMMA comparison [W/(m*K)]	Heat flux [W/(m*K)]	3D model [W/(m*K)]
Nr. 21	0.243	0.259	0.298
Nr. 22	0.245	0.267	0.294
Nr. 23	0.244	0.282	0.296
Nr. 24	0.245	0.260	0.299
Nr. 25	0.242	0.259	0.298
Nr. 26	0.283	0.390	0.318
Nr. 27	0.280	0.390	0.318
Nr. 28	0.284	0.390	0.320
Nr. 29	0.272	0.389	0.319
Nr. 30	0.280	0.390	0.323

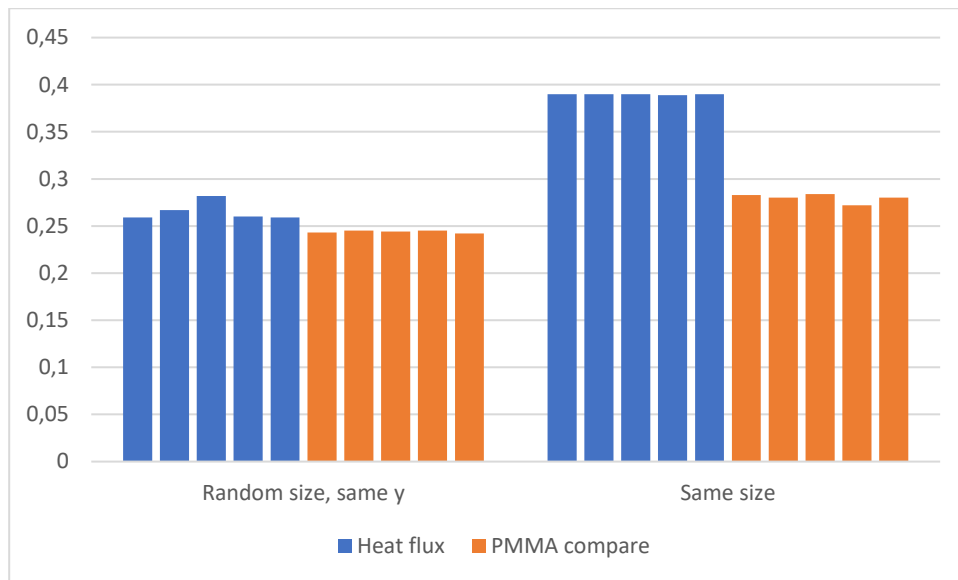


Figure 4.36: Graph showing the variations of the thermal conductivities for the 40µm 2D simulations. The graphs are arranged after the samples of the same geometry

Figure 4.37 shows a comparison of the thermal conductivities from the 3D models. The samples where the spheres fill the entire layer thickness (20.5 µm and 40.5 µm) gave approximately 10% higher thermal conductivity value than the layers with thickness larger than the spheres (23 µm and 44 µm).

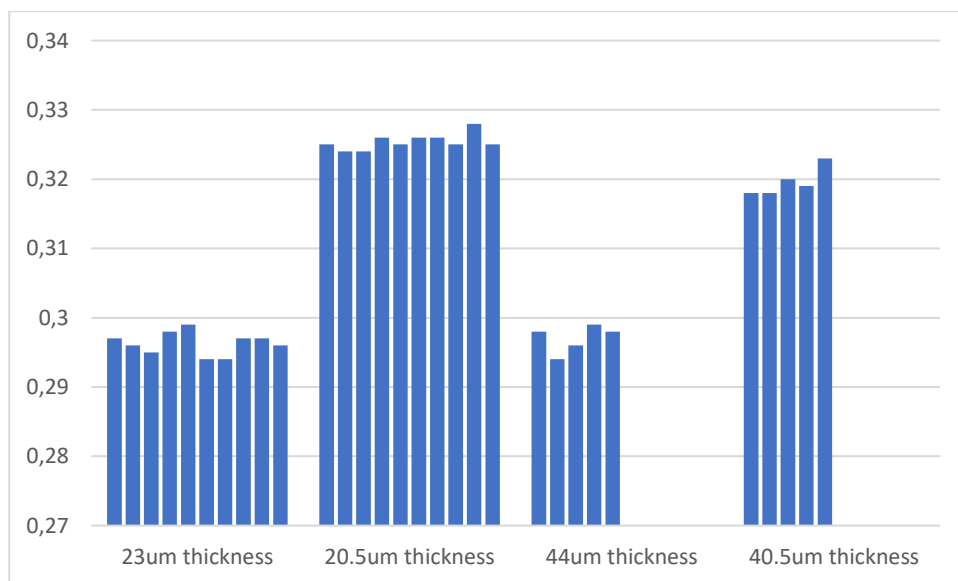


Figure 4.37: Graph showing the variations of the thermal conductivities for the 3D simulations. The graphs are arranged after the samples of the same geometry. The reduced distance with PMMA above and below the sample shows increased thermal conductivity.

The average values for the different structures with the standard deviation is summarized in Table 4.8.

Table 4.8: Overview of the average thermal conductivity and standard deviation for the different geometries.

	Sphere size	Variation	Heat flux [W/(m*K)]	PMMA comparison [W/(m*K)]
Geometry type 1	20 μm	500 μm wide	0.271 ± 0.013	0.250 ± 0.006
		200 μm wide	0.293 ± 0.009	0.272 ± 0.008
Geometry type 2	20 μm	---	0.431 ± 0.004	0.296 ± 0.003
	40 μm	---	0.390 ± 0.000	0.280 ± 0.005
Geometry type 3	20 μm	---	0.273 ± 0.013	0.247 ± 0.004
	40 μm	---	0.265 ± 0.010	0.244 ± 0.001
3D	20 μm	23 μm thickness	---	0.296 ± 0.002
		20.5 μm thickness	---	0.325 ± 0.001
	40 μm	44 μm thickness	---	0.297 ± 0.002
		40.5 μm thickness	---	0.320 ± 0.002

4.5 Silicon samples

The thickness of the sphere layers for the samples consisting of silicon and glass were measured both mechanically and with the optical microscope. The thicknesses found with the optical microscope are shown in Table 4.9, with all thicknesses given in μm . Figure 4.38 and Figure 4.39 shows the mechanically calculated thicknesses of the same samples, also in μm , at different points. These are calculated from the thicknesses measured before and after fabrication, and correspond well with the measurements from the optical microscope.

Table 4.9: Thickness of the sphere layer of the silicon samples measured with the optical microscope. All thicknesses are given in μm .

Sample	Sphere type	Left		Middle		Right	
S4	20 μm	21.64	23.15	22.39	23.15	23.52	22.01
S5	20 μm	40.23	40.64	41.37	39.08	36.82	38.38
S6	20 μm	31.13	33.01	28.46	27.73	26.98	25.44
S7	40 μm	40.22	40.21	41.73	40.97	40.21	40.59
S8	40 μm	40.60	40.23	41.36	40.21	40.21	40.64
S9	40 μm	40.21	40.22	40.21	40.59	40.98	41.38
L1	20 μm	21.59	22.54	22.06	22.07	24.88	21.66
L3	40 μm	40.03	40.39	40.85	40.37	40.50	40.88
L7	40 μm	40.37	40.38	40.08	40.41	40.39	40.38
L8	20 μm	21.59	22.54	24.88	22.54	22.06	22.54
L11	20 μm	20.18	20.66	20.19	20.66	20.18	20.65

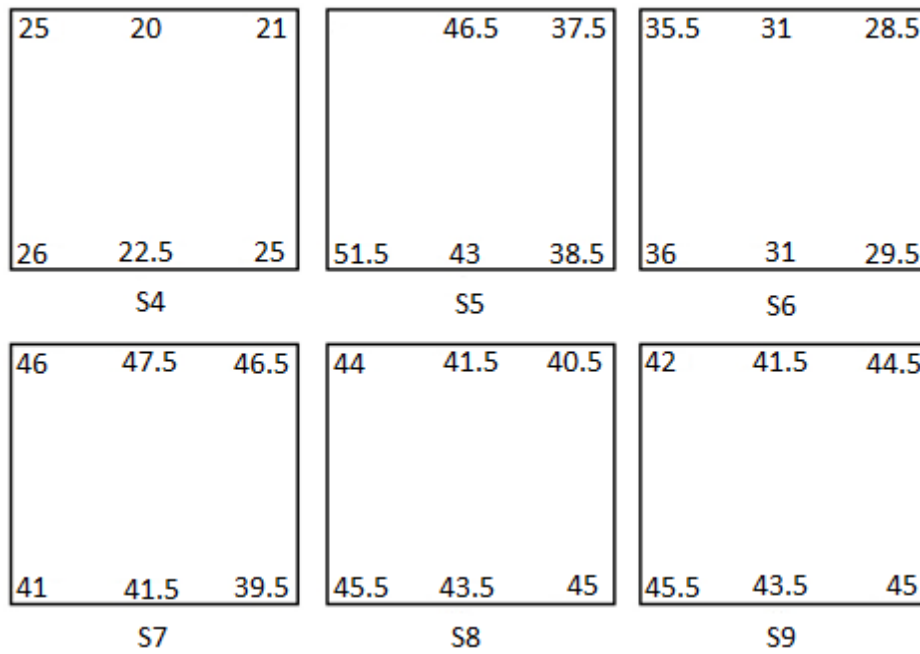


Figure 4.38: Thickness distribution of the silicon samples made with glass from the small microscope coverslips calculated from mechanical measurements. All thicknesses are given in μm .

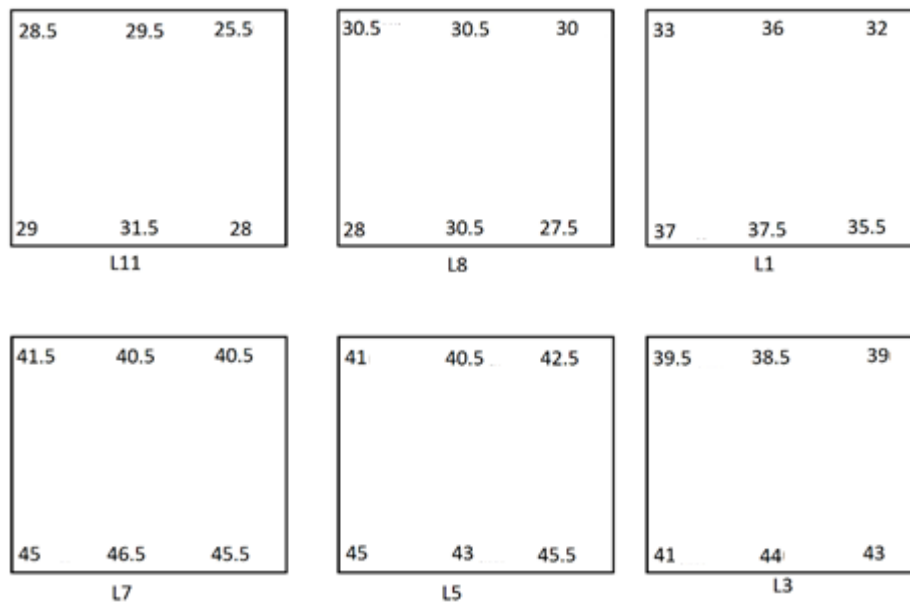


Figure 4.39: Thickness distribution of the silicon samples made with glass from the large coverslips calculated from mechanical measurements. All thicknesses are given in μm .

Figure 4.40 to Figure 4.43 shows microscope images of the undersides of the samples through the glass. Images for all three 20 μm S samples are shown due to the difference between them, while only one image showing the most common spread of the spheres is added for the 40 μm samples.

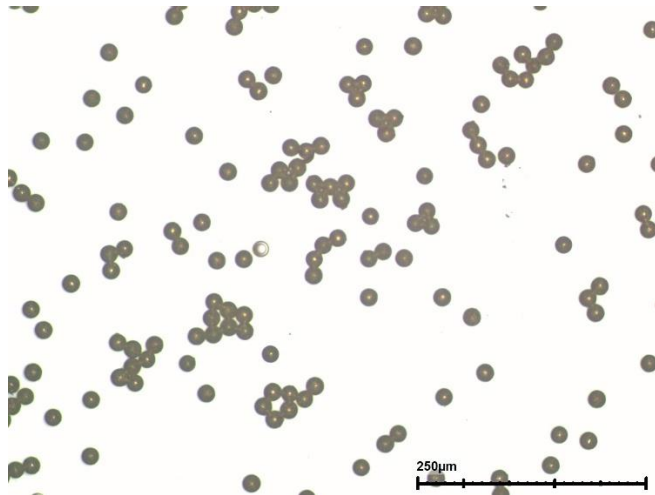


Figure 4.40: Image through the glass of the underside of silicon sample S4, 100x magnification

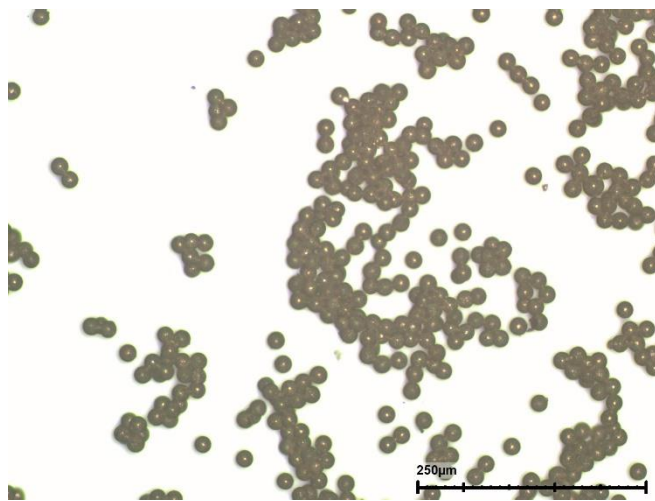


Figure 4.41: Image through the glass of the underside of silicon sample S5, 100x magnification

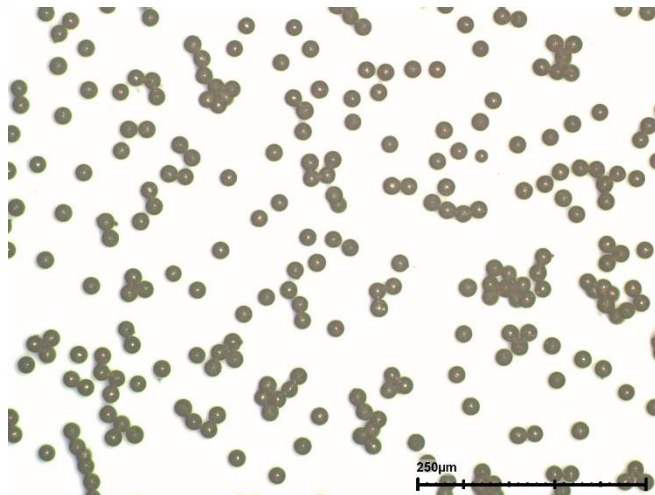


Figure 4.42: Image through the glass of the underside of silicon sample S6, 100x magnification

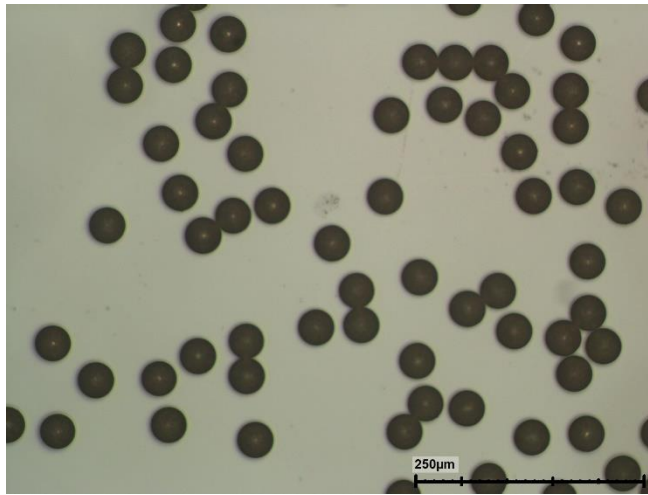


Figure 4.43: Image through the glass of the underside of silicon sample S8, 100x magnification.

This was the most common sight of the underside of the 40 μ m samples, with some spheres being in clusters, while other places were more open.

4.6 PZT samples

The thicknesses of the sphere layer for the PZT samples were also measured mechanically and in the optical microscope. The mechanically calculated thickness of the sphere layer for the PZT samples are shown in Figure 4.44 and Figure 4.45, where Figure 4.44 is for the glass load samples, and Figure 4.45 is for the WC load samples. All the thicknesses are given in μ m.

32	32.5	37	38.5	38	32.5	
43	40.5	38	33	38	43	
46.5	42	38	47.5	39.5	42.5	
1			2			3
37.5	35.5	30	33.5	36.5	41.5	37
43.5	40.5	40	34	36	33.5	48
48.5	48	42.5	31	37.5	40	48.5
4			5			6

Figure 4.44: Thickness of the sphere layer for the glass load samples calculated from mechanical measurements

38.5	40	32.5	35	40	39
40	44	34.5	37	44.5	42.5
38.5	42	32	36	44	41.5
40	41	34	38	41	38.5
7		9		10	
39.5	38.5	29	30.5	38.5	39.5
37.5	36.5	26	27.5	37	39.5
36.5	35.5	25.5	24	36	38
36	36	25.5	25	35.5	37
11		14		15	

Figure 4.45: Thickness of the sphere layer for the tungsten carbide (WC) load samples calculated from mechanical measurements.

Table 4.10 shows the thicknesses of the sphere layer measured for the PZT samples with the optical microscope. For samples 1, 4 and 6 the thickness was measured along the short side of the transducer, since this cut was already made to remove air-pockets and air-bubbles. The rest were measured on a cut parallel to the longer side of the PZT. Sample 3 was not cut and measured due to the crack that appeared during fabrication.

Table 4.10: Thicknesses of the sphere layers of the PZT samples, measured with the optical microscope. All thicknesses are given in μm .

	Left/front		Middle		Right/back	
Sample 1	44.13	45.53	40.84	40.86	34.74	35.68
Sample 2	40.37	40.38	46.00	45.55	40.39	40.03
Sample 4	43.66	44.60	43.19	41.84	39.30	40.37
Sample 5	40.37	40.37	40.37	40.38	40.37	40.39
Sample 6	46.04	43.66	43.66	44.16	40.39	41.37
Sample 7	40.38	40.37	40.37	40.00	40.37	40.37
Sample 9	38.50	39.90	40.39	40.41	40.39	40.37
Sample 10	42.73	44.60	47.92	48.35	47.90	46.00
Sample 11	40.44	40.39	40.84	40.85	40.44	40.41
Sample 14	40.84	40.39	40.39	40.41	40.39	40.44
Sample 15	38.63	38.16	40.03	40.12	40.00	40.03

Table 4.11 shows the values that was used in Xtrans to fit the graphs to the measured impedance. Sample 1 to sample 6 were made with a glass load, while sample 7 to sample 15 were made with WC load. Sample 4 was cut, but the rest left of the PZT was too small to yield clear peaks for fitting.

Table 4.11: The values used in Xtrans to fit the 1D simulated impedance graph to the measured impedance

	Impedance [MRayl]	Speed of Sound [m/s]	Q	Area [mm ²]
Sample 1	2.3	2450	40	21
Sample 1 (cut)	2.1	2450	20	15
Sample 2	2.4	2400	20	9
Sample 4	2.3	2400	40	21
Sample 5	2.2	2400	30	8
Sample 6	2.4	2400	20	21
Sample 6 (cut)	2.6	2450	25	11
Sample 7	3.0	2450	15	21
Sample 9	3.0	2450	15	21
Sample 10	2.7	2450	15	21
Sample 11	3.0	2450	15	21
Sample 14	3.1	2450	15	21
Sample 15	2.9	2450	15	21
Average (glass)	2.3 ± 0.2	2421 ± 27	28 ± 9	---
Average (WC)	3.0 ± 0.1	2450 ± 0	15 ± 0	---

Figure 4.46 is from the underside of sample 2, though sample 5 showed the same tendency as sample 2. Figure 4.47 show a cross section image of sample 5, which shows how most of the samples looked in the cross section, with the exception being that some samples showed air bubbles in the cross section as well as spheres.

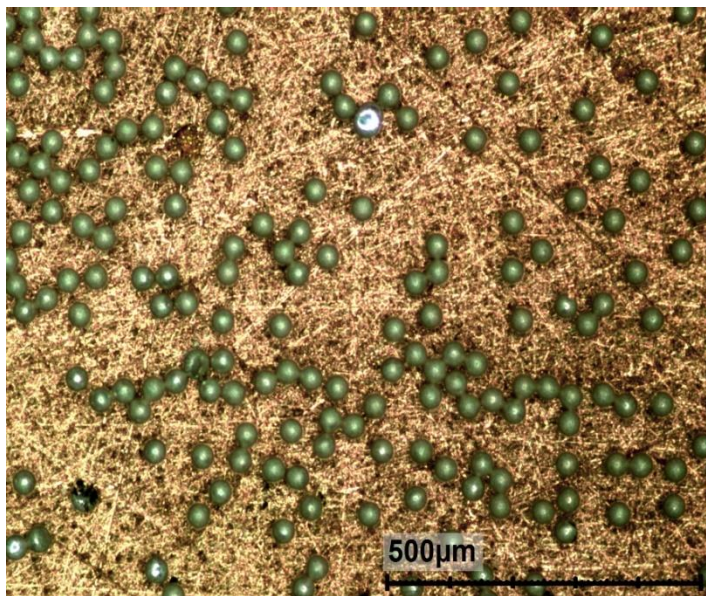


Figure 4.46: The underside of PZT sample 2 taken through the glass, 63x magnification. The green circles are the spheres. Most of the samples showed a similar distribution at some points on the sample, though most also had air bubbles present.

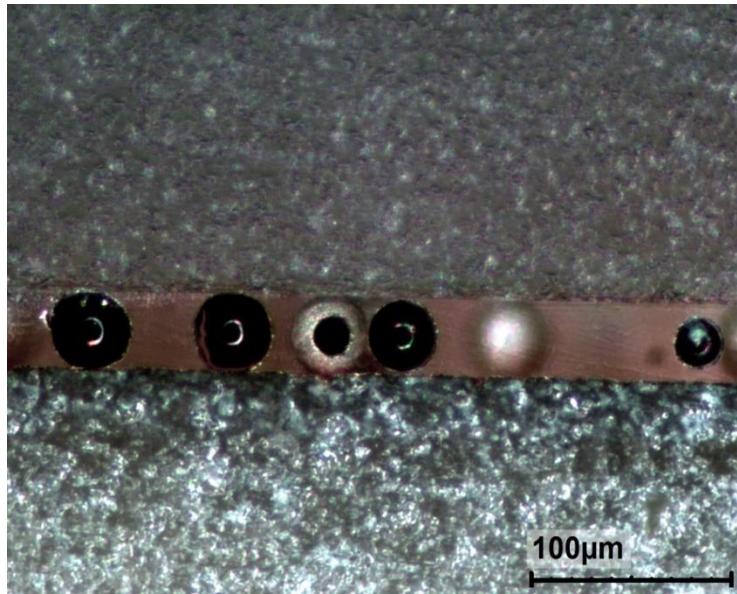


Figure 4.47: Cross section of PZT sample 5, 200x magnification.

The image is showing the common look of the cross section of the samples. The variation between the samples was in the density of spheres and in whether air bubbles were present or not

4.6.1 Failed samples

Several of the glass samples showed the presence of air underneath the PZT, while one, sample 3, cracked during production. Figure 4.48 to Figure 4.51 shows the underside of these samples. Figure 4.48 shows the crack in sample 3, while Figure 4.49, Figure 4.50 and Figure 4.51 show the air that was cut away from sample 1, sample 4 and sample 6, respectively.

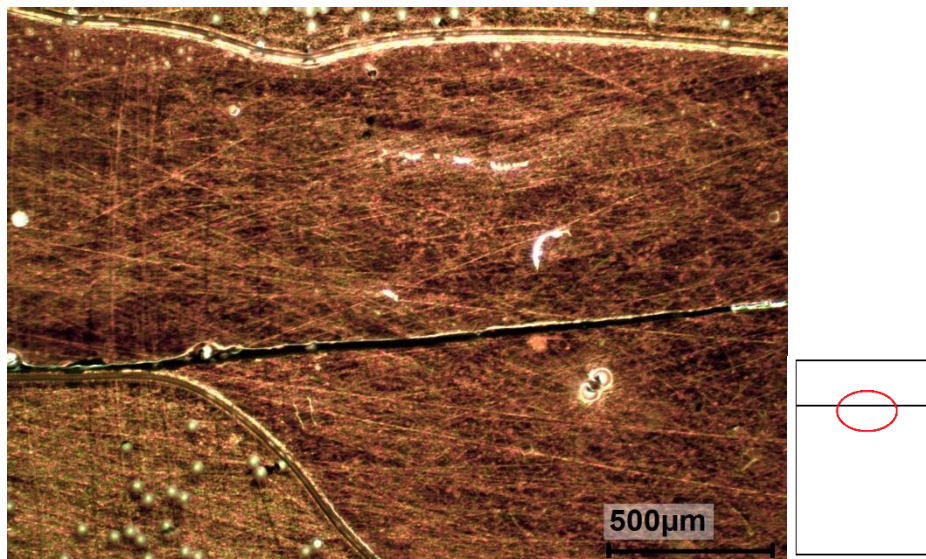


Figure 4.48: The crack created in PZT sample 3 during fabrication, 32x magnification. Placement on the sample is shown to the right.

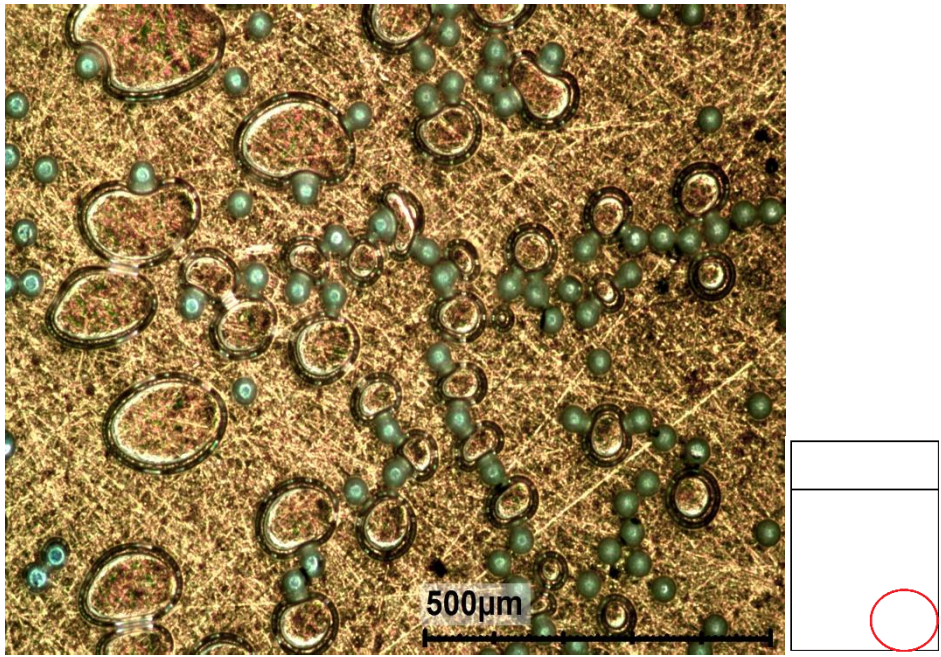


Figure 4.49: Air bubbles in PZT sample 1, 32x magnification. Placement on the sample is shown to the right. This sample had gatherings of air bubbles like this on several places, so the cut away part only removed some.

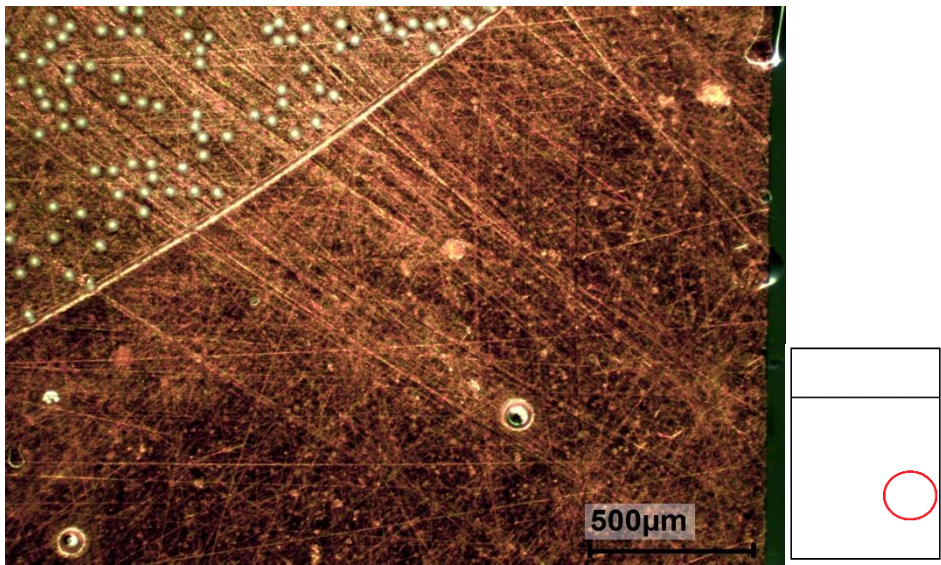


Figure 4.50: Air pocket in PZT sample 4, 32x magnification. Placement on the sample is shown to the right.

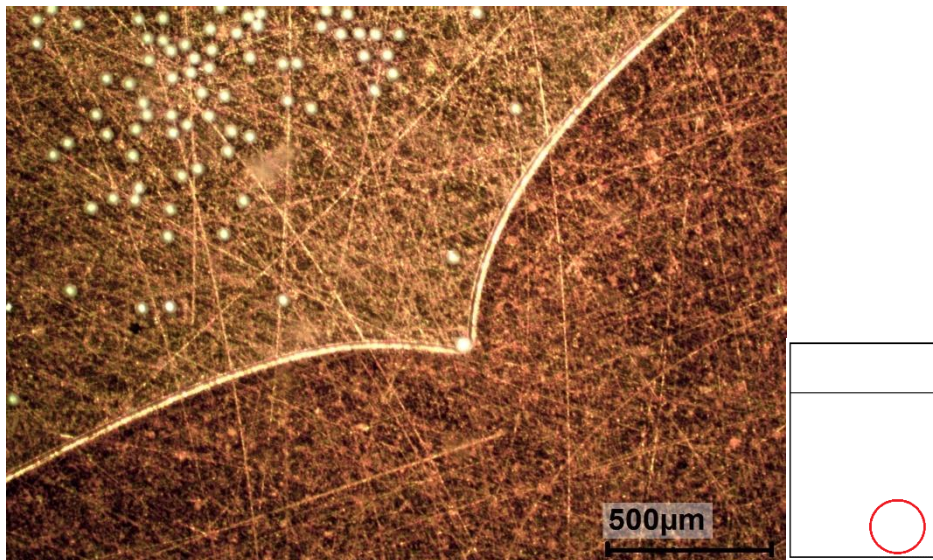


Figure 4.51: Air pocket in PZT sample 4, 32x magnification. Placement on the sample is shown to the right.

4.6.2 Impedance curves

Impedance curves were measured and simulated, both in 1D Mason and 2D FEM, for all the fabricated samples. Figure 4.52 are COMSOL simulated impedance curves for a structure without the sphere layer, with the sphere layer, with the sphere layer and air bubbles, and with sphere layer covering only half of the underside of the PZT. This figure shows how the impedance curve is affected by the addition of spheres and air. Figure 4.53 to Figure 4.65 shows the impedance curves for the PZT samples, with Xtrans and COMSOL in the same graph as the measured curve.

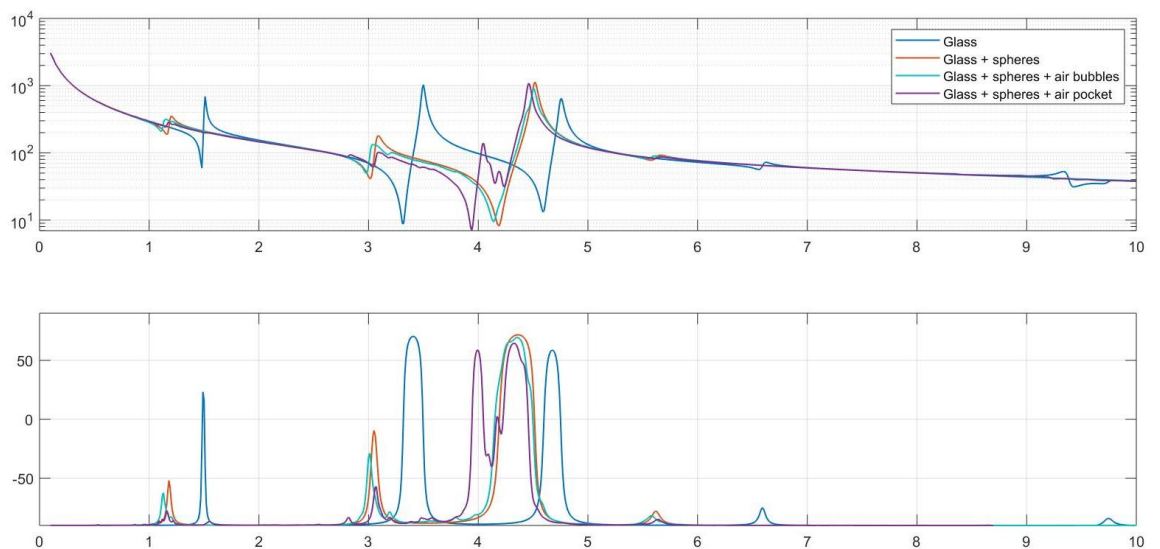


Figure 4.52: Impedance curves simulated in COMSOL, comparing the effect of the sphere layer between the PZT and the load material, and the effect of air between the PZT and the load material

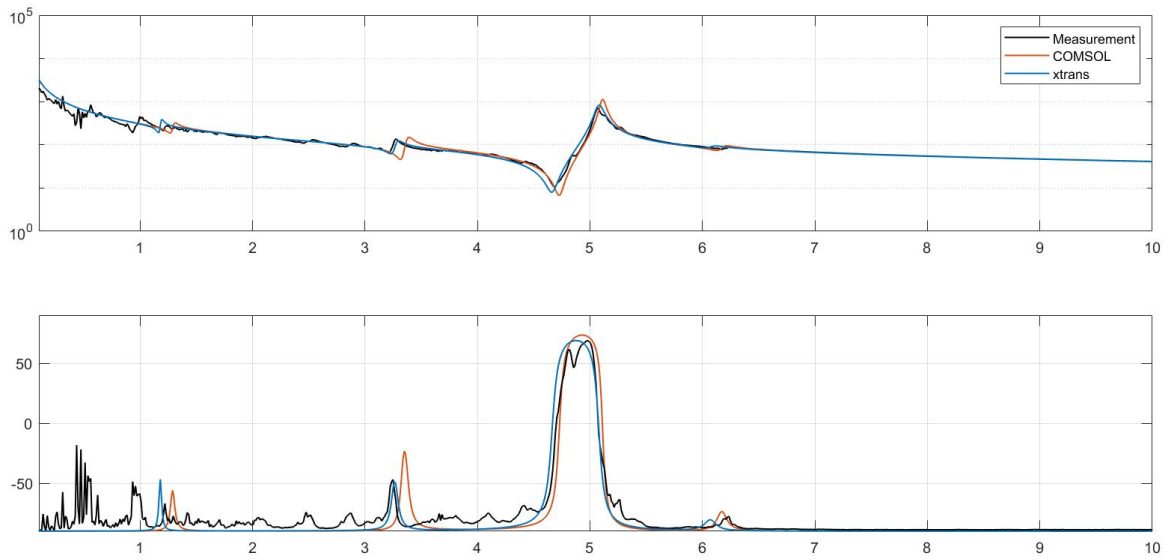


Figure 4.53: Impedance curve (top) and phase curve (bottom) from measurement, Xtrans and COMSOL for PZT sample 1 before air-bubbles were tried cut away.

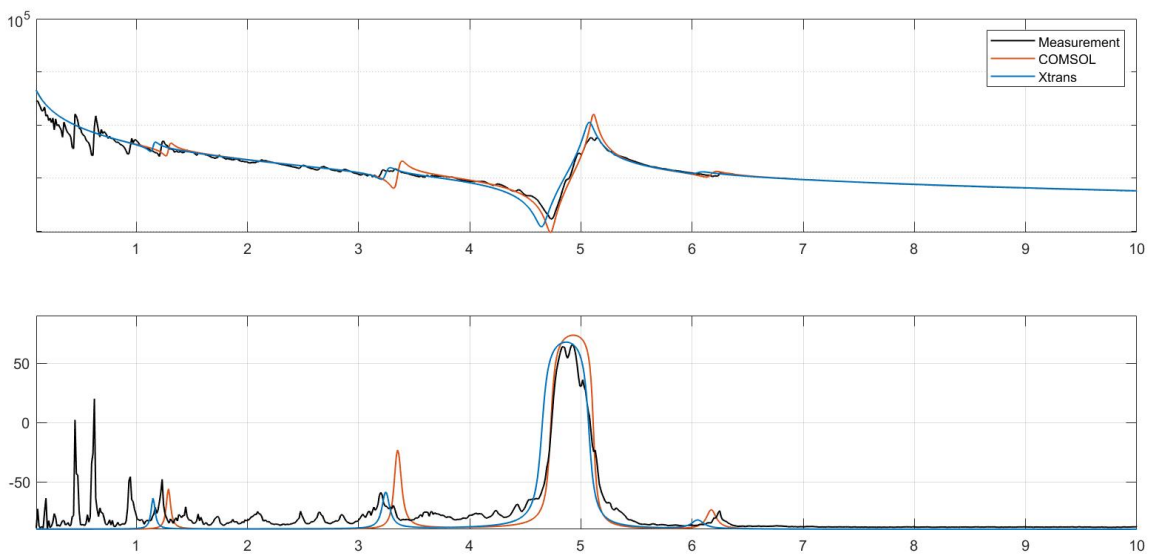


Figure 4.54: Impedance curve (top) and phase curve (bottom) from measurement, Xtrans and COMSOL for PZT sample 1 after the air-bubbles were tried cut away.

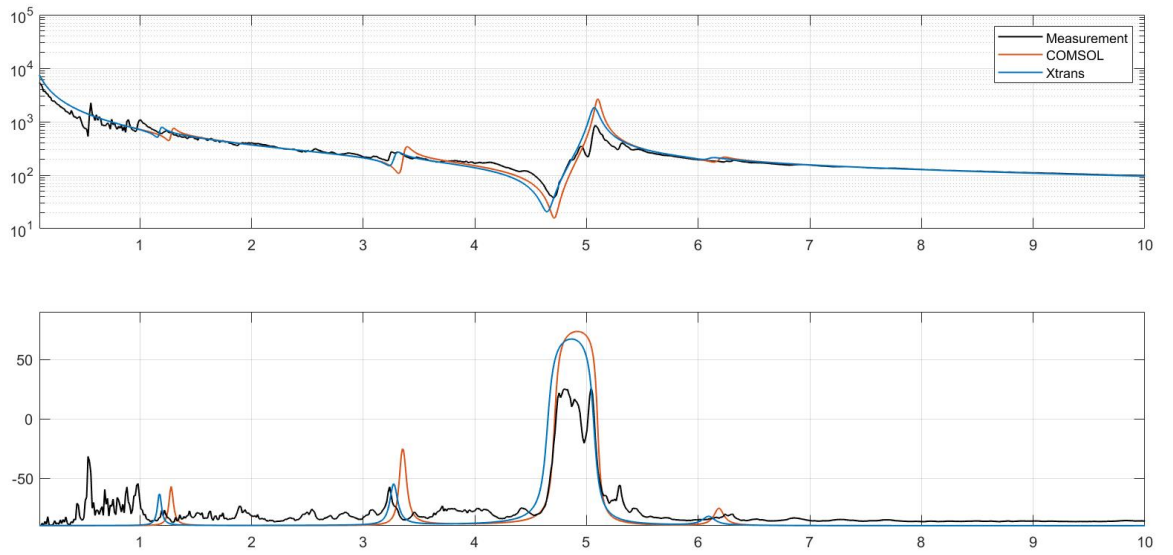


Figure 4.55: Impedance curve (top) and phase curve (bottom) from measurement, Xtrans and COMSOL for PZT sample 2.

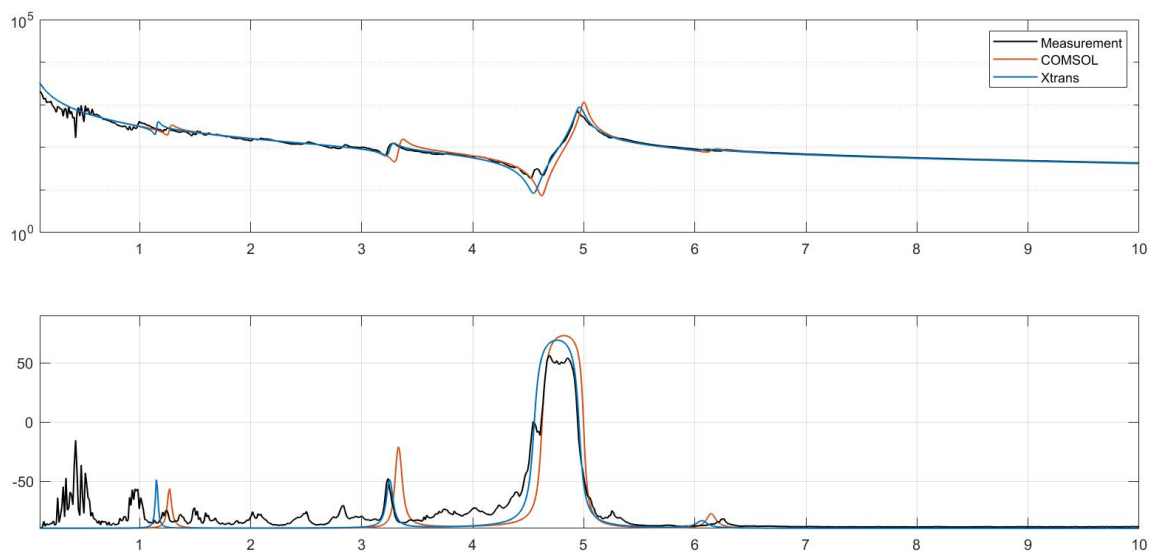


Figure 4.56: Impedance curve (top) and phase curve (bottom) from measurement, Xtrans and COMSOL for PZT sample 4 before the air pocket was cut away. The cut version had too much noise to make a good fit.

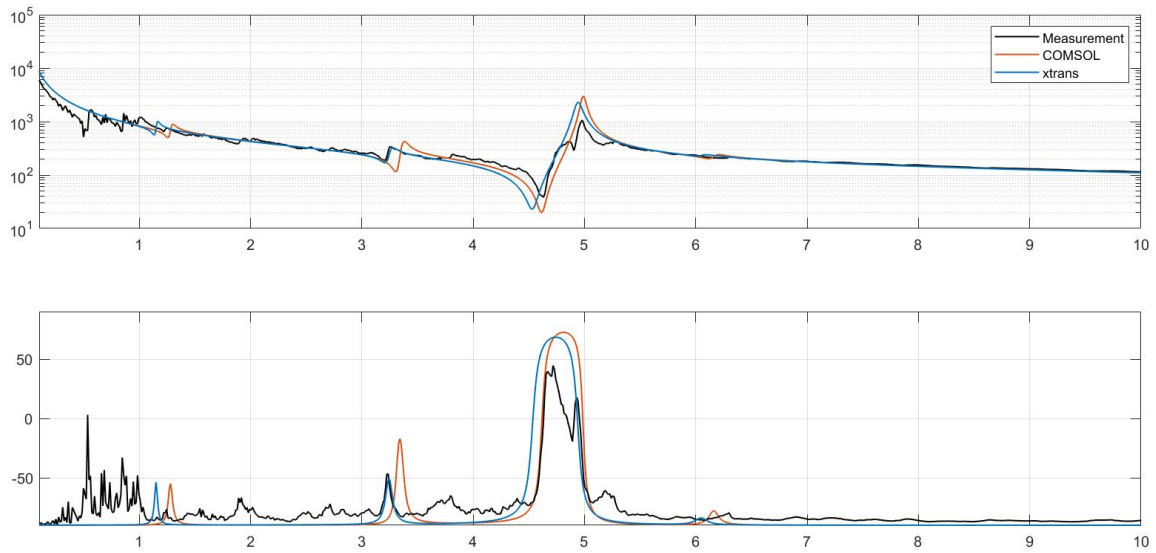


Figure 4.57: Impedance curve (top) and phase curve (bottom) from measurement, Xtrans and COMSOL for PZT sample 5.

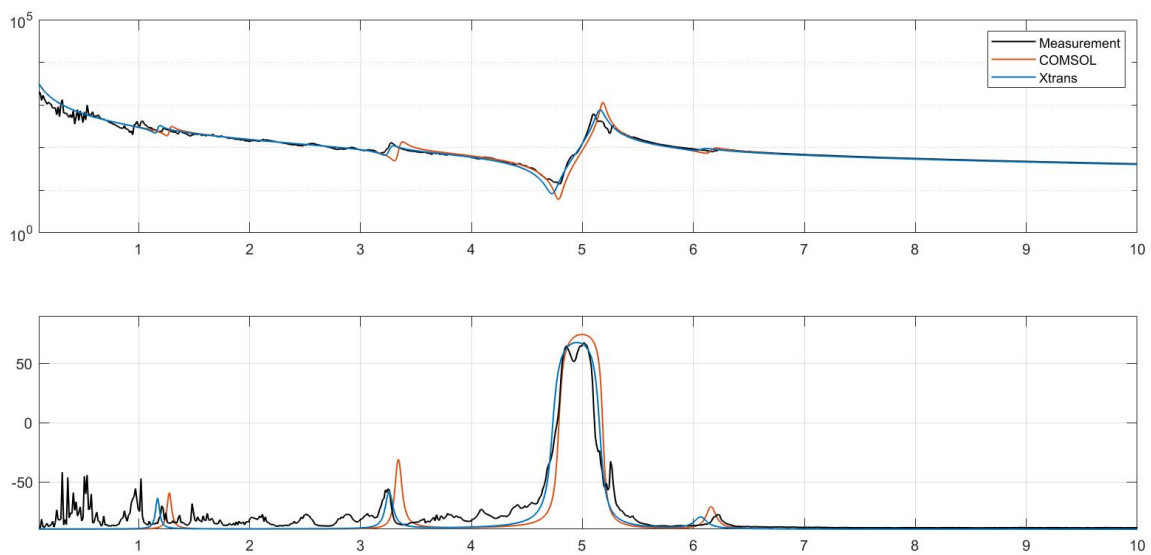


Figure 4.58: Impedance curve (top) and phase curve (bottom) from measurement, Xtrans and COMSOL for PZT sample 6 before the air pocket was cut away.

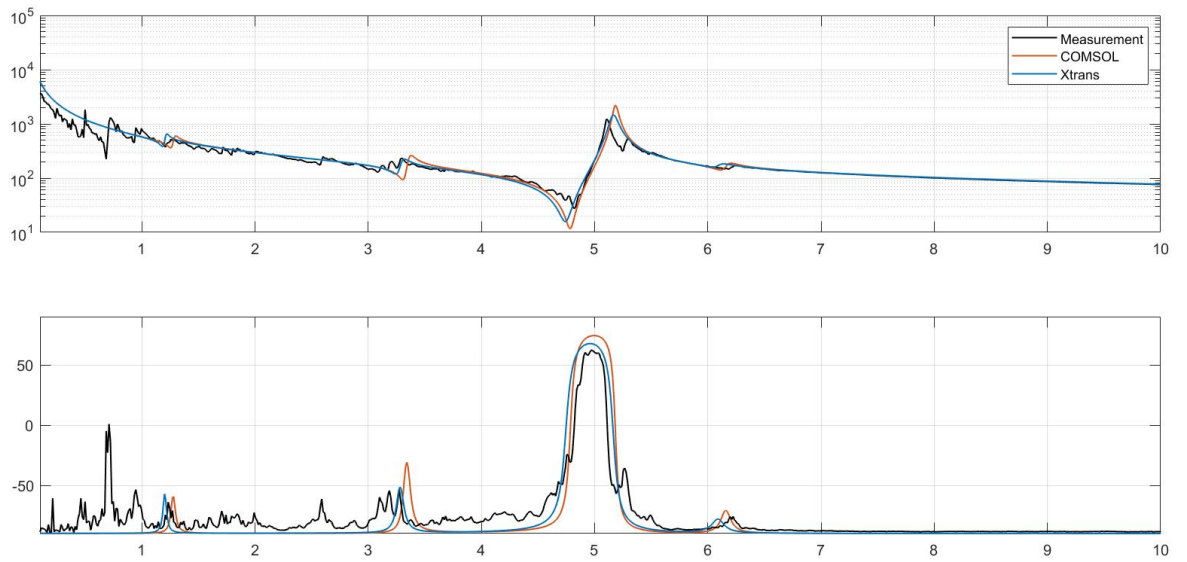


Figure 4.59: Impedance curve (top) and phase curve (bottom) from measurement, Xtrans and COMSOL for PZT sample 6 after the air pocket was cut away.

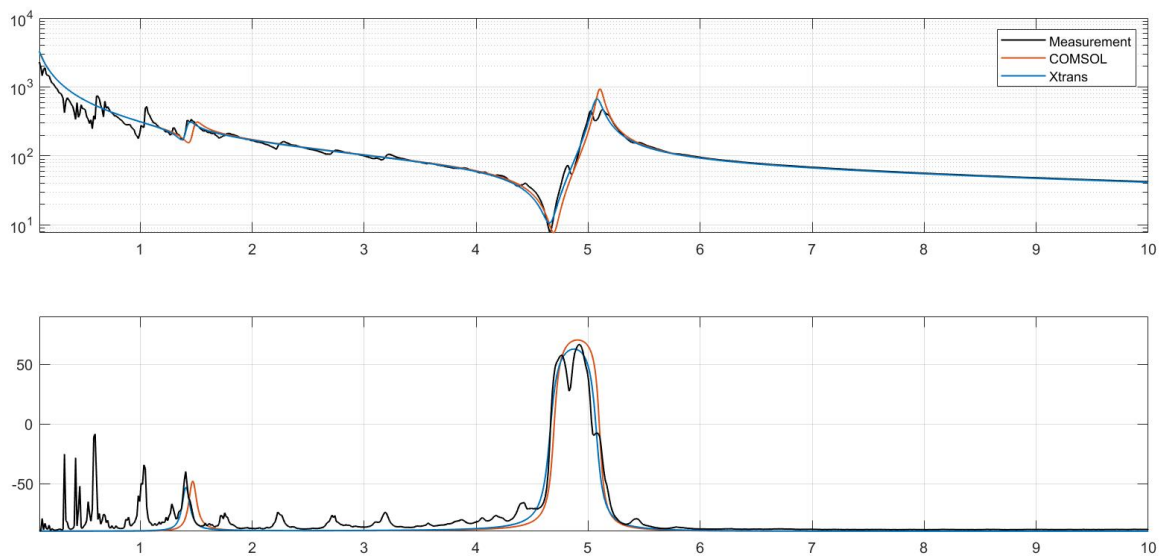


Figure 4.60: Impedance curve (top) and phase curve (bottom) from measurement, Xtrans and COMSOL for PZT sample 7.

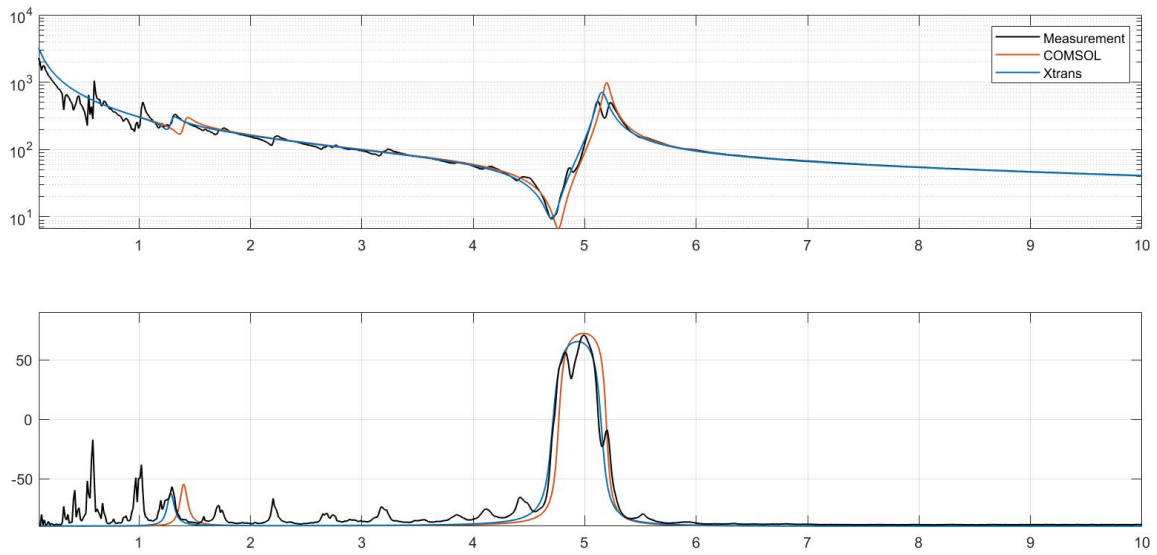


Figure 4.61: Impedance curve (top) and phase curve (bottom) from measurement, Xtrans and COMSOL for PZT sample 9.

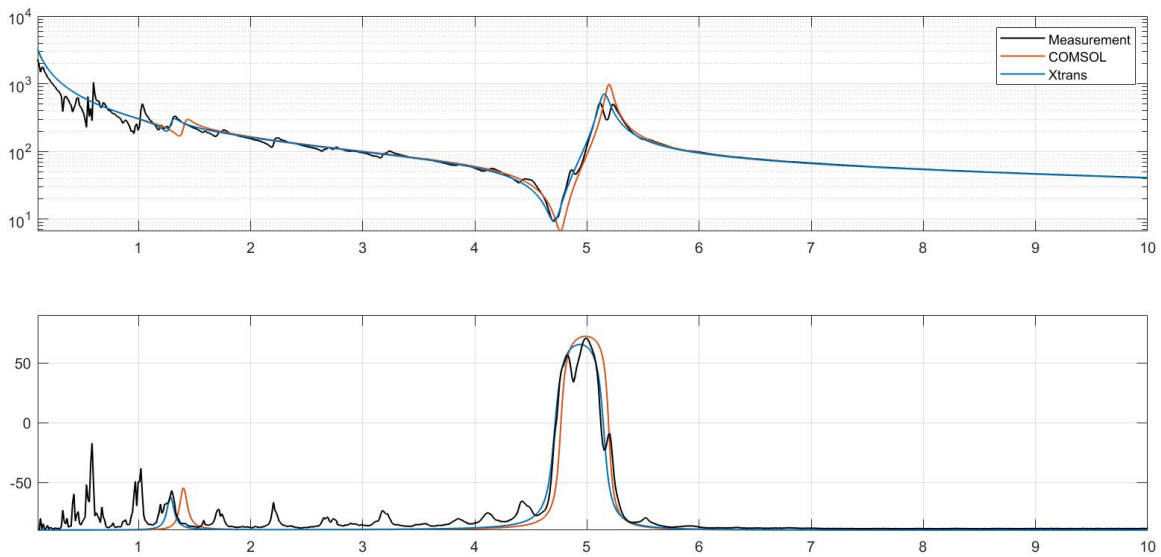


Figure 4.62: Impedance curve (top) and phase curve (bottom) from measurement, Xtrans and COMSOL for PZT sample 10.

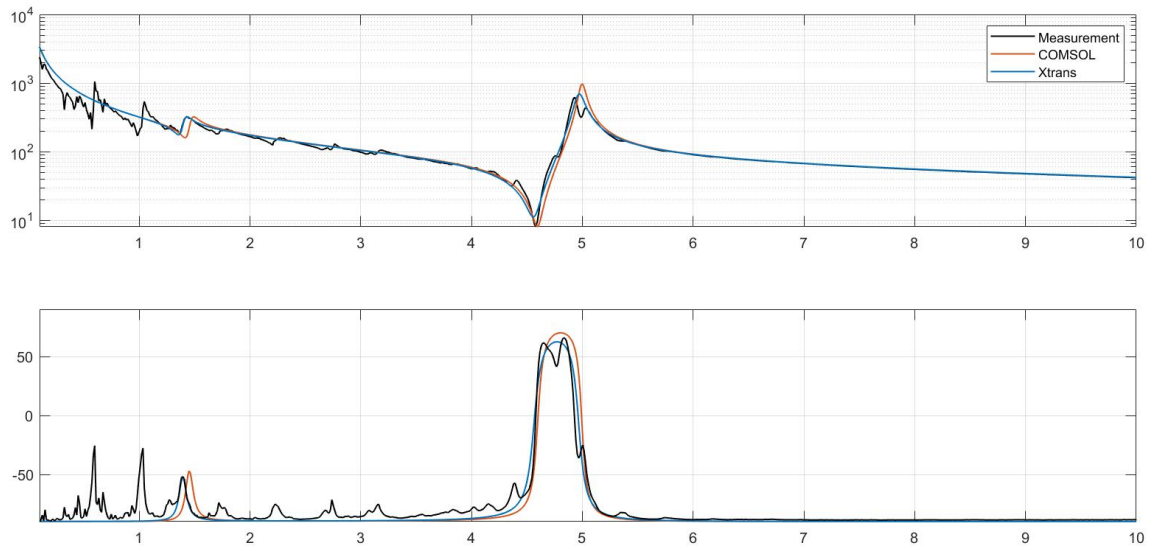


Figure 4.63: Impedance curve (top) and phase curve (bottom) from measurement, Xtrans and COMSOL for PZT sample 11.

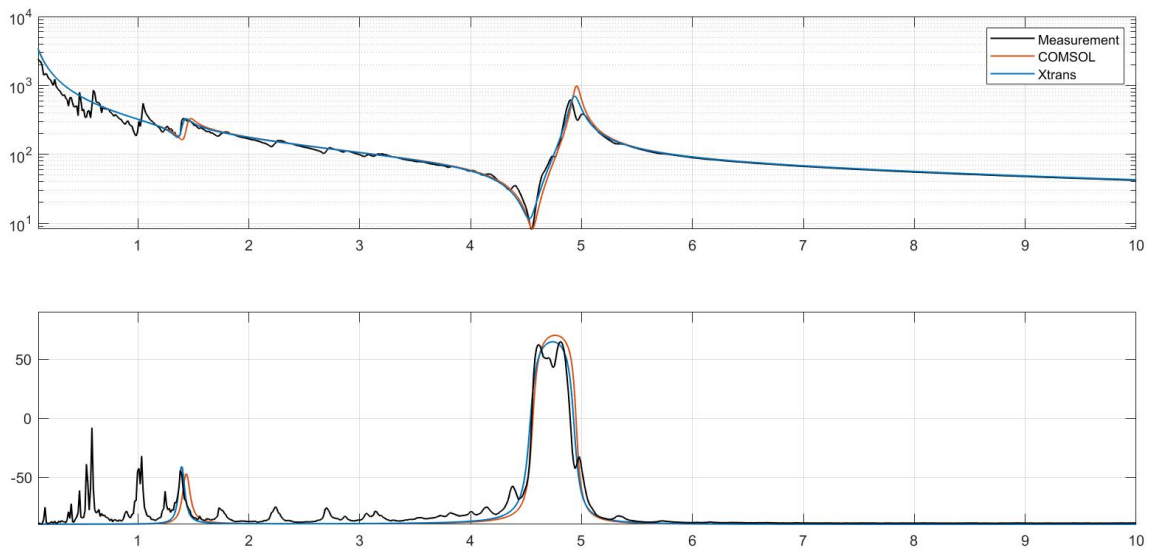


Figure 4.64: Impedance curve (top) and phase curve (bottom) from measurement, Xtrans and COMSOL for PZT sample 14.

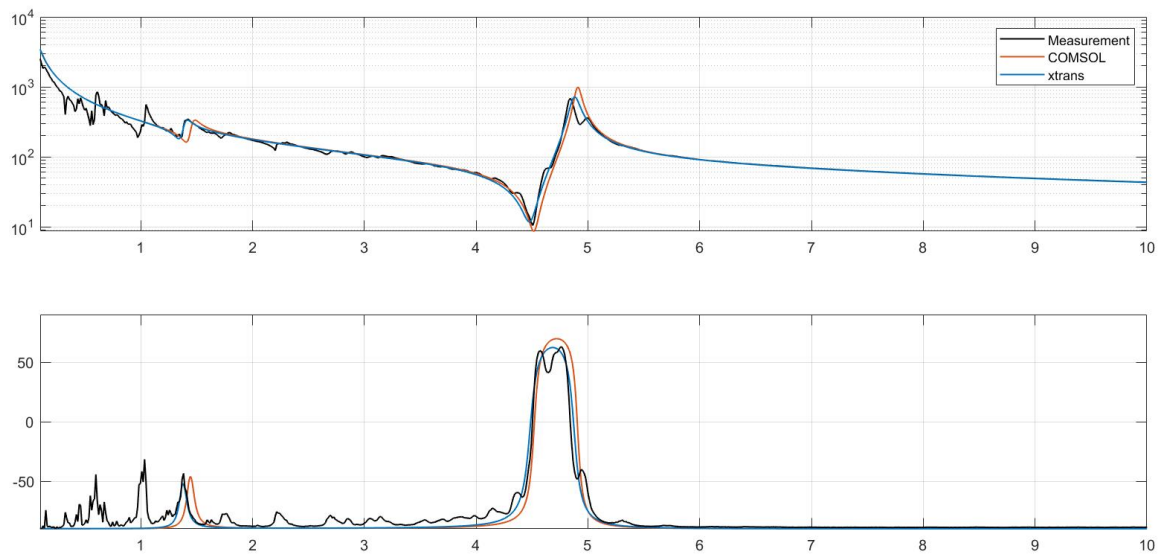


Figure 4.65: Impedance curve (top) and phase curve (bottom) from measurement, Xtrans and COMSOL for PZT sample 15.

5 Discussion

5.1 Trial samples

The graphs for most of the trial samples show impedances with sharp peaks at frequencies where these peaks could be expected, when comparing to simulations. Some show a small spike inside the main resonance, however this was also seen in the PZT discs before any fabrication and was not related to the fabricated layers. The curves that stand out from the rest are the ones for sample 17 and sample 18. These show a larger, uneven spike within the main peak. It is similar to the peak seen in the COMSOL FEM-simulations (Figure 4.52) where half of the sphere layer is replaced by air. However, neither sample 17 nor sample 18 showed larger areas with air, even though the glue in sample 18 had an uneven edge underneath the PZT. The fitting in the 1D Mason model using Xtrans also indicates the presence of this spike inside the main peak. This model only uses the properties of the layers, and does not see the air in the sphere layer, indicating this is a result of thickness resonance. Another effect seen from the FEM simulations in Figure 4.52 is that even small air-bubbles can shift the impedance spectra. Air has both lower acoustic impedance and speed of sound than the sphere layer, and could therefore make the layer softer. Air-bubbles of different sizes would cause different shifts, affecting the sphere property values for the samples. This could therefore be cause for some of the differences between the different samples.

The characteristic acoustic impedance of the samples ranges from 2.6 MRayl to 3.2 MRayl, with some uncertainty being present for the values considering the fitting of the Xtrans curve. However, as can be seen in Figure 4.17, the peak which is most sensitive to the changes in the sphere layer parameter is moved a clear distance with a 0.2 MRayl change in layer impedance. If the value used in the fitting is off by more than 0.2 MRayl, it would be visible, making the uncertainty from this fitting around 0.1 MRayl. The calculated standard deviation is also 0.2 MRayl. The actual fitted values of the samples varied with more than 0.2 MRayl, indicating other effects than the measurement uncertainty. This difference could be a difference in impedance between the layers, caused by air or density of spheres in the layer of one sample compared to the others. The variations seem random, though the variation for the tungsten carbide loaded samples is lower than for the glass samples. However, there are only three tungsten carbide samples and seven glass samples. It is therefore a possibility that this difference could either be that the tungsten carbide samples resulted in a more uniform fabrication than the glass, or that it is a coincidence.

The properties of the sphere layers are found from fitting to the measured impedance, however the thickness of this layer is much thinner than the acoustic wavelength that was tested. Due to this, no peaks are caused directly from the sphere layer, which can be seen in Figure 4.52. The sphere layer has instead shifted the peaks, with the peaks at lower frequencies experiencing the largest effect of different sphere layer property values. As can also be seen in this figure, the addition of air bubbles will shift the impedance graph, with the result typically being a reduction in speed of sound and the acoustic impedance. For most of the glass samples, air bubbles are present when looking in the microscope, and the larger variations in the fitted impedance could therefore be a result of the varying presence of air bubbles in the different samples. The smaller variations for the tungsten carbide load samples could then be that there are less air bubbles present, and thereby less variation. Another factor that could affect the result is how well the composite spread

underneath the PZT, with some having thicker layers and therefore probably had higher density of spheres, in some places, while others had a more even spread of spheres.

5.2 0-3 composite samples

5.2.1 Mixing test

The trial samples of 0-3 composites experienced both floatation, with a monolayer of spheres floating on top of the glue, and sedimentation. It was assumed that the glue and the spheres could separate, since the glue was very thin and the spheres have higher density than the glue. Byk was added to two of the samples, as it is an agent that reduces surface tension and should improve wetting of the sphere surfaces, to see if it would result in more homogeneous samples. As can be seen from the Figure 4.19 and Figure 4.20, the spheres do sediment to the bottom, both in the samples without Byk and those with Byk. The samples with Byk show less sedimentation than the ones without, which would be expected as Byk is added for this specific purpose. The sedimentation of spheres is still large, and a thick layer of spheres did gather at the bottom.

As mentioned, the spheres are heavy, with a density of 1.59g/cm^3 for the $20\mu\text{m}$ spheres and a density of 1.38g/cm^3 for the $40\mu\text{m}$ spheres, compared with the density of the glue, with a density of 1.150g/cm^3 , meaning they should sediment to the bottom. However, some spheres did not sediment, but floated to the top of the glue. The effect is more visible in the sample without Byk than the one with Byk. Seen from above it also seems like the top layer spheres are in the middle for the samples without Byk, while the top spheres are gathered in thinner layers at the edges for samples with Byk. After studying in the microscope, it could seem like the top layer only consisted of one layer of spheres, a monolayer. The presence of spheres at the top surface could be explained by air sacs at the surface. These air sacs would be very small, as they are not visible in the microscope, and would not be able to carry a lot of the spheres. However, if the air sacs are in between the spheres, a monolayer of spheres could be possible to carry. This could also be used to explain the lack of such a monolayer in the middle for the samples with Byk, as the additive is meant to reduce foaming, and therefore could hinder the creation of the air sacs that holds the spheres in the samples without Byk. The spheres along the edges could be sticking to the cup through static electric forces.

At the time of the mixing of the of the first samples, the density of cured Epo-tek 301-2 had neither been found in a reference, nor had it been calculated for a sample. Only the density from Epo-tek 301-2 part B was found in the data sheet, and this was therefore used at that time to calculate the weight of spheres to be added to the mix. The density of the mixed Epo-tek 301-2 is however higher than that of part B, which was indicated by the calculated value from the pure Epo-tek 301-2 sample. The value of $1.136 \pm 0.008\text{ g/cm}^3$ is close to the value of 1.150 g/cm^3 from [24], which was found after the mixing trial samples were made. The value from the paper is in this case just outside the uncertainty bounds. Some of the difference may be uncertainty, considering only one sample was made, though some of the reason may also be air bubbles in the sample. The samples were not vacuumed before curing, as the vacuum pump was not available at that time. The densities for the initial mixing trial samples, SoS1 to SoS4, on the other hand, are not as expected, as some of these are lower than the calculated value for the mixed Epo-tek 301-2. Considering the density of Epo-tek 301-2 is lower than the density of the spheres, the sample density should be higher than the

density of Epo-tek 301-2. As with the pure Epo-tek 301-2 sample, this could be due to air-bubbles being present in the sample, as these were not vacuumed before curing either.

5.2.2 Speed of sound samples

The lower density values for the speed of sound samples are not only present for the mixing test samples, but also for the measured speed of sound samples. For samples SoS5, SoS6, SoS8 and SoS10 the difference in density is small and can easily be caused by the slight difference in added spheres and the actual sphere weight that should be added, or measurement errors. For samples SoS9, SoS11, SoS12 and SoS13 on the other hand, another explanation exists. As mentioned, the density of the speed of sound samples should be somewhere between that of the glue and the MPS, however, these samples too have densities below that of Epo-tek 301-2. Some of the lower density, for all of the samples, could be explained by some gradient of spheres through the samples, with a thin layer of spheres at the bottom of the cured sample which would be removed during grinding. This could however only explain small differences, with the most likely explanation for the values below that of the glue being the air bubbles that are observed with a microscope at the cross section of almost all the samples.

The speed of sounds measured for the different samples does not vary a lot within the specific sphere size, with a standard deviation of 50 m/s (1.9% of the average) for the 20 μm spheres, and 40 m/s (1.6% of the average) or 27 m/s (1.1% of the average), depending on the signal that is registered, for 40 μm spheres. The air bubbles are too small to cause any reflection, however as seen in the results, it does affect the density and would probably also affect the stiffness. The measured speed of sound could then be lower as an effect of the bubbles making the material softer.

Blomvik [20] in his Master's thesis looked at the speed of sound for samples containing MPS through simulation in FEM, though he used a volume fraction of spheres of 48% and 50%, which is around five times what was used for the samples in this thesis. The simulations done in the thesis indicate that both a thicker silver layer and higher volume fraction will decrease the speed of sound, while a larger sphere diameter increases the speed of sound. The results of my COMSOL simulations support his results to some degree. In the graph in Figure 4.28, the average values for the speed of sound simulated for the 40 μm spheres are higher than the average values for the 20 μm spheres, and the speed of sound decreases with increasing volume fraction. However, experimental results when measuring speed of sound in the fabricated 0-3 composite samples showed the opposite result. The average measured values for the speed of sound of the 40 μm spheres are 2449 ± 34 m/s, while the average value for the 20 μm spheres is 2586 ± 50 m/s. The simulations, both done in this thesis and by Blomvik, indicate that the 40 μm spheres should have a higher speed of sound than the 20 μm spheres. However, the physical 0-3 composite samples have air-bubbles, which has not been accounted for in either of the simulations. Air pockets will make the sample softer and less dense. Even though the bubbles are too small to have any visible effect when it comes to the reflected and transmitted signal, the reduced stiffness may slow down the signal going through the sample. Two of the 20 μm samples did not show air-bubbles when investigated in the microscope, but the speed of sound results from the samples with air-bubbles were comparable to those without. This may indicate that the air-bubbles did not slow down the signal, however, this is for the 20 μm case. The 0-3 composites with 40 μm spheres had air-bubbles across the whole cross section that was investigated with the microscope, while the 20 μm samples had points where there were no air-bubbles. The calculated volume fraction of air is also

mostly higher for the 40 μm samples than for the 20 μm samples, which means the effect would be higher for the 40 μm sphere samples than for the 20 μm sphere samples. The simulation that was done indicates that the difference in speed of sound is not very large at 10% volume spheres, with difference of the average value being only 3 m/s, and the standard deviation make them overlap. The larger difference seen for the measured samples are therefore likely to be caused by the air present in the samples. For the Epo-tek 301-2, the speed of sound from the reference is 8% higher than the simulated value, however, this is probably down to the parameters which are used. A calculation for the values used in the parameter gives a speed of sound of 2432m/s, which is the same as the simulated value. This indicates that the difference between the simulated values and the measured values and reference values for the speed of sound is due to the property values used in the simulation.

5.3 Thermal conductivity

As can be seen from the temperature distribution figures, the heat rises faster around the edge of the spheres than it does inside the spheres and further out from the sphere. Silver has a much higher thermal conductivity than PMMA, making it natural that the coating conducts heat faster than the PMMA of the core and surrounding media, even though the silver layer thickness is less than 1% of the sphere diameter. Looking at the temperature distributions, it seems clear that the heat conduction is dominated by the silver layer close to the spheres. The core of the spheres seems to have almost uniform temperature, while the heat rise fast around the edge of the spheres, compared to the area a small distance away from the spheres.

Of all the simulations, the 3D simulations would be the most accurate, considering this takes into account the actual shapes of the spheres. The 2D model on the other hand is less realistic, as the spheres are seen as cylinders with a given radius. Usually, the 2D models would have the advantage of shorter computation time, but in this case, both use less than 30 seconds on the calculations. The 2D do still have the advantage that it can run two different simulation methods for calculating the thermal conductivity, both from heat flux and comparison with PMMA, while the 3D can only run comparison with PMMA. This is because the calculation for the heat flux done by COMSOL requires the silver layer to be made, but the meshing in 3D is not fine enough to make this layer.

As mentioned in the methods part, three geometry types for the 2D and two measuring types were used to identify the thermal conductivity. For the 2D geometries where all the spheres were of the same size, geometry type 2, and for the 3D geometry, the actual volume fraction was the same for all cases. The differences in the calculated values using the same method are therefore a result of the distribution. As can be seen in Table 4.6 and Table 4.7, the difference depending on the distribution in the structure is not that large, with standard deviation being less than 2% of the average for all. Some of the structures with geometry type 3, where all spheres are placed at the same y-coordinate and the sphere radius is random, has as low standard deviation as those where all the spheres have the same size. However, for most of the samples where some randomness in size is present, the deviation is larger, indicating that the effect of random size is higher than for the random distribution.

The volume concentration of spheres was set as the same for all 2D models, so the variations in the results for the geometries with variable sphere radius stems from two variables; the variation in size and the variation in placement. As the models where all the spheres were the same size showed, the distribution

has a certain effect on the thermal conductivity. Unlike for the same size geometries, all the spheres do not reach from one boundary to the other for those with variable radius. The heat would therefore have to travel a longer distance through PMMA, with a lower thermal conductivity, and shorter distance through the silver layer, with a higher thermal conductivity, which would reduce the total thermal conductivity of the layer.

The results from the 2D structures varies a lot between the structures. For the 20 μm structures, the highest average value, which is for the same size structure, is approximately $0.050\text{W}/(\text{m}\cdot\text{K})$ (17%) larger than the lowest average value, which is completely random structure, for the method where the sphere layer is compared with PMMA. For the heat flux calculation the highest average is $0.16\text{W}/(\text{m}\cdot\text{K})$ (37%) larger than the lowest average. From these results, it is difficult to determine what geometries are closest to reality. The structure that is least likely to be accurate is geometry type 1, where both sphere size and placement of the spheres are random. This is the geometry furthest away from how the cross section would look, and also the one with the largest variation in results. The other two geometries, on the other hand, has some correlation with the real samples. Geometry type 3 is close to how the real cross section would look, with the spheres having the same center placement in the y direction, but are cut at different places. However, it does not indicate that all the spheres at some point touches both the top and the bottom surfaces of the layer. Geometry type 2, where all the spheres have the same size, takes this into account, but does not take into account that the spheres are not in contact at all points. For the impedance measurement, the size, whether it is the same or random, does not have a big effect on the result. However, the thermal conductivity calculated with the same size structures is generally higher than the one calculated with the random size, and is also closer to the values from the 3D simulations, which is the model closest to the real case.

For the 2D geometries with some randomness, the two calculation methods, comparison with PMMA and calculation from heat flux, gave almost the same answer, with the results from the heat flux calculation being 7% to 10% higher than the results from the comparison. For the structures with geometry type 2, however, the results are quite different. For both the 20 μm and the 40 μm sphere structures the heat flux gives approximately 30% higher average result than the comparison with PMMA. The lower values of the PMMA comparison values could stem from the large difference in temperature that could be experienced around the spheres compared to points on the boundary where there are no spheres. The thermal conductivity is calculated from the average temperature of the boundary, which is pulled down by the areas without spheres and up by the areas with spheres. The same size sphere structure would experience larger variations along the boundary than the structures where the spheres have random radius, which could account for the larger difference there. The method where calculations is done from the heat flux, the average is taken over the whole area of the 2D structure, which could make it more accurate. However, the results from the heat flux generally have a higher standard deviation than the results from the comparisons. The temperature variation of the 3D simulation could have less effect than that of the 2D, since the temperature is taken over an area rather than a line, however it would be interesting to see the values for heat flux calculations for the 3D as well. It may be questioned whether a single thermal conductivity value is appropriate to describe the sphere-epoxy matrix, as the mixture is highly inhomogeneous, and the metal layers form 'bridges' of very high thermal conductivity across the layer.

The conductivities of the 3D structure with a PMMA layer outside the spheres are almost the same as the thermal conductivities of the 2D structures with geometry type 2, when the same calculation is used. For the 20 μm spheres there are no difference on the average value, while the 40 μm has a 6% higher thermal conductivity for the 3D case. As mentioned previously, the 3D models could only calculate the thermal conductivities based on comparison with PMMA due to problems with meshing the silver layer. The thermal conductivity of the structure with a thin PMMA layer between the spheres and boundary of the structure have lower thermal conductivity than the structures with no PMMA. The drop from no PMMA to some PMMA is approximately $0.020\text{W}/(\text{m}\cdot\text{K})$ (7% drop). This decrease is due to the PMMA layer, as the number of spheres is the same, even though the layer is a little thicker. The heat would have to go through this extra layer as well, which is the most likely cause for the reduction in thermal conductivity. The temperature variations along the surface might also be smaller, with the PMMA somewhat evening out the difference.

Gakkestad et.al. [22] investigated how the thermal conductivity varied between isotropic conductive adhesive with different volume fractions of MPS. The investigation indicated, as would be assumed, that an increase in volume fraction of MPS increases the thermal conductivity. It also indicates that larger spheres give higher thermal conductivity per volume fraction silver than smaller spheres. However, they also give lower thermal conductivity per volume fraction spheres. The same was seen in the simulations in this thesis, as the structures with 40 μm spheres showed lower thermal conductivities than the structures with 20 μm spheres. The difference range from 1% higher value for the 20 μm sphere structure with geometry type 3 calculated with PMMA comparison, to 9% higher value for the 20 μm sphere structure with geometry type 2 calculated from the heat flux. This difference could be explained by the increased volume fraction of silver for the smaller spheres. The thickness of the silver layer was the same for both cases, making the volume fraction of silver higher for the 20 μm cases, and thereby causing the higher thermal conductivity. The small difference could be due to the low volume fraction, making the difference in actual silver fraction small.

5.4 Monolayer samples

5.4.1 Monolayer fabrication challenges

The silicon samples were made to test the fabrication procedure and see how it worked with a well-defined, very flat substrate. Silicon is not a piezoelectric material, and investigations of these samples for acoustic properties was not possible with the methods available in our lab. For the most cases, the thickness achieved with these samples were closer to actual monolayers than what was achieved with the initial samples. The only process difference was that the trial samples with PZT were put directly in the oven, while the silicon samples were outside for half an hour. This was done to allow the glue to be pressed out and the layer to be created before curing began. The time in the oven also differed, as the trial samples were made with a glue that did not need as long curing time as the glue that was used on the later samples. The trial samples were also made under pressure of time, as this was done in another lab, reducing the time they could be in the oven. However, the trial samples continued curing in air for a long time after they were made, and by the point they were taken out of the oven, the glue had hardened. The thinner layer cures faster than a thicker layer, so the initial samples, being put right in the oven, could experience stiffening of the glue before a

monolayer could be made. Also, both of the weights were used on several samples at the same time, however, the weight 320 g divided over several samples is probably too little to achieve a monolayer. If divided over five of the samples with the smallest area, the pressure on each would be approximately 12.5 kPa, while the 1.8 kg weight would give a pressure of approximately 70 kPa for the same case. The weights used for the silicon samples were 675 g, 835 g and 1.12 kg, giving each sample a pressure between 66 kPa and 110 kPa. The pressures are therefore between 4 and 7 times larger for the silicon samples than for the trial samples with the lightest weight on the smallest PZT pieces. This could, together with the extra time outside the oven, explain the thickness differences.

The silicon samples also indicated that a big determinant for whether a monolayer was made or not had to do with how much of the glue-sphere mix was applied, and the tape. As mentioned, the mix was applied in drops, but getting exactly the same size of drop on all samples was extremely difficult, as the amount of glue sticking to the plastic stick varied from application to application. Some samples, like S5, got a bigger drop than other samples, and more than what was needed to fill the underside of the silicon piece. When the weight was added in this case, the glue was squeezed out, but the tape hindered the glue from being squeezed out in two directions. This caused the glue to remain under the silicon piece, and the layer to be thicker than a monolayer. Too small amount of the glue mix, however, would not allow the whole underside of the Si piece to be covered. A more accurate way of applying an exact volume of the mix would therefore help in making the monolayer.

5.4.2 PZT vs silicon samples

A problem that occurred for both the silicon samples and the PZT samples were air bubbles. Several things could be the cause of this, though some are more likely than others. One possibility is that the air bubbles were in the mix before it was applied, however, it was vacuumed for 15 minutes before being used, which should prevent this. The air bubbles could also have been introduced in the application process, with the application from the plastic stick being most likely. Air-bubbles could be created when the plastic stick is put in the glue, or when the glue is added to the load. This is probably the cause of the smaller air-bubbles near the center of the pieces, as everything else was cleaned before use for the PZT samples. The larger bubbles along the edges of PZT sample 1 and the air-pockets underneath both PZT sample 4 and sample 6, as well as some of the silicon samples, could be caused by the movement of the weights. These are too large to stem from application, and is therefore more likely to be a result of air being sucked in due to movement of the weight or even the weight being taken off. The large air-pockets are probably caused by not enough glue-sphere mix being applied, as well as the movement of the weights or the weight coming into contact with the sample on one side, then the rest. Some of the reason for making the samples smaller than the silicon pieces was that it would be easier to get enough of the glue-sphere mix to fill the whole underside. However, the smaller size increased the risk of adding too much of the glue-sphere mix, which has probably affected the application process.

For the thickness calculation, it could, at first glance, seem like the mechanical measurement and optical measurement of the Si samples fit better than for the PZT samples. Closer inspection shows that both the Si samples and the PZT samples had approximately the same difference in mechanical and optical measurement, with the difference between the two measurement types ranging from 2 μ m to 10 μ m. The error in the *Heidenhain Thickness Gauge* is 0.5 μ m, however, the larger difference could be due to other

factors. One factor is where the measurements were done. Even though it was drawn up and written down where the different measurements were done, the sample was not necessarily exactly in that given place. The thickness of the load or the piece on top, either PZT or Si, could be matched with a point on the glass or tungsten carbide that had a slightly different thickness than what was used for the assumed point. More importantly though is that the thickness of the PZT, Si, glass and WC are large compared to the thickness of the sphere layer. Two large values that are subtracted to find a smaller value would give higher uncertainty for that smaller value than it was for the larger, original values, and cause the difference between the optical measurement and the mechanical measurement.

5.5 Comparison fitting and calculation

5.5.1 Difficulties with the comparison

The impedance graphs for the final PZT samples made from Ferroperm's Pz27 showed more spikes at lower frequencies than the PZT used in the trial samples. This is because the lateral dimension of the Pz27 pieces were 4 to 5 times the wavelength at resonance, causing lateral effects to show. These effects are not shown in the ideal Xtrans model, nor in the COMSOL, as the 'Roller' boundary condition used on the sides of the transducer tells COMSOL that the transducer is part of a bigger plate. The lateral modes disappear at higher frequencies where the size of the transducer becomes larger compared to the wavelength in the material. Both the samples with WC load and the samples with glass load has a peak at a frequency within the noise, and the placement of this was assumed through comparisons with the measurement of the Pz27 pieces without a load, and through the peak that stood out, as it was mostly placed where the lateral peaks were beginning to fade.

The impedance curves of sample 2 and sample 5 did not fit with the intended active area of the PZT pieces, but rather indicated that the active area was much smaller. The best fit was found with 9 mm² for sample 2 and 8 mm² for sample 5, compared to the 21 mm² for the intact samples. This was not visible for the first measurement of the impedance, that is for the PZT alone, so any reduction in area must have happened during the fabrication of the samples. The most likely cause for the reduction is a crack in the gold electrode which is too small to see, but large enough to prevent passage of current. The measurement of resistance on the top electrode showed the same resistance between all points, indicating that the crack was on the underside, however, it was not found with the optical microscope.

5.5.2 Comparison of measurement and simulation

The properties of the sphere layers are found from fitting to the measured impedance. None of the peaks stem directly from the sphere layer itself, as can be seen in Figure 4.52, but the peaks are shifted by the sphere layer, with the peaks at lower frequencies experiencing the largest effect of different sphere layer property values. As can also be seen in this figure, the addition of air bubbles will also shift the impedance graph. For most of the glass samples, air bubbles are present when looking in the microscope, and the larger variations in the fitted impedance could therefore be a result of the varying presence of air bubbles in the different samples. The smaller variations for the tungsten carbide load samples could then be that there are less air bubbles present, and thereby less variation. Another factor that could affect the result is how well

the composite spread underneath the PZT, with some having thicker layers and therefore probably had higher density of spheres, in some places, while others had a more even spread of spheres.

The results from the initial samples and the 0-3 composites were used as a starting point for the fitting with Xtrans. None of the peaks that were visible in the impedance spectra were from the sphere layer, however, the sphere layer visibly shifted the peaks at lower frequencies, as can be seen in Figure 4.17. The main peaks on the other hand were not visibly shifted for small changes in the sphere parameters. Though the matching was done for this small peak, it was desired to fit all peaks, which was difficult for the glass load samples. The shift was still very small, and could be due to variations in thickness in the materials, or slight variations in the properties of the materials.

The impedance curves from the COMSOL simulations fitted the main peak very well, with a slight shift for the smaller peaks. The thicknesses of the layers are important when it comes to the placement of the peaks in the impedance spectrum, and the varying thicknesses of the layers could be a cause of the shift seen in the curve, as some of the samples showed larger variations. However, the effect of air-bubbles was also investigated with simulations as seen in Figure 4.52. Though the effect seemed small when the air-bubbles were small, it still moved the impedance slightly, especially around the small peaks used to fit the Xtrans curves. The COMSOL model, on the other hand, was made ideally, and was run without air-bubbles. The measured curve could be affected by the air bubbles present, which would explain why the impedance has moved. Another effect could also stem from the COMSOL model being a 2D model. In this case, the spheres are not seen as spheres, but rather as cylinders, as only the cross section is seen. Since all the spheres are of same size, the model was run with same size spheres, though the difference between the more realistic looking cross section of spheres with different sizes yielded little difference to the one where all were of the same size. A 3D model would have yielded a more accurate result, however, the sphere layer could not be made large enough to simulate the actual transducers that was made. Such a model would also be more complex and would require more time for the calculations than the 2D, which was already quite time consuming, with a computation time between 1.5 and 2.5 hours.

The COMSOL model is an ideal model, without air-bubbles or variations in thickness of the layers, which could both affect the impedance curve. Especially the air-bubbles tend to shift the curves to lower levels, as seen in Figure 4.52. This means that if air-bubbles present in the samples have moved the measured impedance graph, the values found by fitting with Xtrans would be slightly off, though the effect might not be large. All the glass load samples clearly showed air-bubbles when investigated in the microscope, and though not all the tungsten carbide samples showed air-bubbles in the cross section cut, air-bubbles could still be present in the sphere layer, slightly shifting the impedance curve. This shift is especially visible around the peaks, which is used to fit the Xtrans curve, and could explain the lower acoustic impedance value found for the glass samples compared to the WC samples. The samples that could indicate otherwise are sample 2 and sample 5, which did not show large air-bubbles or air-pockets underneath the PZT. However, as mentioned, the active area of these were smaller than assumed, and some air-bubbles were present for these two samples as well. If the air-bubbles were within the reduced active area, the effect could be more visible than it would have been for a full active area, explaining the low acoustic impedance seen for these samples as well. The WC samples on the other hand showed few air-bubbles in the cross-section, though there could be more present underneath the PZT. The values do however suggest that there

are not that many air-bubbles underneath the WC, which could indicate a more uniform fabrication for the WC samples. The average value of 3.0 ± 0.1 MRayl for the acoustic impedance of the WC samples is above the value from the 0-3 composites when using the ideal density to calculate the acoustic impedance. This difference could be an effect of possible lower speed of sound for the samples due to the air. The average value of the PZT samples with glass load is also quite close in number, though the average value of 2.3 MRayl is 23% lower than that of the WC samples, and 20% lower than the average from the 0-3 composites. However, this could be an effect from the air bubbles, as the maximum uncertainty gives an acoustic impedance of 2.7 MRayl, which is 10% lower than the average value found for the WC samples, and 6% lower than the average of the 0-3 composites. The higher acoustic impedance of the WC samples could be a result of the speed of sound measured in the composites is lower than the actual value. Even though 2450 m/s gave the best fit for the WC samples, a higher speed of sound of 2500 m/s and even 2600 m/s could be used with a lower impedance to get a fit that was almost as good as for the property values that were used.

The speed of sound values found with the PZT samples were generally lower than those found in the trial PZT samples. However, most of the trial samples used 20 μm spheres instead of 40 μm spheres, which would make it likely that there is a difference, though not a large one. The results from Blomvik seem to indicate that a larger radius of the spheres slightly decrease the impedance of the composite, which fits with the values calculated from the speed of sound samples. For 40 μm sphere he also indicates that the impedance is around 3.3 MRayl, while the impedance found with the PZT samples were somewhat lower. The density of the composite will increase for a larger volume fraction of spheres, which could indicate that the characteristic acoustic impedance should increase. However, the speed of sound, which decrease with volume fraction also has an effect, making the total effect unclear. In addition, the results from Blomvik are all from simulations and therefore idealized. Any effects of air-bubbles which are present in the physically fabricated samples here is not taken into account in his results

6 Conclusion

In this thesis, metal coated polymer spheres were characterized, and the results from fabricated samples were compared with Xtrans simulations, FEM simulations and previous studies.

Initial samples, using PZTs with wrap around, were made to see the effect of the MPS and figure out how to make the monolayer of spheres. These samples indicated difficulties in making the monolayer, and also gave an indication that the speed of sound was somewhere between 2700 m/s and 3200 m/s, and that the acoustic impedance was somewhere between 2.8 MRayl and 3.2 MRayl. The measurements also showed that the sphere layer shifted the impedance curves, with the largest shift being for the smaller impedance peaks at frequencies below that of the main peak.

0-3 composites for speed of sound samples were also made. Almost all of these samples had air bubbles after spinning later in the curing process. Though the air bubbles were visible in the form of lower density for some of the samples, the measured speed of sound did not vary for those where the density was affected compared to those where the density was not affected. The measured speed of sound had an average of 2449 ± 31 m/s for the 40 μm spheres, and 2586 ± 50 m/s for the 20 μm spheres. It is assumed that the air-bubbles present in the samples have slowed down the speed of sound, at least for the 40 μm sphere samples.

Samples on glass substrate made from glass, MPS mixed with epoxy, and Si were fabricated for both 20 μm spheres and 40 μm spheres. The method for making the monolayer was tested with these samples, and different techniques for applying tape and pressure was used, with the most successful being to apply the tape lightly before placing a weight on top of the sample. The mechanical way of measuring the thickness of the layer gave an indication of the thickness and the thickness variation, but some error showed, as a result of two large numbers being subtracted.

Samples with Pz27 piezoceramic glued to glass or WC loads were fabricated for the 40 μm spheres, with the Xtrans graph being fitted to the measured impedance graph. The average values for the glass samples were 2.3 ± 0.2 MRayl for the characteristic acoustic impedance and 2421 ± 27 m/s for the speed of sound. All the samples were somewhat affected by air-bubbles, which would shift the graph to lower values. The WC samples did not show as much air, and had average characteristic acoustic impedance of 3.0 ± 0.1 MRayl and average speed of sound of 2450 ± 0 m/s. The COMSOL model showed a deviation that was almost the same for all the sample, likely caused by shifting of the curves by air bubbles inside the glue layer.

Thermal conductivity of the sphere layer is increased by around 70% from the thermal conductivity of 0.190W/(m*K) of the PMMA, with heat conduction mainly happening in the silver layer. 2D simulations where all the spheres have the same size can give an indication of the value, though more accurate results were obtained from the 3D simulations. The thermal conductivity of a layer that is the same thickness as the sphere diameter is approximately 0.325 ± 0.001 W/(m*K) for 20 μm and 0.320 ± 0.002 W/(m*K) for 40 μm spheres. An increase in the layer thickness above and below the spheres decreases the thermal conductivity.

6.1 Future work

Based on the results in this thesis, following recommendations are made for future work:

- Determining a method for fabrication of 0-3 composite samples without air-bubbles for accurate determination of speed of sound
- Determine a method for making monolayers without air bubbles and test for what volume percentages a monolayer can be made
- Fabrication of monolayers using spheres with other diameters, like 20 μm to determine the effect of monolayers of different thicknesses and with different silver coating thicknesses.
- Determine the thermal conductivity through the layer by a second simulation method for 3D or by fabrication of samples.

References

- [1] T. L. Szabo, *Diagnostic Ultrasound Imaging: Inside Out*, Elsevier, 2013.
- [2] T. R. Shrout, "Innovations in Piezoelectric Materials for Ultrasound Transducers," IEEE, 2008.
- [3] R. R. Tummala, in *Fundamentals of Microsystems Packaging*, Atlanta, Georgia, McGraw-Hill, 2000, pp. 212-262.
- [4] H.-V. Nguyen, K. E. Aasmundtveit, H. Kristiansen and T. Helland, "An Overview of Isotropic Conductive Adhesives Filled with Metal-coated Polymer Spheres," in *46th International Symposium on Microelectronics (IMAPS 2013)*, Orlando, Florida, 2013.
- [5] S. K. Blomvik, *Finite Element Approximation of the Acoustic Impedance in Transducer Layers Comprising Silver Coated Monodisperse Polymer Spheres in a Polymer Adhesive*, Trondheim: NTNU, 2017.
- [6] W. Jiang, H. Wang and W. Cao, "Characterization of lead zirconate titanate piezoceramic using high frequency ultrasonic spectroscopy," *Journal of Applied Physics*, Vol. 85, pp. 8083-8091, July 1999.
- [7] E. Samei and D. J. Peck, in *Hendee's Physics of Medical Imaging*, Oxford, Wiley Blackwell, 2019, pp. 305-338.
- [8] L. E. Kinsler, A. R. Frey, A. B. Coppens and J. V. Sanders, in *Fundamentals of Acoustics*, John Wiley & Sons, Inc., 1999, pp. 149-150.
- [9] K. Worden, J. Haywood and W. A. Bullough, in *Smart Technologies*, World Scientific Publishing Company, 2003, pp. 141-170.
- [10] D. Ensminger and L. J. Bond, *Ultrasonics: Fundamentals, Technologies, and Applications*, New York: Taylor & Francis Group, 2011.
- [11] C. S. Desilets, "The Design of Efficient Broad-Band Piezoelectric Transducers," IEEE, 1978.
- [12] G. Liu, S. Zhang, W. Jiang and W. Cao, "Losses in ferroelectric materials," *Materials Science and Engineering R*, pp. Vol. 89, p.1-48, 14 february 2015.
- [13] F. P. Incropera, D. P. Dewitt, T. L. Bergman and A. S. Lavine, *Fundamentals of Heat and Mass Transfer*, 7th edition, John Wiley & Sons, 2007.
- [14] S. Sherrit, S. P. Leary, B. P. Dolgin and Y. Bar-Cohen, "Comparison of the Mason and KLM Equivalent Circuits for Piezoelectric Resonators in the Thickness Mode," in *1999 IEEE Ultrasonics Symposium. Proceedings. International Symposium*, 1999.

- [15] COMSOL Inc., "COMSOL," COMSOL, 21 02 2017. [Online]. Available: <https://www.comsol.com/multiphysics/finite-element-method>. [Accessed 11 01 2021].
- [16] D. Popovici, F. Constantinescu, M. Maricaru, F. I. Hantila, M. Nitescu and A. Gheorghe, "Modeling and Simulation of Piezoelectric Devices," in *Modelling and Simulation*, Intech Education and Publisher, 2008, pp. 471-500.
- [17] J. L. Butler and C. H. Sherman, *Transducer and Arrays for Underwater Sound*, Springer, 2016.
- [18] P. Dineva, D. Gross, R. Müller and T. Rangelov, in *Dynamic Fracture of Piezoelectric Materials*, Springer International Publishing AG, 2014, pp. 7-31.
- [19] W. P. Mason, "3f Acoustic Properties of Solids," in *American Institute of Physics Handbook*, McGraw Hill, 1972.
- [20] S. Blomvik, *Finite Element Approximation of the Acoustic Impedance in Transducer Layers Comprising Silver Coated Monodisperse Polymer Spheres in a Polymer Adhesive*, Trondheim: NTNU, 2017.
- [21] BYK, BYK, [Online]. Available: https://www.byk.com/en/product/surface-additives?fbclid=IwAR3r-2gWMI9MQxVxpwk26yNosXuihHq6dIdiTOFMxUNUZpVKkopqdsO_ZIA. [Accessed 28 May 2021].
- [22] J. Gakkestad, Z. Li, T. Helland and C. Wong, "Thermo-Mechanical Properties of Isotropic Conductive Adhesive Filled with Metallized Polymer Spheres," in *2013 IEEE 15th Electronics Packaging Technology Conference (EPTC 2013)*, 2013.
- [23] Ferroperm Piezoceramics A/S, *Ferroperm MatData*.
- [24] T. A. Ritter, T. R. ShROUT, R. Tutweiler and K. K. Shung, "A 30-MHz Piezo-Composite Ultrasound Array for Medical Imaging Applications," *IEEE Transactions on Ultrasonics, Ferroelectrics, and Frequency Control* vol. 49, February 2002.
- [25] P. K. Bolstad, T. Manh, M. Frijlink and L. Hoff, "Acoustic Characterization of Inhomogeneous Layers using Finite Element Method," in *IEEE International Ultrasonics Symposium*, 2021.
- [26] O. M. Brende, "Measurement Report: Acoustic measurement on ACA," Trondheim, 2017.

Appendix

A. Pz27 Ferroperm data

Symbol	Unit	Pz27
$e_{1,r}^s$		1,80E+03
$e_{3,r}^s$		1,80E+03
$e_{1,r}^S$		1,1296900E+03
$e_{3,r}^S$		9,1373000E+02
$\tan d (3^s)$		0,017
$T_C >$	°C	350
k_p		0,592
k_t		0,469
k_{31}		0,327
k_{33}		0,699
k_{15}		0,609
d_{31}	C/N	-1,70E-10
d_{33}	C/N	4,25E-10
d_{15}	C/N	5,06E-10
d_h	C/N	8,50E-11
g_{31}	V m/N	-0,0107
g_{33}	V m/N	0,0267
g_{15}	V m/N	0,0373
e_{31}	C/m ²	-3,0874407739
e_{33}	C/m ²	16,0264000000
e_{15}	C/m ²	11,6439000000
h_{31}	V/m	-3,82E+08
h_{33}	V/m	1,9837E+09
h_{15}	V/m	1,16E+09
N_p	m/s	2011,08
N_t	m/s	1953
N_{31}	m/s	1400
N_{33}	m/s	1500
N_{15}	m/s	896
$Q_{m,p}^E$		89

$Q_{m,t}^E$		74
r	kg/m ³	7,70E+03
n_{12}^E		0,389
s_{11}^E	m ² /N	1,70E-11
s_{12}^E	m ² /N	-6,60E-12
s_{13}^E	m ² /N	-8,61E-12
s_{33}^E	m ² /N	2,32E-11
$s_{44}^E = s_{55}^E$	m ² /N	4,35E-11
s_{66}	m ² /N	4,71E-11
s_{11}^D	m ² /N	1,51E-11
s_{12}^D	m ² /N	-8,41E-12
s_{13}^D	m ² /N	-4,08E-12
s_{33}^D	m ² /N	1,19E-11
$s_{44}^D = s_{55}^D$	m ² /N	2,73E-11
c_{11}^E	N/m ²	1,47391095E+11
c_{12}^E	N/m ²	1,04936542E+11
c_{13}^E	N/m ²	9,36614417E+10
c_{33}^E	N/m ²	1,12634000E+11
$c_{44}^E = c_{55}^E$	N/m ²	2,30130000E+10
c_{66}	N/m ²	2,12272762E+10
c_{11}^D	N/m ²	1,48570050E+11
c_{12}^D	N/m ²	1,06115318E+11
c_{13}^D	N/m ²	8,75365618E+10
c_{33}^D	N/m ²	1,44425000E+11
$c_{44}^D = c_{55}^D$	N/m ²	3,65770000E+10
Y_{11}^E	GPa	5,90E+01
Y_{33}^E	GPa	4,31E+01
Y_{11}^D	GPa	6,60E+01
Y_{33}^D	GPa	8,43E+01
v_{33}^D	m/s	4330,88
Z_{33}^D	Mrayl	33,347751

B. Code for creating 2D sphere layer geometry (COMSOL)

```
package builder;
import com.comsol.model.application.*;
import com.comsol.api.*;
import com.comsol.model.*;
import com.comsol.model.physics.*;
public class Voids_NoOverlap extends ApplicationMethod {

public void execute() {
    ///-- CLEAR ALL
    model.result().table().remove("tbl1");
    model.result().table().clear();
    clearModel(model);
    message("-----MODEL CLEARED-----");
    model.component().create("comp1", true);
    model.component("comp1").geom().create("geom1", 2);
    model.component("comp1").mesh().create("mesh1");

    //GENERAL DEFINITIONS
    int ind = 0;
    double VFTarget = 10.0;
    double hx, hz, hr = 0.0;
    double dAg = 0.160;
    double BOND_HEIGHT = 21;
    double DEAD_ZONE = BOND_HEIGHT/1000;
    double BOND_WIDTH = 1000.00;
    double EDGE_THICKNESS = 0.001;
    double VOID_MIN_RADIUS = 10.00;
    double VOID_MAX_RADIUS = 10.00;
    model.component("comp1").geom("geom1").lengthUnit("um");

    // THIS LINE CREATES A CELL WHICH WILL CONTAIN ALL VOIDS AND WILL LATER BE
    SUBTRACTED FROM
    // THE RECTANGLE TO CREATE THE POROUS STRUCTURE
    model.component("comp1").geom("geom1").selection().create("csel1", "CumulativeSelection");

    //CALCULATING VOLUME FRACTION
    double SizeCount = 0;
    double TotalSize = BOND_HEIGHT*BOND_WIDTH;
    double VolumeFraction = ((SizeCount/TotalSize)*100);
```

```

//DEFINE ARRAYS AND MATRIX FOR POSITION TRACKING
double[] PosArray = new double[2];
double[][] AllPos = new double[1][2];
double Rad;
double[] AllRad = new double[1];

// LOOP UNTIL A TARGET VOLUME FRACTION IS REACHED.
// EACH ITERATION CREATES A NEW VOID WITH A RANDOM POSITION AND RADIUS
while (VolumeFraction < VFTarget) {
    hx = (Math.random()*BOND_WIDTH);
    hz = Math.random()*BOND_HEIGHT;
    hr = Math.random()*(VOID_MAX_RADIUS-VOID_MIN_RADIUS)+VOID_MIN_RADIUS;

    // MAKE SURE THE VOID ARE WITHIN THE DEFINED RECTANGLE
    if ((Math.sqrt(hx*hx)+hr) > BOND_WIDTH-EDGE_THICKNESS) {continue; }
    if ((Math.sqrt(hx*hx)-hr) < EDGE_THICKNESS) {continue; }
    // REMOVE VOIDS THAT APPEAR ON THE BORDER
    if (((hz-hr) < EDGE_THICKNESS) || ((hz+hr) > BOND_HEIGHT-EDGE_THICKNESS)) {continue; }
    // if (((hz > DEAD_ZONE) && (hz < DEAD_ZONE*2)) || ((hz > DEAD_ZONE*2) && (hz <
DEAD_ZONE*3)))) {continue; }
    //if ((hz-hr > DEAD_ZONE) || ((hz-hr > DEAD_ZONE*2))) {continue; }
    //if ((hz-hr > DEAD_ZONE*2)) {continue; }

    // if ((hz > DEAD_ZONE) && (hz < DEAD_ZONE*2)) {continue; }
    // if ((hz > DEAD_ZONE*2) && (hz < DEAD_ZONE*3)) {continue; }

    // THE POSITION AND RADIUS OF EACH VOID IS ADDED TO AN ARRAY
    PosArray = new double[]{hx, hz};
    AllPos = appendRow(AllPos, PosArray);
    Rad = hr;
    AllRad = append(AllRad, Rad);

    // ALL EXISTING VOIDS ARE CHECKED IF THE NEW VOID WILL OVERLAP
    for (int i = 0; i < AllRad.length; ++i) {
        double Xn = AllPos[i][0];
        double Zn = AllPos[i][1];
        double Rn = AllRad[i];
        double dist1 = ((hx-Xn)*(hx-Xn)+(hz-Zn)*(hz-Zn));
        double radSum1 = ((Rn)+hr)*((Rn)+hr);

```



```

// IF THERE IS AN OVERLAP OCCURRING SOMEWHERE, THE NEW VOID WILL BE
DISGARDDED AND REMOVED FROM THE POSITION-ARRAY
// THIS ITERATION OF THE LOOP BREAKS AND A THE WHILE-LOOP STARTS OVER
if (hr >= Rn && dist1 <= (hr-Rn)*(hr-Rn)) {
    message("Overlap Case 1");
    AllRad = remove(AllRad, ind+1);
    AllPos = removeRow(AllPos, ind+1);
    break;
}
else if ((Rn >= hr && dist1 <= (Rn-hr)*(Rn-hr))) {
    message("Overlap Case 2");
    AllRad = remove(AllRad, ind+1);
    AllPos = removeRow(AllPos, ind+1);
    break;
}
else if ((dist1 <= (radSum1))) {
    message("Overlap Case 3");
    AllRad = remove(AllRad, ind+1);
    AllPos = removeRow(AllPos, ind+1);
    break;
}

// IF THERE IS NO OVERLAP THE NEW VOID WILL BE ADDED TO THE CELL CONTAINING
ALL VOIDS

```

```

else {
    if (i == ind) {
        model.component("comp1").geom("geom1").create("c1"+ind, "Circle");
        model.component("comp1").geom("geom1").feature("c1"+ind).set("r", hr);
        model.component("comp1").geom("geom1").feature("c1"+ind).set("pos", new double[]{hx, hz});
        model.component("comp1").geom("geom1").feature("c1"+ind).set("contributeto", "cset1");
        model.component("comp1").geom("geom1").create("c1"+ind+100, "Circle");
        model.component("comp1").geom("geom1").feature("c1"+ind+100).set("r", hr-dAg);
        model.component("comp1").geom("geom1").feature("c1"+ind+100).set("pos", new double[]{hx, hz});
        model.component("comp1").geom("geom1").feature("c1"+ind+100).set("contributeto", "cset1");
        double VoidSize = Math.PI*Math.pow(AllRad[ind], 2);
        SizeCount += VoidSize;
        ind++;
        break;
    }
}

```

```

    else {
    }
}
}
VolumeFraction = ((SizeCount/TotalSize)*100);
}

//WHEN TARGET VOLUME FRACTION IS REACHED, THE RECTANGLE WILL BE BUILT AND
SUBTRACT VOIDS FROM FINAL GEOMETRY
model.component("comp1").geom("geom1").create("r1", "Rectangle");
model.component("comp1").geom("geom1").feature("r1").set("size", new double[]{BOND_WIDTH,
BOND_HEIGHT});
model.component("comp1").geom("geom1").feature("r1").set("base", "center");
model.component("comp1").geom("geom1").feature("r1").set("pos", new double[]{BOND_WIDTH/2,
BOND_HEIGHT/2});
//model.component("comp1").geom("geom1").create("dif1", "Difference");
//model.component("comp1").geom("geom1").feature("dif1").selection("input").set("r1");
//model.component("comp1").geom("geom1").feature("dif1").selection("input2").named("cse11");
//model.component("comp1").geom("geom1").run();
message("Exact Volume Fraction:");
message(VolumeFraction);
}
}

```

C. Code for creating 3D sphere layer geometry (COMSOL)

```
package builder;
import com.comsol.model.application.*;
import com.comsol.api.*;
import com.comsol.model.*;
import com.comsol.model.physics.*;
public class Voids_NoOverlap extends ApplicationMethod {

    public void execute() {
        ///-- CLEAR ALL
        model.result().table().remove("tbl1");
        model.result().table().clear();
        clearModel(model);
        message("-----MODEL CLEARED-----");
        model.component().create("comp1", true);
        model.component("comp1").geom().create("geom1", 3);
        model.component("comp1").mesh().create("mesh1");

        //GENERAL DEFINITIONS
        int ind = 0;
        double VFTarget = 10.00;
        double hx, hy, hz, hr = 0.0;
        double BOND_HEIGHT = 23.0;
        double BOND_WIDTH = 200.0;
        double EDGE_THICKNESS = 1.0;
        double VOID_MIN_RADIUS = 10;
        double VOID_MAX_RADIUS = 10;
        model.component("comp1").geom("geom1").lengthUnit("um");

        // THIS LINE CREATES A CELL WHICH WILL CONTAIN ALL VOIDS AND WILL LATER BE
SUBTRACTED FROM
        // THE RECTANGLE TO CREATE THE POROUS STRUCTURE
        model.component("comp1").geom("geom1").selection().create("csel1", "CumulativeSelection");
        model.component("comp1").geom("geom1").selection().create("csel2", "CumulativeSelection");

        //CALUCULATING VOLUME FRACTION
        double SizeCount = 0;
        double TotalSize = BOND_HEIGHT*BOND_WIDTH*BOND_WIDTH;
        double VolumeFraction = ((SizeCount/TotalSize)*100);
```

```

//DEFINE ARRAYS AND MATRIX FOR POSITION TRACKING
double[] PosArray = new double[3];
double[][] AllPos = new double[1][3];
double Rad;
double[] AllRad = new double[1];

// LOOP UNTIL A TARGET VOLUME FRACTION IS REACHED.
// EACH ITERATION CREATES A NEW VOID WITH A RANDOM POSITION AND RADIUS
while (VolumeFraction < VFTarget) {
    hx = Math.random()*BOND_WIDTH;
    hy = Math.random()*BOND_WIDTH;
    hz = Math.random()*BOND_HEIGHT;
    hr = Math.random()*(VOID_MAX_RADIUS-VOID_MIN_RADIUS)+VOID_MIN_RADIUS;
    //hr = VOID_MAX_RADIUS;

    // MAKE SURE THE VOID ARE WITHIN THE DEFINED RECTANGLE
    if ((Math.sqrt(hx*hx)+hr) > BOND_WIDTH-EDGE_THICKNESS) {continue; }
    if ((Math.sqrt(hx*hx)-hr) < EDGE_THICKNESS) {continue; }
    if ((Math.sqrt(hy*hy)+hr) > BOND_WIDTH-EDGE_THICKNESS) {continue; }
    if ((Math.sqrt(hy*hy)-hr) < EDGE_THICKNESS) {continue; }
    // REMOVE VOIDS THAT APPEAR ON THE BORDER
    if (((hz-hr) < EDGE_THICKNESS) || ((hz+hr) > BOND_HEIGHT-EDGE_THICKNESS)) {continue; }
    if (((hz-hr) < EDGE_THICKNESS) || ((hz+hr) > BOND_HEIGHT-EDGE_THICKNESS)) {continue; }

    // THE POSITION AND RADIUS OF EACH VOID IS ADDED TO AN ARRAY
    PosArray = new double[]{hx, hy, hz};
    AllPos = appendRow(AllPos, PosArray);
    Rad = hr;
    AllRad = append(AllRad, Rad);

    // ALL EXISTING VOIDS ARE CHECKED IF THE NEW VOID WILL OVERLAP
    for (int i = 0; i < AllRad.length; ++i) {
        double Xn = AllPos[i][0];
        double Yn = AllPos[i][1];
        double Zn = AllPos[i][2];
        double Rn = AllRad[i];
        double dist1 = ((hx-Xn)*(hx-Xn)+(hy-Yn)*(hy-Yn)+(hz-Zn)*(hz-Zn));
        double radSum1 = ((Rn)+hr)*((Rn)+hr);
    }
}

```

```

// IF THERE IS AN OVERLAP OCCURRING SOMEWHERE, THE NEW VOID WILL BE
DISGARDDED AND REMOVED FROM THE POSITION-ARRAY
// THIS ITERATION OF THE LOOP BREAKS AND A THE WHILE-LOOP STARTS OVER
if (hr >= Rn && dist1 <= (hr-Rn)*(hr-Rn)) { //
    message("Overlap Case 1");
    AllRad = remove(AllRad, ind+1);
    AllPos = removeRow(AllPos, ind+1);
    break;
}
else if ((Rn >= hr && dist1 <= (Rn-hr)*(Rn-hr))) {
    message("Overlap Case 2");
    AllRad = remove(AllRad, ind+1);
    AllPos = removeRow(AllPos, ind+1);
    break;
}
else if ((dist1 <= (radSum1))) {
    message("Overlap Case 3");
    AllRad = remove(AllRad, ind+1);
    AllPos = removeRow(AllPos, ind+1);
    break;
}

// IF THERE IS NO OVERLAP THE NEW VOID WILL BE ADDED TO THE CELL CONTAINING
ALL VOIDS

```

```

else {
    if (i == ind) {
        model.component("comp1").geom("geom1").create("sph1"+ind, "Sphere");
        model.component("comp1").geom("geom1").feature("sph1"+ind).set("r", hr);
        model.component("comp1").geom("geom1").feature("sph1"+ind).set("pos", new double[]{hx, hy, hz});
        model.component("comp1").geom("geom1").feature("sph1"+ind).set("contributeto", "csel1");

        //    //--Make line segment
        //    model.component("comp1").geom("geom1").create("ls1"+ind, "LineSegment");
        //    with(model.component("comp1").geom("geom1").feature("ls1"+ind));
        //    set("specify1", "coord");
        //    set("specify2", "coord");
        //    set("coord1", new double[]{hx-hr, -10});
        //    set("coord2", new double[]{hx+hr, -10});
        //    endwith();
        //    model.component("comp1").geom("geom1").feature("ls1"+ind).set("contributeto", "csel2");
    }
}

```

```

//
double VoidSize = (4/3)*Math.PI*Math.pow(AllRad[ind], 3);
SizeCount += VoidSize;
ind++;
break;
}
else {
}
}
}
VolumeFraction = ((SizeCount/TotalSize)*100);
}

//WHEN TARGET VOLUME FRACTION IS REACHED, THE RECTANGLE WILL BE BUILT AND
SUBTRACT VOIDS FROM FINAL GEOMETRY

model.component("comp1").geom("geom1").create("blk1", "Block");
model.component("comp1").geom("geom1").feature("blk1").set("size", new double[]{BOND_WIDTH,
BOND_WIDTH, BOND_HEIGHT});
model.component("comp1").geom("geom1").feature("blk1").set("base", "center");
model.component("comp1").geom("geom1").feature("blk1").set("pos", new double[]{BOND_WIDTH/2,
BOND_WIDTH/2, BOND_HEIGHT/2});

//model.component("comp1").geom("geom1").create("dif1", "Difference");
//model.component("comp1").geom("geom1").feature("dif1").selection("input").set("blk1");
//model.component("comp1").geom("geom1").feature("dif1").selection("input2").named("csel1");

model.component("comp1").geom("geom1").create("uni1", "Union");
model.component("comp1").geom("geom1").feature("uni1").selection("input").named("csel2");
model.component("comp1").geom("geom1").run();

//-----Calculate Fractions-----
model.study().create("std1");
model.study("std1").create("stat", "Stationary");
model.component("comp1").cpl().create("intop1", "Integration");
with(model.component("comp1").cpl("intop1"));
  set("axisym", true);
endwith();
model.component("comp1").cpl("intop1").selection().geom("geom1", 1);
model.component("comp1").cpl("intop1").selection().named("geom1_csel2_bnd");
model.component("comp1").cpl().create("intop2", "Integration");
with(model.component("comp1").cpl("intop2"));
  set("axisym", true);

```

```

endwith();
model.component("comp1").cpl("intop2").selection().geom("geom1", 1);
model.component("comp1").cpl("intop2").selection().set(3);
model.component("comp1").variable().create("var1");
with(model.component("comp1").variable("var1"));
  set("VoidLength", "intop1(1)");
  set("FullLength", "intop2(1)");
  set("Thickness", "intop4(1)");
  set("AreaFraction", "(VoidLength/FullLength)*100");
  set("FullVolume", "Thickness*FullLength");
  set("VoidVolume", "intop3(1)");
  set("VolumeFraction", "(1-(VoidVolume/FullVolume))*100");
endwith();
model.component("comp1").cpl().create("intop3", "Integration");
with(model.component("comp1").cpl("intop3"));
  set("axisym", true);
endwith();
model.component("comp1").cpl("intop3").selection().set(1);
with(model.component("comp1").variable("var1"));
  set("VoidVolume", "intop3(1)");
endwith();

model.component("comp1").cpl().create("intop4", "Integration");
with(model.component("comp1").cpl("intop4"));
  set("axisym", true);
endwith();
model.component("comp1").cpl("intop4").selection().geom("geom1", 1);
model.component("comp1").cpl("intop4").selection().set(1);
with(model.component("comp1").variable("var1"));
  set("Thickness", "intop4(1)");
endwith();

model.sol().create("sol1");
model.sol("sol1").study("std1");
with(model.study("std1").feature("stat"));
  set("notlistsolnum", 1);
  set("notsolnum", "1");
  set("listsolnum", 1);
  set("solnum", "1");

```

```

endwith();
model.sol("sol1").create("st1", "StudyStep");
with(model.sol("sol1").feature("st1"));
    set("study", "std1");
    set("studystep", "stat");
endwith();
model.sol("sol1").create("v1", "Variables");
with(model.sol("sol1").feature("v1"));
    set("control", "stat");
endwith();
model.sol("sol1").create("s1", "Stationary");
model.sol("sol1").attach("std1");
model.sol("sol1").runAll();
model.result().numerical().create("gev1", "EvalGlobal");
with(model.result().numerical("gev1"));
    set("expr", new String[]{"FullLength"});
    set("descr", new String[]{""});
    set("unit", new String[]{"\u00b5m"});
endwith();
model.result().numerical().create("gev2", "EvalGlobal");
with(model.result().numerical("gev2"));
    set("expr", new String[]{"VoidLength"});
    set("descr", new String[]{""});
    set("unit", new String[]{"\u00b5m"});
endwith();
model.result().numerical().create("gev3", "EvalGlobal");
with(model.result().numerical("gev3"));
    set("expr", new String[]{"AreaFraction"});
    set("descr", new String[]{""});
    set("unit", new String[]{"\u00b5"});
endwith();
model.result().numerical().create("gev4", "EvalGlobal");
with(model.result().numerical("gev4"));
    set("expr", new String[]{"VolumeFraction"});
    set("descr", new String[]{""});
    set("unit", new String[]{"\u00b5m^2"});
endwith();

```



```

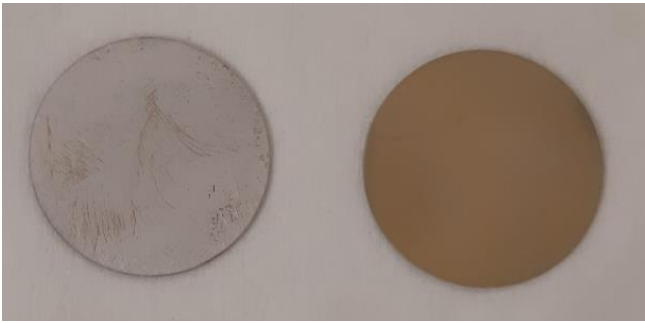

model.result().table().create("tbl1", "Table");
model.result().table("tbl1").comments("Global Evaluation 1");
with(model.result().numerical("gev1"));
  set("table", "tbl1");
endwith();
model.result().numerical("gev1").setResult();
with(model.result().numerical("gev2"));
  set("table", "tbl1");
endwith();
model.result().numerical("gev2").appendResult();
with(model.result().numerical("gev3"));
  set("table", "tbl1");
endwith();
model.result().numerical("gev3").appendResult();
with(model.result().numerical("gev4"));
  set("table", "tbl1");
endwith();
model.result().numerical("gev4").appendResult();

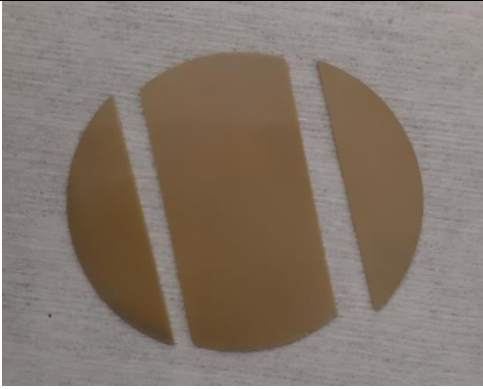
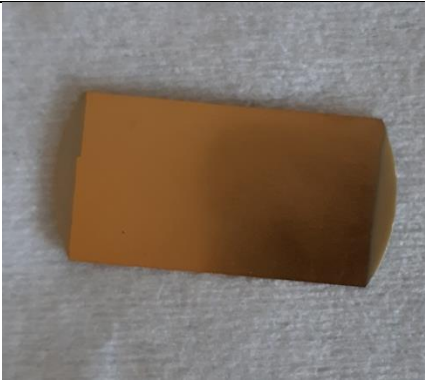

message("Exact Volume Fraction:");
message(VolumeFraction);
}
}


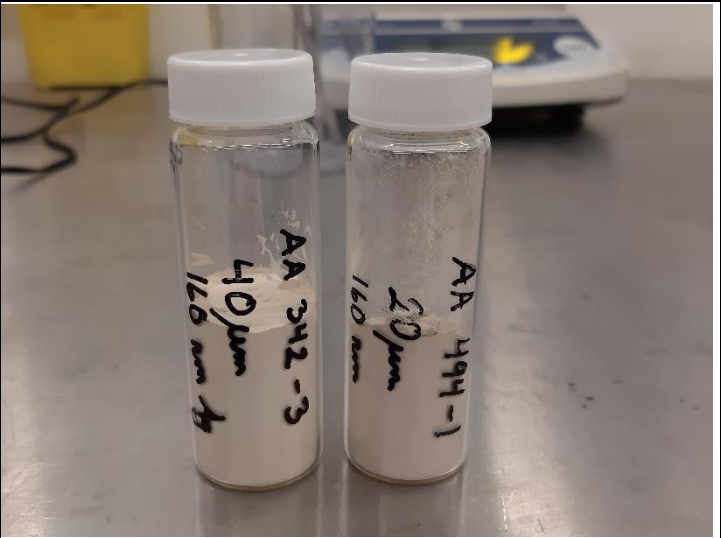
```

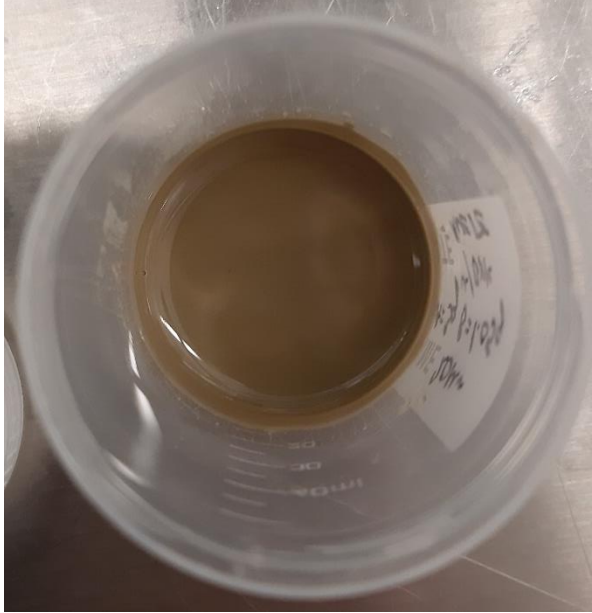
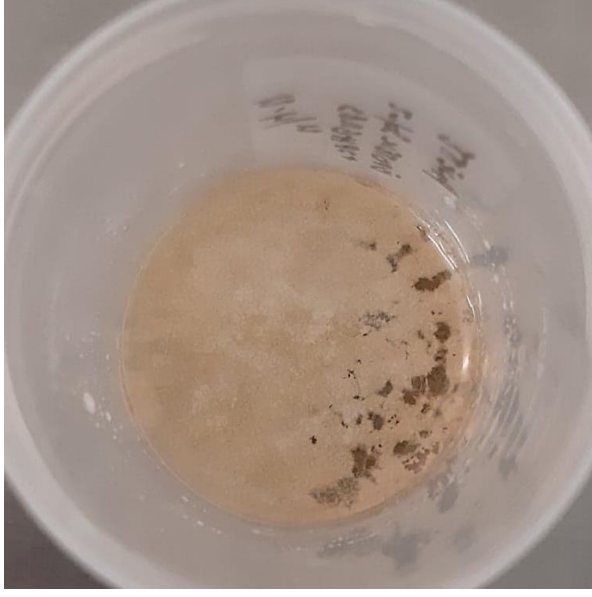
D. Transducer process


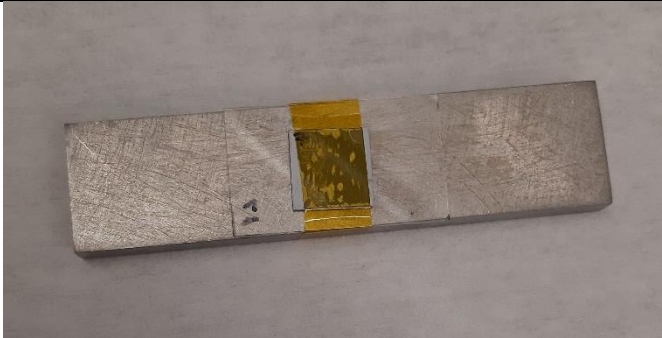
In some of the cases, like with the trial sample batch, step 1 was not necessary, as the PZT used already had a wrap around.



	Step	Procedure	Other information
Wrap around	1.1	The thickness of large plates of Pz27, was measured, before it was grinded by hand to remove the electrode already present on both sides. The main part of the electrode was removed using paper with grit 600. When the electrode was gone, paper with grit 1200 was used to smoothen the surface.	Material: Pz27 Size: 3 cm diameter
			Pz27 samples before and after electrode removal
	1.2	The samples were then glued to a dicing tape and a long plate of width 1.5 cm was diced out of the larger circular plates with the dicing saw (<i>Disco DAD 3220</i>)	
			Disco DAD 3220 dicing saw

			The diced Pz27 plate
	1.3	The diced Pz27 was cleaned in an ultrasonic bath for 5 minutes, then plasma cleaned (<i>Alpha Plasma</i>) with O ₂ for 30 seconds on each side. The clean PZTs were taped to a plate and sputtered one side at a time, first with a 20 nm chromium layer, then with 200 nm gold.	
			Gold sputtered Pz27 piece
	1.4	The sputtered plates were diced in the middle parallel to the long side of the plate. Samples were made by dicing the long sides into smaller elements of 5 mm. A second cut was also made along the long side, 2.5 mm in, this only going halfway through the sputtered Pz27 to cut the contact between the upper and bottom electrode.	
			Pz27 on the dicing tape after all cuts to create the wrap around
Mixing	2.1	The mixing of the glue and sphere was done in a fume hood. Firstly pipettes were used to add the two parts of the Epo-tek 301-2, Epo-tek 301-2 part A and Epo-tek 301-2 part B, in the relation 100:35 (A:B) in a cup, and this was mixed in the Speed	Materials: - Epo-tek 301-2 part A and part B


	<p>Mixer for 2 minutes at 2500 rpm. The weight of glue desired for the finished mix was taken out of the pre-mix into a separate container, where the calculated weight of spheres also was added. This mix of glue and spheres were then spun 2 minutes at 2500 rpm.</p>	<p>- MPS (20 μm and 40 μm diameter)</p>
		<p>Mixing station with the weight, Epo-tek part A in the blank cup and part B in the brown bottle</p>
		<p>Bottles containing the spheres</p>
<p>2.2</p>	<p>After spinning, the glue and sphere mix was vacuumed for 15 minutes. In some cases 1 minute in the speed mixer was necessary after the vacuuming due to separation of glue and spheres in the vacuuming process.</p>	



			<p>20 μm glue-sphere mix after vacuuming.</p>
			<p>40 μm glue-sphere mix after vacuuming.</p>

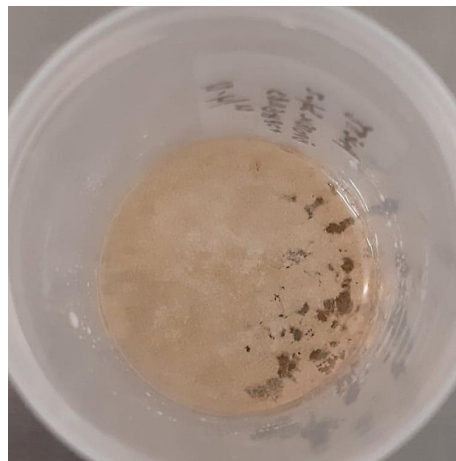
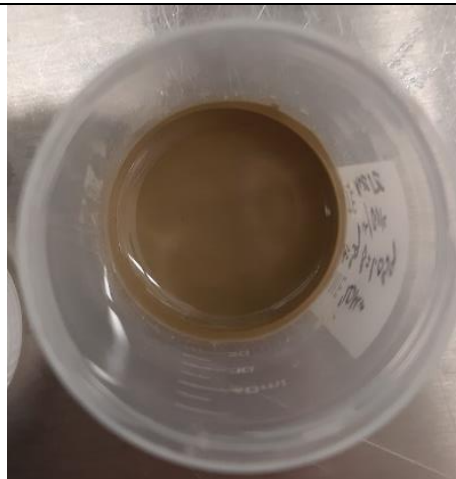
			The vacuum pump and chamber
Monolayer	3.1	The glass and WC was cleaned with water for 5 minutes before they were used. The monolayer samples were made both with PZT and Si. A plastic stick was dipped into the the mix, and then used to place a drop of the mix on the load.	Materials: - Mix - Glass - WC
	3.2	The PZT/Si that was being glued to the load was placed so that the mix would be approximately in the center of the element and then placed on top of the drop. A tape was gently placed over the element to avoid it from sliding. In some cases this tape had already been glued to the element, and the element was gently taped to a metal underlayer before the weight was placed on top.	Materials: - PZT - Si - Weight (675 g, 835 g, and 1.12 kg)
			Si on glass taped down.
Curing	4	The samples were put in the oven at 80°C for curing in 3 to 4 hours. In a few cases the samples had to be taken out after 2 hours, but these were left to cure in air for a few days before anything else was done.	

			<p>Samples during the curing process in the oven</p>
<p>Measurements</p>	<p>5</p>	<p>The PZT samples were investigated using the <i>R&S® ZVL Vector Network Analyzers</i> setup.</p>	 <p><i>R&S® ZVL Vector Network Analyzers</i> setup</p>



E. Speed of Sound samples

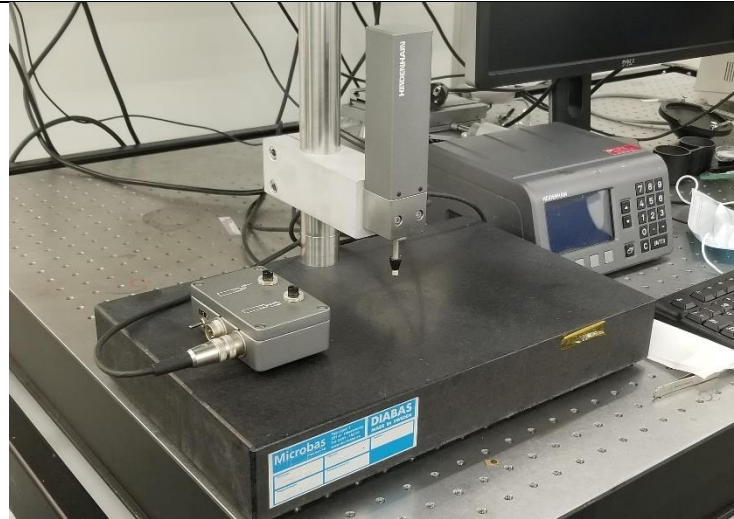
	Step	Procedure	Other information
Mixing	1	The Epo-tek 301-2 was mixed in the ratio 100:35 for part A:part B, which was then mixed in the speed mixer for 2 minutes. Then a given weight of the mix was put in another container, and a calculated weight of spheres was added. For two of the mixing trial samples a drop of Byk was also added	- Epo-tek 301-2 - MPS
			Setup for the mixing of speed of sound samples.
	2	The mix of epoxy and MPS was first stirred with a plastic stick, and then put in the Speed Mixer (<i>DAC 150FVZ-K</i>) at 2500 rpm for 2 minutes.	

			<p>The SpeedMixer DAC 150 FVZ-K</p>
			<p>Sample after mixing</p>
<p>3</p>		<p>After mixing, the sample was locked in a vacuum chamber for 15 minutes to remove the air bubbles.</p>	<p>Vacuum pump with vacuum chamber</p>



20 µm sample (top) and 40 µm sample (bottom) after vacuuming

	4	<p>The samples were put in the oven at 80°C between 3 and 4 hours to cure. They were taken out and spun after 30 minutes, and checked every 5 minutes up to 1 hour to see if it had separated. Most showed signs of beginning sedimentation at the 40 minutes check, and were then taken out and spun for another 1 minute. Some also showed signs of sedimentation up to 55 minutes.</p>	
			<p>Samples with sedimentation (left) and even distribution (right)</p>
Grinding and measurement	6	<p>The cured samples were grinded using a grinding machine (<i>MultiPrep system for grinding and polishing</i>), first with paper with grit 240 to flatten the surface, then with paper with grit 600 to smooth out. The thickness of the samples was measured before the speed of sound was measured in the setup of Figure 3.4.</p>	
			<p>MultiPrep system for grinding and polishing</p>



The
Heidenhain
thickness
gauge